Electromagnetic Modeling for Radar Remote Sensing of Snow-Covered Terrain

By

Mostafa M. Zaky

A dissertation submitted in partial fulfillment
of the requirements for the degree of
Doctor of Philosophy
(Electrical Engineering)
in the University of Michigan
2021

Doctoral Committee:

Professor Kamal Sarabandi, Chair
Dr. Roger Dean De Roo
Associate Professor Branko Kerkez
Professor Leung Tsang
Professor Fawwaz T. Ulaby

Mostafa M. Zaky

mzaky@umich.edu

ORCID iD: 0000-0001-6014-0724

DEDICATION

To my father, my role model and my main source of motivation; may his soul rest in peace!

ACKNOWLEDGEMENTS

TABLE OF CONTENTS

LIST OF TABLES

LIST OF FIGURES

x

ABSTRACT

This thesis investigates the radar remote sensing of snow-covered terrain for estimation of snow equivalent water on global scale. The importance and impact of this research stems from the fact that water from snowmelt is the major source of water for inland cities and agriculture during summer. This effort is focused on developing a physics-based model for snow and a fully coherent polarimetric scattering model for snow above ground. Both the physical model and the forward polarimetric scattering model present a significant improvement compared to the existing models for snowpack.

Computer-generated snow media are constructed using 3-D spatial exponential correlation functions, along with Lineal-Path functions that serve to preserve the connectivity of the snow particles. A fully-coherent model is presented through the use of the **S**tatistical **S**-matrix **Wa**ve **P**ropagation in **S**pectral-**D**omain (SSWaP-SD) technique. The SSWaP-SD depends on the discretization of the medium into thin slabs. Several realizations of a thin snow slab are solved numerically to form the statistics of the scattering matrix representing such a thin snow layer. For each thin slab of the snow-pack, a corresponding polarimetric N-port (representing different directions of scattering) S-matrix is generated. These S-matrices are cascaded using the SSWaP-SD method to calculate the total forward and backward bistatic scattered fields in a fully coherent way. The SSWaP-SD, in conjunction with a Method of Moments (MoM) code based on the Discrete-Dipole Approximation (DDA), is chosen to leverage both the time-efficient computations of the DDA and the full-coherency of the SSWaP-SD method, simultaneously. In addition to the

MoM-DDA, a Finite Element Method (FEM) based on commercial software is used for cross-comparison and validation. The simulation results of the backscattering from an arbitrary thick snow layer are presented and validated with measurements.

The underlying rough ground surface response is then estimated through both an analytical technique based on the Physical Optics (PO) method and a numerical solver based on MoM using a commercial full-wave solver. Finally, the complete response is then calculated by cascading the S-matrices representing the snow and the rough surface responses. The simulation results of the backscattering are presented using a Monte-Carlo process, which show very good agreement with measurements.

Chapter 1

Introduction

1.1. Background and Motivation

Water is the single most precious resource that exists on our planet. It is everyone's absolute responsibility to manage and keep such a vital element of life. A substantial amount of water is stored in the form of snow, especially during the winter season. Accurate estimation of snow accumulation plays a significant role in hydrology and the study of climate change, with direct relevance to important applications such as flood forecasting [1], agriculture [2] and the management of water resources [3]. There is a substantial amount of water stored in the form of snow, especially during the winter season. The runoff from melting of snow is the main source of water during summer in many parts of the world with huge impact on billions of people living inland. Study of the water cycle and understanding its change due to the effects of global warming has been the subject of intense investigation for the past several decades. Snow accumulated over mountainous terrain is measured by a parameter known as the Snow-Water Equivalent (SWE). The Snow-Water Equivalent is the hypothetical equivalent amount of water that results from an instantaneous complete melting of the snow pack [4]. The SWE is mathematically related to the snow depth and snow density as in (1.1)

$$SWE = \frac{Snow\ Depth}{Snow\ Density} \qquad (1.1)$$

While the snow density depends on the "type" and "age" of the snow [5] and the snow depth can vary greatly from hour to hour, due to settlement and compaction of the snow, the amount of water contained within the snow remains consistent. That is why scientists are more interested in the measurement of SWE than in the measurement of the snow depth. Because the supply of water during the spring and summer season is dependent on the amount of water stored in the snowpack during the winter months, snow water equivalent is used as the standard measure for characterizing snowpack water content.

A snowpack is essentially formed by the accumulation of ice particles on the ground surface. The process of snow formation during a winter storm relies heavily on temperature, but not necessarily the temperature at the ground surface. There are basically two conditions for snow
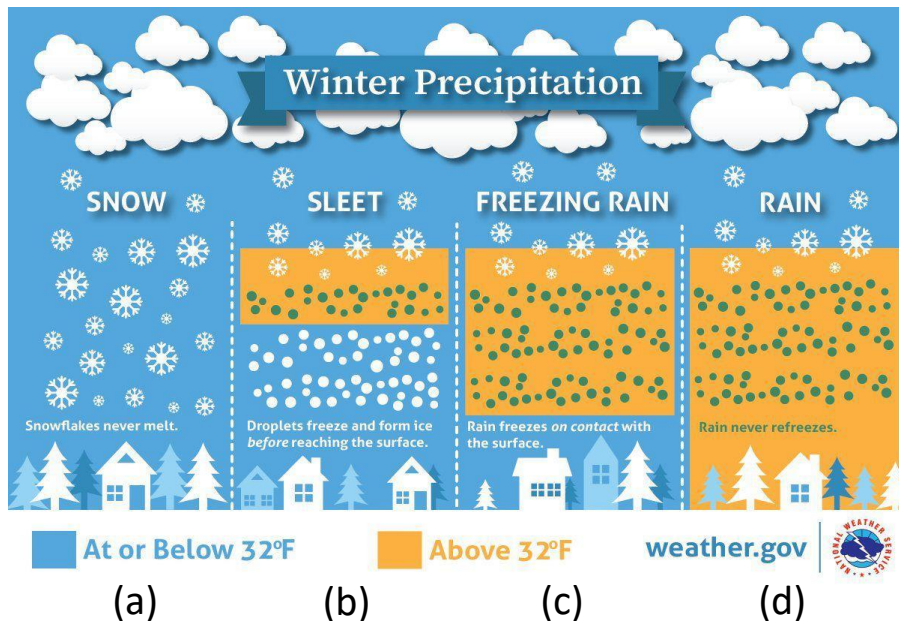
Figure 1.1 Winter Perception scenarios [4] for different atmospheric conditions: (a) the whole atmospheric layer is below freezing, (b) if a high-latitude layer is warmer than freezing, (c) if the atmospheric temperature is below freezing but the ground surface is at or above freezing, and (d) if everything is below freezing.

to form: (1) the atmospheric temperature should be at or below freezing (0 degrees Celsius or 32 degrees Fahrenheit), and (2) there should be a minimum amount of moisture in the air. If both conditions are satisfied, the winter storm produces snowflakes [6] that can reach the ground in the form of various types of precipitation depending on the temperature profile of the atmosphere. The various precipitation scenarios are summarized in Fig. 1.1 [7]. If the atmospheric temperature and the ground temperature are both below freezing, as in Fig. 1.1(a), the snow never melts and falls in the form of snowflakes that accumulate on the ground to form a snowpack. When present in a warmer-than-freezing high-altitude atmospheric layer, as in Fig. 1.1 (b), the snow melts into liquid form inside this high-temperature layer. Interestingly, this melting process creates partial evaporative cooling that brings the air temperature around the snowflakes into lower temperatures, thereby opposing the melting process. However, if the high-temperature layer is thick enough, the snowflakes would melt completely. But if there exists another below-freezing atmospheric layer between the warm layer and the ground, then the liquid droplets partially transform into solid to form sleet. Conversely, if the atmospheric temperature profile is mostly above freezing but the ground itself is below freezing, then frozen rain is produced as depicted in Fig. 1.1(c). Similarly, if both the ground and the atmospheric temperatures are above freezing, then this results in regular rain precipitation as in Fig. 1.1(d). As a general rule, however, snow will not form if the ground temperature is at 5 degrees Celsius (41 degrees Fahrenheit) or higher, according to the National Snow & Ice Data Center.

The characteristics of the snowpack after a snowfall depend on the original form of the crystals and on the weather conditions present when the snow fell. For example, when a snowfall is accompanied by strong winds, the snow crystals are broken into smaller fragments that can become more densely packed. After a snowfall, snow may melt or evaporate, or it may persist for
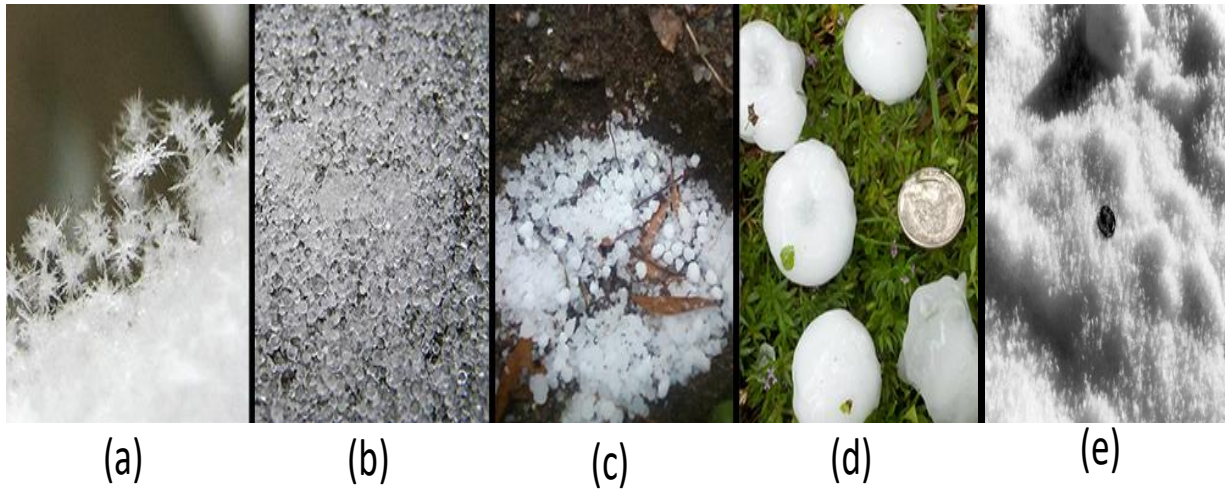
Figure 1.2 Forms of different frozen precipitation [7]: (a) snowflakes, (b) sleet, (c) graupel, (d) hail and (e) hoarfrost.

long periods. If snow persists on the ground, the texture, size, and shape of individual grains will change even while the snow temperature remains below freezing, or they may melt and refreeze over time, and will eventually become compressed by subsequent snowfalls. Different snow types are depicted in Fig. 1.2 [7].

Over the winter season, the snowpack typically accumulates and develops a complex layered structure made up of a variety of snow grains, reflecting the weather and climate conditions prevailing at the time of deposition as well as changes within the snow cover over time. An example of such snow accumulation is depicted in Fig. 1.3 for Iceland [8], where the left part of the photo is taken in the early summer and the right part was taken in the middle of the winter.
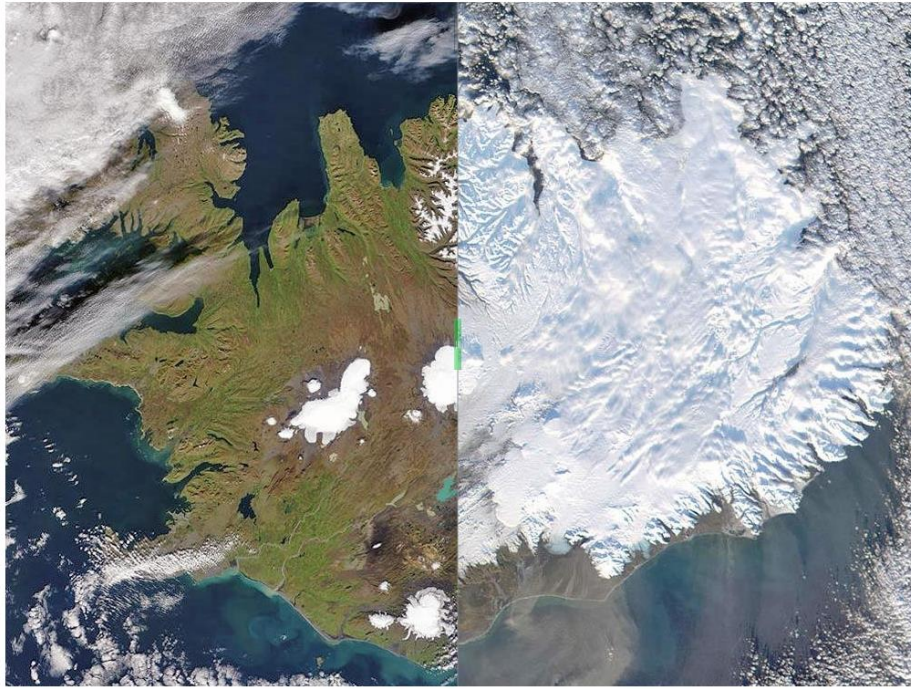
Figure 1.3 A satellite image of Iceland [8] in a) late summer, showing ice-free landscape except for permanent ice fields, and b) the middle of winter, showing that the island country is almost completely covered in white snow and ice.

An example of depicting the spatial distribution of snow-covered areas in the U.S. during winter of 2019-2020 is shown in Fig. 1.4. The snow accumulation map data is updated by NOAA on a daily basis. Figure 1.4(a) provides a map for a day in early winter (November), and Fig. 1.4 (b) shows the map for a day in the middle of the winter season. As we can surmise from the maps, the vast majority of the U.S. (and especially, the northern part) is actually covered with snow. To highlight the importance of the problem, we recite the information in [9] which states that 80% of the land in Eurasia and North America is covered with snow in the winter season which is equivalent to about 46.5 million km^2 of the Northern hemisphere during the month of January. Even in August, about 3.8 million km^2 remain covered in snow. Of course, the water contained
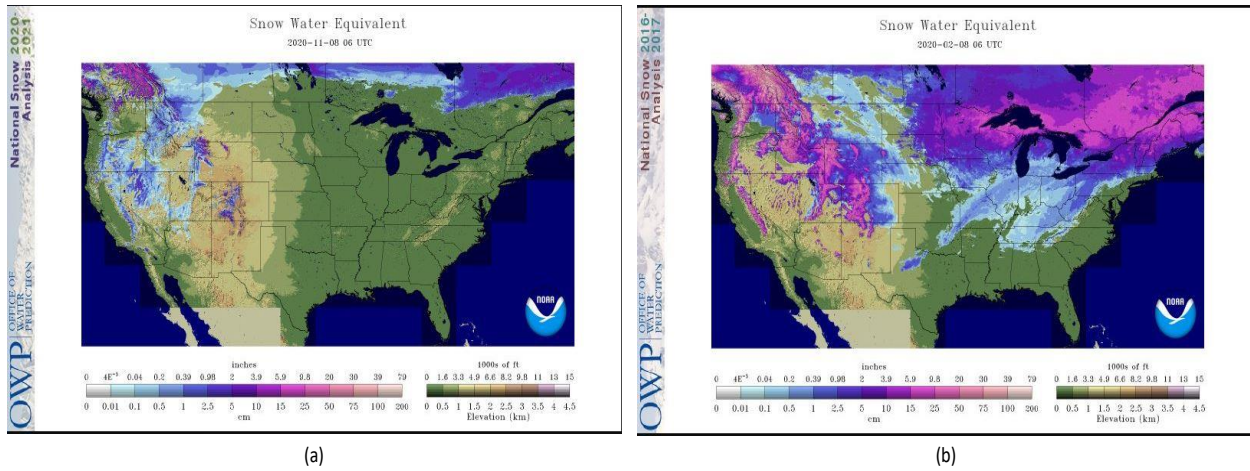
Figure 1.4 A snow water equivalent map for the United States [7] in (a) November, 2020, and (b) February, 2019.

in the snowpack results in an equivalent amount of liquid water when melted during the spring/summer season. According to [10], the snow run-off contribution to the total streamflow is around 50-80% during late spring. Additionally, glaciers and permanent snow cover produces 68.7% of the total fresh water of the global reserves [11], of which the Antarctic contributes 61.7%, Greenland contributes 6.68%, the Arctic Islands contributes 0.24%, and mountainous regions contribute 0.12%. To highlight how large the percentage of fresh water reserve produced by snow is, we can refer to the total amount of fresh water reserve produced by soil moisture, which is only 0.05% of the total fresh water [12], compared to 68.7% for snow-covered areas.

These numbers highlight how important it is to monitor and estimate the SWE accurately. Several sensing techniques have been proposed to estimate the distribution of SWE, both regionally and globally. In-situ measurement of SWE are usually performed by burying a sensor underneath the snow cover [13-17]. A common in-situ measurement technique is the snow-course which entails taking multiple samples of the snowpack at multiple locations. Over 2000 sites in

the western U.S. use the snow-course measurement approach to monitor SWE [13]. Multiple samples of snow are taken using a snow tube inserted in the snowpack and weighed using a calibrated scale to give the SWE value for the snowpack at the location [14]. However, manual sampling of the snow is tedious, expensive, and time-consuming. Alternatively, automatic SWE monitoring is achievable through the use of snow pillows (also known as SNOTEL). Over 800 snow pillows are installed in the western part of the U.S. to continuously measure the SWE. A photograph of a typical sampling site is shown in Fig. 1.5 [15], which consists of snow pillow, snow depth sensor, equipment shelter, and telemetry radio equipment. A snow pillow is meant to measure the weight of the water inside a snowpack as a function of time [16]. The pillow is connected to a stilling well, as shown in Fig. 1.6, via a pipe. When the ground is bare, the liquid level inside the stilling well is measured and recorded. During winter precipitation, snow accumulation changes the pressure on the pillow which is then transferred to the stilling well via an underground hose. This pressure causes the level of the liquid in the stilling well to change accordingly and that change is directly related to the value of SWE, given the snow depth information from the snow depth sensor. Additionally, a snow probe can be used to measure the density and wetness level of the snow as well [17]. The snow probe consists of a coaxial cable-based cavity resonator whose resonant frequency depends on the amount of snow present in the cavity. Moreover, acoustic-based sensors can be used as well to monitor the SWE [18], wherein a microphone is placed at a vertical distance away from the snowpack and the reflected mechanical vibration is then sensed by a loud speaker.
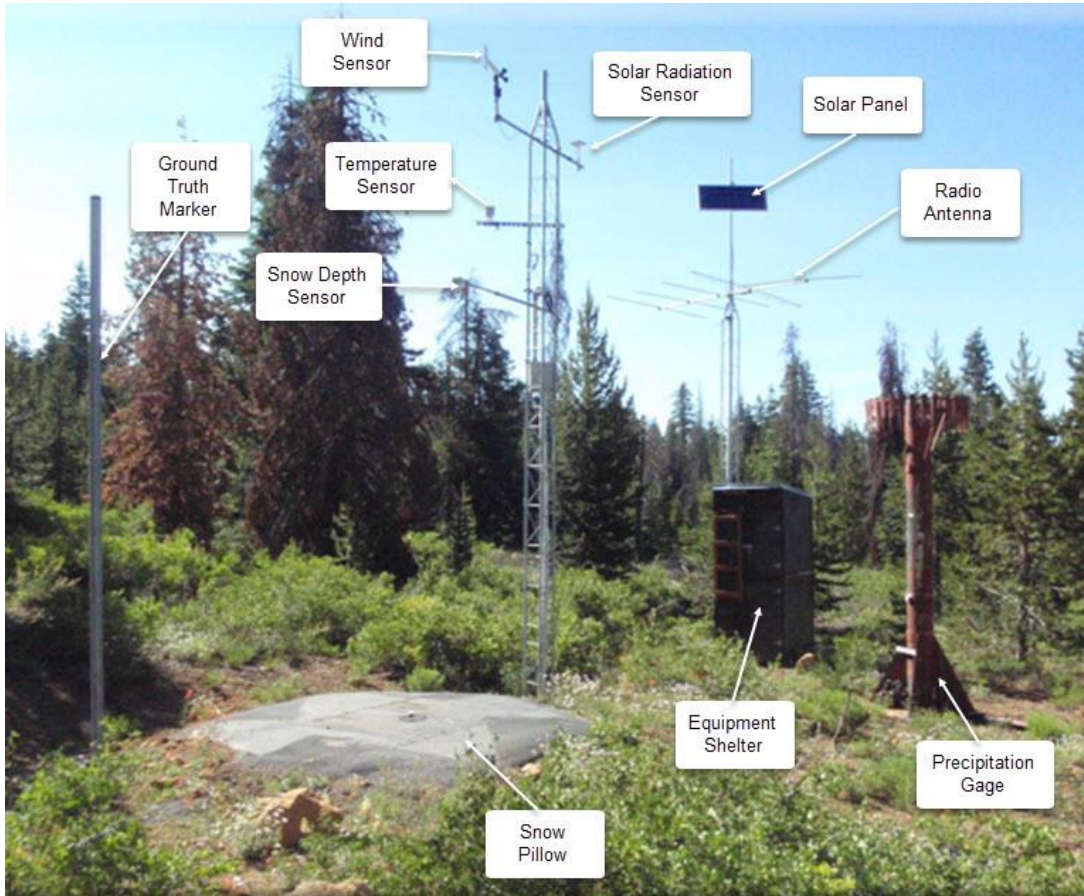
Figure 1.5 Typical SNOTEL site [16].
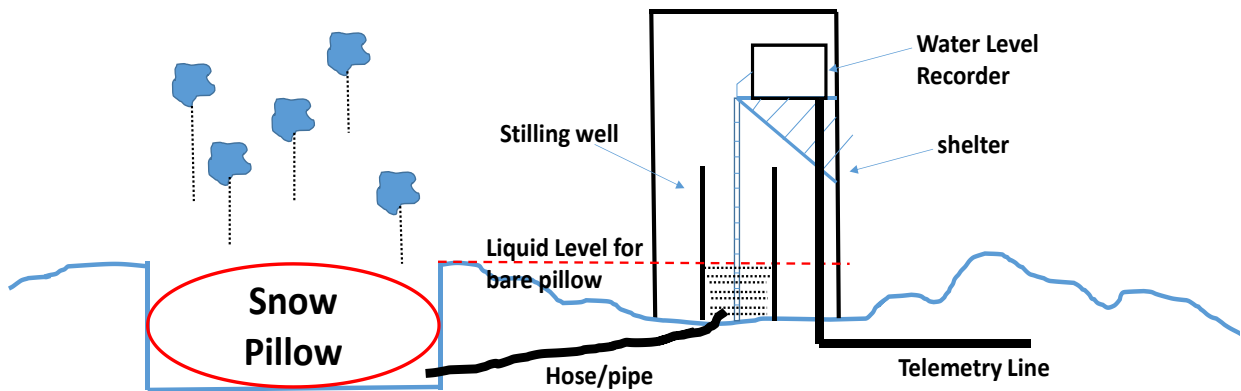
Figure 1.6 Snow pillow (SNOTEL) operation description.

However, the disadvantage of in-situ techniques is that they can cover only specific locations. SWE can also be determined using LiDARs (Light Detection And Ranging) either via airborne sensors or using ground based instruments [19]. LiDAR is considered an accurate sensing technique to measure snow depth information for forested terrains by illuminating the scene of interest with a laser pulse and then recording the reflected pulses via a discrete-return receiver. When directed downwards towards the scene, the system detects discrete return times corresponding to the distances to, and therefore the heights of, individual obstacles. While this technique accurately captures returns from trees and largely-spaced elements, the ice-particles are closely-packed in the snow, requiring appropriate adjustment to the receiver system. A photon-counting receiver system is used instead to measure the profile of the return photons [20], which is directly related to the number of scatterers inside the medium. Therefore, LiDAR can estimate the snow depth from the discrete return time and can estimate the density of the snow from the photon count profile, thereby providing an estimate of SWE from these two parameters using Eq. (1.1). However, the LiDAR technique suffer from high noise levels contributed by solar photons, particularly during daytime.

In contrast to in-situ snow sensors, satellite-borne remote sensing sensors offer the ability to measure SWE at a global scale [21-22]. Both passive and active remote sensing techniques have been utilized to provide estimation of snow depth and SWE over large areas. The reader is referred to [23] for a detailed discussion of the basics of passive and active remote sensing techniques. A summary of these techniques is presented in section 1.2.2. It is worth noting that InSAR techniques are particularly useful in this regard because they can be used to map SWE with high resolution [24].

Determining SWE from radar remote sensing measurements remains a very challenging problem. The goal is to estimate SWE from the radar backscattering coefficient measured by an imaging radar system. Such a retrieval requires the application of a very precise solution of the inverse-scattering problem, which can be developed using a well-trained machine learning algorithm that uses a set of calibrated values of the backscattering coefficient defined at a set of different frequencies or incident angles [25-27]. Achievement of such high-accuracy inversion technique is impossible without the availability of a very accurate training set of radar data and corresponding SWE values, which is only made through a physics-based forward scattering model. The development of such accurate physics-based forward model is the main objective of this work.

1.2. Recent Advances in Microwave Remote Sensing of Snow

Electromagnetic (EM) scattering from a random medium over a rough ground surface has been a major topic of interest in microwave remote sensing for many years. The combined volume scattering and surface scattering problem requires a solution that accounts for both attenuation and multiple scattering caused by the scatterers within the random medium and reflections by the underlying rough surface. Many remote sensing problems of interest consist of such composite scenarios [28-29], such as remote sensing of soil moisture in forested terrain and croplands as well as snow cover over ground surfaces. From a radar remote sensing perspective, the measured backscattering coefficient represents the full response of the system due to everything within the imaged pixel. The measured backscattering coefficient can be decomposed into the individual scattering contributions from the volume and surface. However, such discrimination between the surface and volume scattering components, without considering the interaction between them is a major oversimplification. Accurate forward scattering models are needed to accomplish the task

of inverse scattering for retrieval of the physical parameters of both the rough surface and the random volume.

A complete solution of the forward scattering problem is constructed from the output of four intermediary-steps: (1) computer-generation of a physics-based model for the snow samples and the underlying rough surface, (2) development of an accurate time-efficient numerical computation method for calculating electromagnetic scattering from the computer-generated samples of the snow, (3) solution for scattering from the rough surface, and (4) development of a coherent superposition technique to account for the snow and rough surface interactions.

The composite scattering scenario from the snowpack over the rough surface is depicted in Fig. 1.7. There are multiple components that need to be considered in order to completely account for the full response of the backscattering coefficient including: (1) the air-snow interface, (2) the volumetric snow contribution, and (3) the snow-ground reflection. A general form of the total backscattering could be written as

$$\sigma^o_{total} = \sigma^o_{air-snow} + \sigma^o_{snow\ volume} + \sigma^o_{snow-ground} \tag{1.2}$$
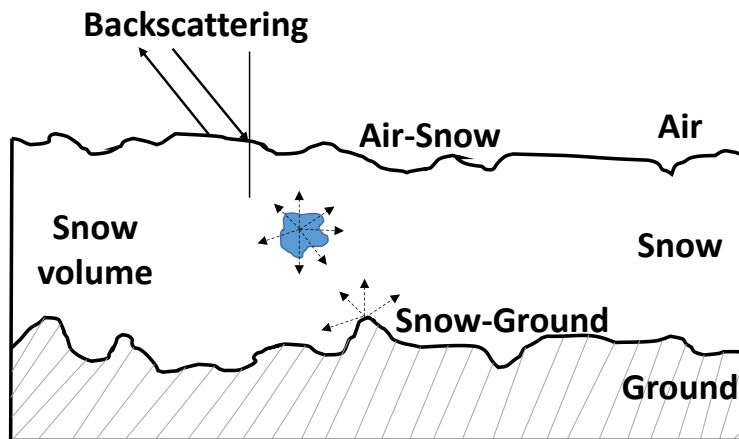
Figure 1.7 Electromagnetic scattering from Snowpack over rough ground.

where σ^o is the normalized backscattering coefficient. This equation may imply that the full scattering response from the snowpack can be obtained by direct superposition of the individual backscattering components, thereby simplifying the problem to solve for each component by itself and then adding the three contributions to obtain the total response. However, such an incoherent-addition (adding powers instead of fields) does not account for the phase information. Instead, to accurately account for volume scattering by the densely-packed snow particles and their interaction with the underlying ground surface, a fully coherent model that accounts for phase is required.

1.3. Modeling Snow's Ice Particles

Snow as a mixture of ice and air [30]. Among the many different approaches proposed for reconstructing 3-D volume of snow, two methods stand out as particularly worth considering. These are the densely-packed sticky particles method [31-32], and the Bi-continuous media method [33-34]. For the densely-packed particles method, the particles are assumed to be spherical in shape with a specific size and stickiness coefficient. Using these two parameters, an iterative algorithm is used to randomly locate the spheres such that their spatial distribution satisfies the specified volume fraction Φ_v. An example of such a medium is shown in Fig. 1.8(a). On the other hand, the bi-continuous media method makes use of the fact that snow is actually a two-phase medium composed of ice and air and tries to implement the discontinuities between the two continuous media. This is realized through the summation of a large number of spatial standing waves with random wave numbers, initial phases, and directions. The mean value of the wave number dictates the average grain size and its distribution defines the autocorrelation function. Various types of statistical distributions including the Gamma distribution, the log-normal

distribution and the inverse Gamma distribution have been used and reported in literature [34]. An example of a 2D cut of the reconstructed snow medium using the bi-continuous medium method is depicted in Fig. 1.8(b). However, these models fail to guarantee the macroscopic connectivity of the ice particles. Since it is not realistic to have an ice particle being surrounded everywhere by air, the macroscopic connectivity of the ice particles should be invoked. The enforcement of the macroscopic connectivity is not only important from a realistic structural view point, but also from an electromagnetic point of view. The connected particles result in a more coherent representation of the medium, which means that the phases of the fields are estimated with better accuracy. This effect is more important at higher frequencies where the dimensions of inhomogeneities are comparable to the wavelength.

(a)   (b)
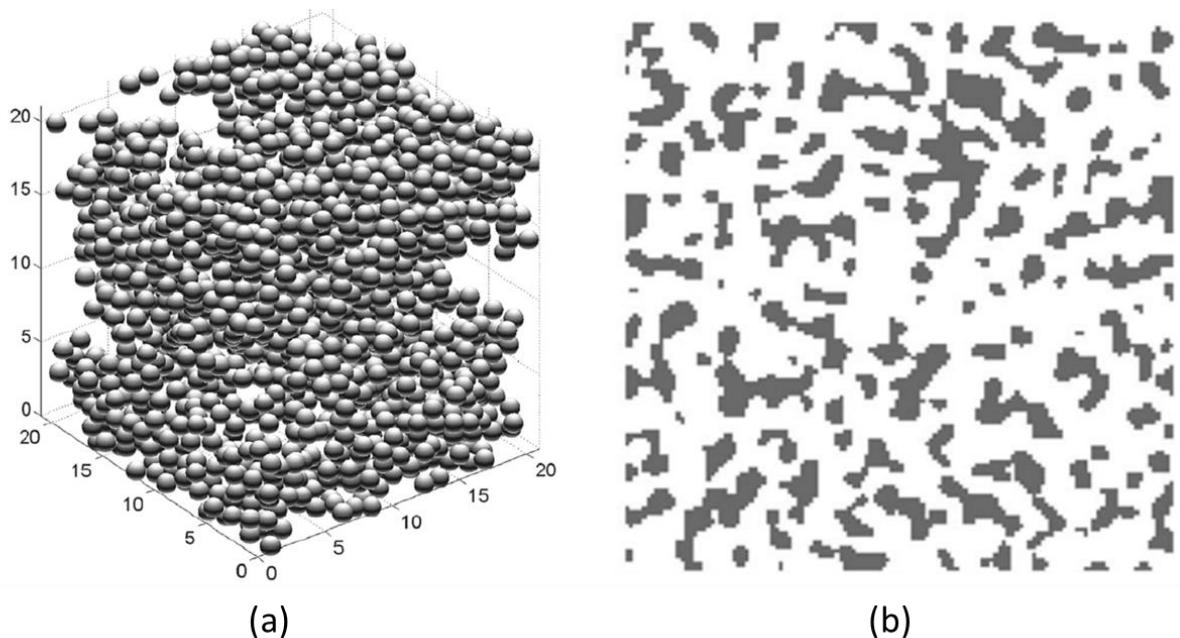
Figure 1.8 An example of a reconstructed snow medium using (a) densely-packed sticky-particles [31], and (b) a bi-continuous medium [33].

1.4. Passive vs Active Remote Sensing of Snow

For radar sensing of snow water equivalent, after the snow sample has been generated, an accurate numerical solver should be used to calculate the statistics of the forward and backward scattered fields. The choice of the operating frequency of the radar system is important because an electromagnetic wave propagating in the snow medium would not experience significant scattering by the ice particles unless its wavelength is comparable to or shorter than the dimensions of the particles. Hence, traditionally, either X- or Ku-band are used for radar remote sensing of snow because snow can produce considerable volume scattering at these wavelengths, thereby making it possible to use the measured response to obtain information about the snow depth and density. This is due to the fact that the average snow grain size is a considerable fraction of the wavelength at these frequencies. Also noting that the ice particles are densely packed, the application of a fully-coherent scattering method that accounts for multiple scattering interactions is mandatory. Several techniques have been reported in the literature for modeling radar remote sensing of snowpacks. We can categorize these techniques into empirical, semi-empirical, analytical, and numerical techniques. Empirical models depend on building a relationship between the parameters of the snow medium and the observed radar response. The main advantage of empirical models is that they are relatively fast to conduct and easy to process. The major drawback is that there is no guarantee that the same empirical model will be applicable globally under any various snow conditions. Analytical techniques do not have this limitations of the empirical approach, but they usually depend on approximate simplified models. The validity of the analytical models should be tested across different measurement campaigns to assess the applicability of the model under different snow conditions. The third category includes semi-empirical models, which usually are a hybrid mixture between the analytical technique and the empirical approach created by fitting

measured radar and snow data to the expressions provided by analytical techniques. Numerical techniques depend on solving Maxwell's equations numerically, using either differential or integral forms. The main advantage of the numerical technique over the analytical techniques is that the numerical technique does not have to employ approximations to arrive at a solution. The major drawback of available numerical-solution techniques is that they are very time consuming because the medium under test is random, dense, and complicated. Hence, developing an accurate, time-efficient numerical technique –which is the major goal of this study– is the best option for modeling such a complicated medium like snow. In principle, the characterizations offered about these techniques are equally applicable to both passive and active remote sensing scenarios [35-36].

Passive remote sensing relies on measuring the brightness temperature of the scene illuminated by the antenna pattern using a microwave radiometer [37]. The Brightness temperature is related to the physical temperature of the scene (or volume, in the case of snowpack) as well as its absorption and scattering properties. Two semi-empirical models commonly-used for relating the brightness temperature of snowpacks to snow water content are the HUT [38] (Helsinki University of Technology, also known as TKK) and the MEMLS [39] (Microwave Emission Model of Layered Snowpacks) models. The HUT model is a semi-empirical radiative transfer model that treats the whole snowpack as an equivalent homogenous medium, and has been demonstrated to lead to acceptable results at operating frequencies in the microwave spectrum (approximately up to Ku band ~ 15 GHz). In the HUT model, most of the power scattered by the snow particles travels in the forward direction, which may not provide an accurate description of scattering by ice particles when the wavelength of the electromagnetic wave travelling in the snow medium is comparable to the size of the particles. In MEMLS, the snowpack is represented by a

stack of horizontal layers of different thicknesses, snow densities, etc. The extinction coefficient of an individual slab is then calculated using empirical equations and used in the radiative-transfer equations to obtain the complete response. Other modeling approaches include the DMRT (Dense-media Radiative Transfer) model [40] and the SFT (Strong Fluctuations Technique) [41-43]. Of course, from an imaging standpoint, the spatial resolution of a microwave radiometer is quite coarse compared with that of a synthetic aperture radar (SAR): hundreds of meters for an airborne radiometer and tens of kilometers for a satellite-borne radiometer, compared with a spatial resolution of only a few meters for both airborne and spaceborne SAR systems [44]. In view of the fact that snow-covered mountainous terrains can be highly heterogeneous and spatially varied, the high-resolution capability of SAR systems becomes a major advantage for using an active microwave sensor over its passive counterpart.

The next question to consider is: which of the available theoretical models is the most appropriate for developing the accurate and computationally time-efficient numerical model that we seek in the present study? Some models, optimized specifically for active remote sensing of snow, depend on analytical approximations like the Foldy-Lax multiple scattering approximation for a densely-packed medium [45], which exploits the known T-matrix of a sphere to represent the ice particles. Such a method is computationally inefficient and fails to provide solutions for particles of arbitrary shape. Another approach is to analyze the scattering by the random snow medium by applying the radiative transfer equation, but the radiative transfer formulation [46] depends on the intensities of the scattered waves, and consequently it does not account for the information contained in the phase of the scattered field. The Dense Media radiative Transfer (DMRT) formulation is a partially-coherent technique with which a specified portion of the medium is analyzed numerically through the solution of Volume Integral Equations (VIE) to

estimate the extinction coefficient and the phase matrix accounting to the coherent near-field interactions between the ice particles. Then, the extinction coefficient and the phase matrix are inserted into the incoherent radiative transfer equations to estimate the far-field scattered field incoherently [47]. Another hybrid experimental/analytical technique was introduced in [48] where the parameters of the DMRT were estimated using empirical models. Recently, the electromagnetic scattering from a snow layer over planar ground was reported [49] using the dyadic half space Green's function. The method solves the volume integral equation through the Discrete-Dipole approximation (DDA) to estimate the scattered fields in a fully-coherent way. However, the maximum snow layer thickness is limited by the computation resources. Hence, there is a strong need and desire to develop a time-efficient, fully-coherent electromagnetic scattering computational tool for the snow cover over a rough surface and use it for mapping snow water equivalent (SWE) by airborne and spaceborne SAR systems.

1.5. Scattering By a Rough Surface

Electromagnetic scattering by a rough surface has been studied extensively over the past 40 years. The rough surface usually is characterized by the following parameters: (1) the dielectric constant of the surface material, (2) the rms (root mean square) height of the surface (s), (3) the autocorrelation function, and (4) the correlation length (l_c). It is also important to note that from electromagnetic point of view, surface roughness (rms height and correlation length) is measured relative to the wavelength, so the same surface may appear smooth at a lower frequency but appear very rough at higher operating frequencies, which is why surface roughness usually is reported in terms of ks where $k = \omega/c$ is the free-space wavenumber. In a manner similar to the earlier discussion related to scattering by the snow volume, there exists many different scattering models

for rough surfaces, which include analytical, empirical, numerical, and hybrid methods. A very good summary of the various surface scattering techniques is available in [23], and a detailed discussion of how to implement them is presented in [50-51]. Analytical methods rely on the simplification of Maxwell's equations under certain assumptions pertaining to the surface parameters. For a slightly-rough surface, where ($ks < 0.3, kl < 3$), the Small Perturbation Method (SPM) [52] is applicable. In the SPM, the surface fields are expanded into a perturbation series with n terms, with n depending on the order of the approximation, and then these surface fields are used to solve a boundary value problem to obtain the scattered field. Recently, a second-order SPM was utilized to solve for a multi-layer rough surface as in [53].

On the other hand, if the roughness scale is large compared to the wavelength but the surface can be considered to be smoothly-varying, then the Kirchhoff's Approximation [54] can be made. Two types of approximation are used in practice, one for the case when $ks > 3$, and it is called the Geometric Optics (GO) [55] approximation, and the second is for when $ks < 3$, which is called the Physical Optics (PO) [56] approximation. Since the rough surface acts as a boundary between two different media, the solution for the scattered EM field is equivalent to solving the boundary value problem by applying the appropriate boundary conditions, namely imposing the continuity of the tangential electric and magnetic fields across the boundary. Consequently, we can end up with an integral equation for the scattered fields with the surface fields as the only unknowns. Using the assumption of gentle variation of the surface height function, we can simplify the integral and achieve a closed-form expression. Moreover, a realistic surface can be considered as a multi-scale roughness surface whose actual roughness distribution consists of the superposition of multiple different roughness profiles. To solve for the scattering from such a surface, the Two-Scale Model [57] is commonly used by representing the surface as a combination

18

of a small-scale surface that can be solved using SPM and a large-scale surface that can be solved using the KA method, and then the total normalized backscattering coefficient is calculated using the superposition of the small- and large- scale surfaces. However, if the surface does not satisfy the validity region of this technique, the results would be inaccurate. Alternatively, measured data can be used to build an empirical model. The Oh model [58] is the most-used empirical model when it comes to rough surface scattering. It describes the polarmetric backscattering coefficients $(\sigma_{vv}, \sigma_{hh}, \sigma_{vh})$ using the measured data for different incidence angles and at different frequencies (L, C, and X bands). Another widely used empirical model is the Dubois model [59], which is basically a simplified version of the Oh model realized by neglecting the cross-pol component and optimizing the equations for a certain range of surface parameters, leading to simpler equations for σ_{vv} and σ_{hh}. Both the analytical and empirical methods suffer from some of the simplifications used in their implementation. Alternatively, numerical-based scattering models can be used because they are more accurate and without the limitation of a specific region of validity, but they require more rigorous implementation techniques. One way to improve the accuracy of the analytical techniques is by using a hybrid numerical-analytical method such as the Improved Integral equation Model (I2EM) [60], which is one of the most-commonly used models. The I2EM computes the backscattering or the bistatic scattering coefficient for any arbitrary roughness profile. The main advantage of the I2EM is that it solves the integral equation and accounts for the effects of shadowing through a pre-defined shadowing function. For more accurate results, complete numerical methods should be used. Numerical computation of the scattered fields from a rough surface is a tough problem because the rough surface is usually assumed to be infinite in extent which requires either proper tapering of the input or the use of periodic boundary conditions in order to emulate the large extent of the rough surface. As mentioned earlier, we can come up

with an integral equation to solve for the unknown surface fields/currents using the Method of Moments (MoM). Usually, the MoM matrix is dense and it requires quite a bit of time to be filled and its inversion can be difficult. The Sparse-Matrix Canonical-Grid (SM-CG) [61-63] method is a time-efficient technique to solve for the scattered field from a rough surface by dividing the elements of the MoM matrix into near and far elements. For the far-elements, the Green's function contained in the formulation is approximated so as to speed up its calculation and result in a sparse far-field matrix that requires less memory and consequently less simulation time. The SM-CG was initially used for only 2D problems, then it was extended to speed up a generalized 3-D form which is called the Numerical Maxwell Model in 3-D (NMM3D) [64-67]. Even though current numerical techniques, especially the NMM3D, provide very good accuracy, they are still hard to implement and time-consuming to build. For the snow problem central to this study, given all the advancement in the commercial computational EM tools available today (like HFSS, CST, FEKO, COMSOL, etc.), the question is: should we base our solution using these commercial tools or should we to develop codes of our own? The answer of this question will come in the following chapters.

1.6. Dissertation Overview and Contributions

The main objective of this thesis is to develop a complete forward scattering model for snowpack over a rough surface. An overview of the topics discussed in this thesis is portrayed in Fig.1.9. To accomplish the stated goal, four steps should be implemented: (1) reconstruction of the snow medium in 3-D space, (2) solving for scattering by the snow layer alone, (3) solving for scattering by the rough surface alone, and (4) combining the two previous responses in a phase-coherent manner.

Chapter 2 discusses the physics-based reconstruction method of the computer generated samples. To redress the shortcomings of the existing reconstruction methods, we propose the use of the Lineal-path function together with a 3D spatial exponential correlation function to build the snow sample and assure the connectivity of the ice particles [68] in the reconstructed snow medium. The Lineal-Path function is the probability of finding a straight line (a chord) within the medium that connects two points [69] such that every single point along this line belongs to the same phase of the medium. An example of the reconstructed medium is shown in Fig. 2.10 [70].

Chapter 3 presents the computationally-tractable fully-coherent method used to solve for scattering by an arbitrarily-thick snow layer. We propose a 3-D generalized version of the Statistical S-matrix Wave Propagation in Spectral Domain (SSWaP-SD) technique. The SSWaP-SD was used to analyze the long distance propagation in a 2-D sparse random medium, which offers a time-efficient simulation technique [71] that was inspired by a wave propagation technique used for propagation in foliage [72]. The SSWaP-SD depends on dividing the medium into horizontal slabs and representing each slab with an N-dimensional fully-polarmetric bistatic
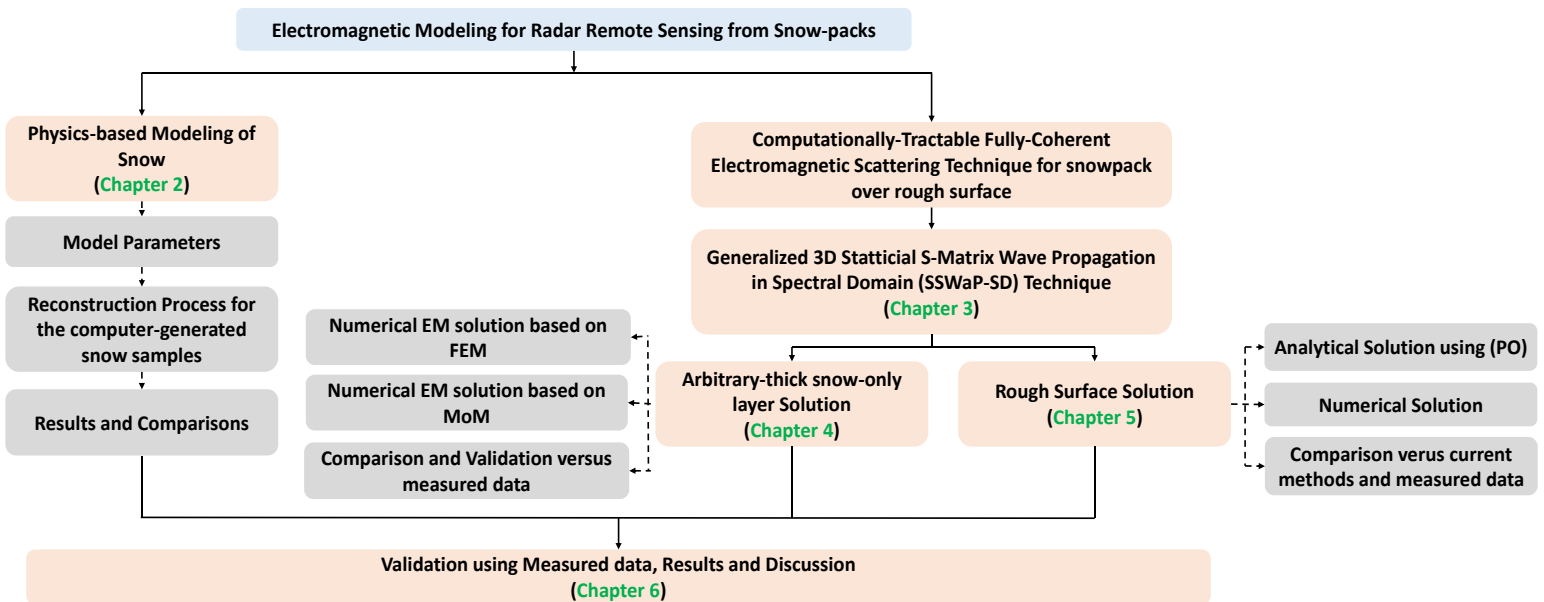
Figure 1.9 Overview of the topics that are covered in this dissertation.

scattering matrix that relates the forward and backward fields. The individual elements in the S-matric are calculated by decomposing the scattered fields at the top and bottom plane into the corresponding plane waves [73] and obtaining the relation between the scattered and incident plane wave. The rough surface also is represented by a reflectivity matrix. These matrices are then cascaded coherently to give the total forward and backward scattering patterns.

The numerical solver for a single snow-only slab is reported in Chapter 4. Each individual snow slab is solved numerically using both the Finite Element Method (FEM) and the MoM method [74]. The results of applying the two techniques are compared to one another and good agreement between them is observed. The main task of the solution method is to account for all the multiple interactions inside each slab, and then the cascading algorithm insures that the multiple interactions between the different slabs are all taken into account. With this approach, we execute a fully-coherent solver for the scattering from the snowpack. Moreover, using the assumption that each layer constitutes a statistically-homogenous medium, we can generate the statistics of the building block S-matrix and use it to emulate other slabs and calculate the scattering patterns for any arbitrary thickness of the snow layer [75].

Chapter 5 discusses how the rough surface reflectivity matrix [76] is calculated using both an analytical method based on a modified Physical Optics (PO) approximation [77] and a numerical solution based on MoM through a commercial full-wave software (CADFEFKO) [78].

Chapter 6 presents the results and validation of our model using two different measurement campaigns at X- [79] and Ku- [80] bands. In addition to the validation and results, we also report a statistical model for the snow slab and the rough surface which can be used as an initial step for the inversion algorithm. Lastly, conclusions are drawn and future work is listed.

Chapter 2

Reconstruction of Physics-Based Computer-Generated Snow Samples

2.1 Introduction

This chapter covers the proposed physics-based reconstruction method used to create 3-D computer-generated samples of the snow volume. The snow is a two-phase medium comprised of ice and air. The main purpose of this chapter is to describe how to reconstruct a 3-D matrix representing the connected ice particles in the air background. Preserving the macroscopic connectivity of the ice particles is essential for realistic reconstruction of the computer-generated samples. As discussed in the introduction chapter, many of the models reported in the literature fail to guarantee this important macroscopic property. Because it is not realistic to model the ice particle as surrounded everywhere with air, the macroscopic connectivity of the ice particles should be invoked. Enforcement of the macroscopic connectivity condition is not only important from a realistic structural view, but also from an electromagnetics point of view. The connected particles result in a more coherent representation of the medium, which means that the phases of the EM fields are estimated with better accuracy. This consideration is particularly important at the higher microwave frequencies where the sizes of the in-homogeneities are comparable with the EM wavelength.

Our proposed reconstruction method rectifies the shortcoming of currently available reconstruction methods by enforcing a second-order clustering correlation function, in addition to the usual auto-correlation function commonly used in 3-D reconstruction .

2.2 Proposed Reconstruction Method

The snow medium can be visualized as a collection of connected ice particles in an air background. To reconstruct a snow sample with sufficient accuracy to satisfy the desired EM scattering environment, we should use a random process with certain parameters designed to match the measured statistics of the snow medium. To preserve a specific macroscopic characteristic, like the connectivity of particles in a two-phase dense random medium, our reconstruction process should include all the zeroth, first, and second order statistics of the spatial environment [81]. The zeroth-order statistic represents the average probability for finding an ice particle at any specified position in the medium, which is defined in terms of the volume fraction Φ_v. The volume fraction of snow usually varies between 10% and 50%. Next, the first-order statistic refers to the Two-Point Correlation Function (TPCF) representing the joint probability of occurrence of two particles present simultaneously while separated by a specified distance. Microscopic observations indicate that the TPCF can be modeled as an exponential function with a correlation length (l_c) whose value is proportional to the average measured particle size (~ $0.5mm$ [82] ~$\lambda/40$ at 14 GHz). The exact value of the factor relating l_c to the grain size depends on snow type (new, densified, hard, etc.) [83]. Even though the TPCF indicates the probability that two points, at specified locations, are located in the same phase (ice or air), it is still a point-to-point probability. In other words, there is no information included in the TPCF about the possible presence of other particles in between those two points. Therefore, a clustering
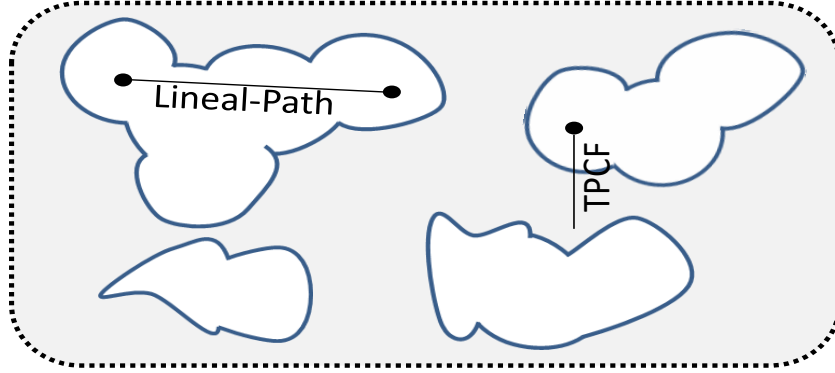
Figure 2.1 Depiction of the difference between the Two-Point Correlation Function (TPCF) and the Lineal-Path function.

correlation function (second-order statistic) should be used in conjunction with the TPCF to achieve an accurate realization of the snow volume. One example of such a clustering correlation function is the Lineal-Path correlation function which assigns a probability to finding a straight line (a chord) connecting two specified points such that all the other points of this line lay completely within the same phase (ice or air), as depicted in Fig. 2.1. Thus, the Lineal-Path function can be considered an indicator of how snow particles form clusters. It might also be visualized as a spatial filter to the autocorrelation function. Interestingly, the same method is used by civil engineers to model porous sand stone model [84]. The Lineal-Path function is given by the following form:

$$S_l(r) = \begin{cases} \phi_v \left(1 - \dfrac{r}{l_g}\right) & r < l_g \\ 0 & Otherwise \end{cases} \tag{2.1}$$

where, S_l is the spatial Lineal-Path function at location r in the space under consideration, ϕ_v is the volume fraction, and l_g is the average chord length. As shown in Eq. (2.1), the Lineal-Path function is defined by two parameters: (1) the volume fraction (ϕ_v), and (2) the average chord length (l_g). Usually, the Lineal-path function is enforced iteratively by the simulated annealing algorithm wherein random chords are drawn into the system and the current Lineal-Path function
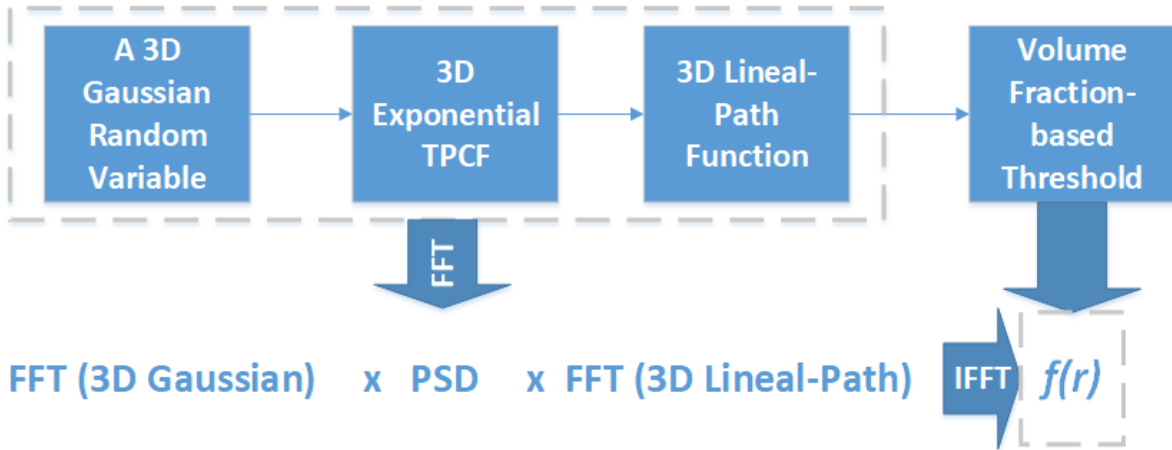
Figure 2.2 The reconstruction random process of the snow medium.

is evaluated and compared with the desired one. Then, the difference between the current and desired correlation function is minimized by shuffling the positions of some of the points iteratively until a specific accuracy is achieved [85].

Instead of the iterative approach, we propose to apply a direct approach by using the Lineal-Path function as a spatial filter for the Power Spectral Density (PSD) of the 3-D exponential function (TPCF). The complete process is demonstrated in Fig. 2.2. As a first step a 3-D Gaussian random number is generated, then the TPCF (3-D exponential) is enforced, then filtered using the Lineal-path correlation function and a volume fraction-based threshold is applied at the end. It is worth noting that the frequency-domain implementation of the process is much easier to execute than the spatial-domain implementation. The equivalence between the two domains is depicted in Fig. 2.2. After performing a Fourier transformation on each of the 3 initial blocks and multiplying their spectra together, application of the Inverse Fourier Transform (IFT) and assignment of the appropriate volume fraction leads to the desired result. Since the Lineal-Path function works as a spatial filter to smooth out the sharp discontinuities and improve the overall connectivity, the chord length (l_g) is chosen to be longer than the average grain size (or, about 1.5 times the correlation length (l_c)). This reconstruction approach may cause the auto-correlation function to deviate
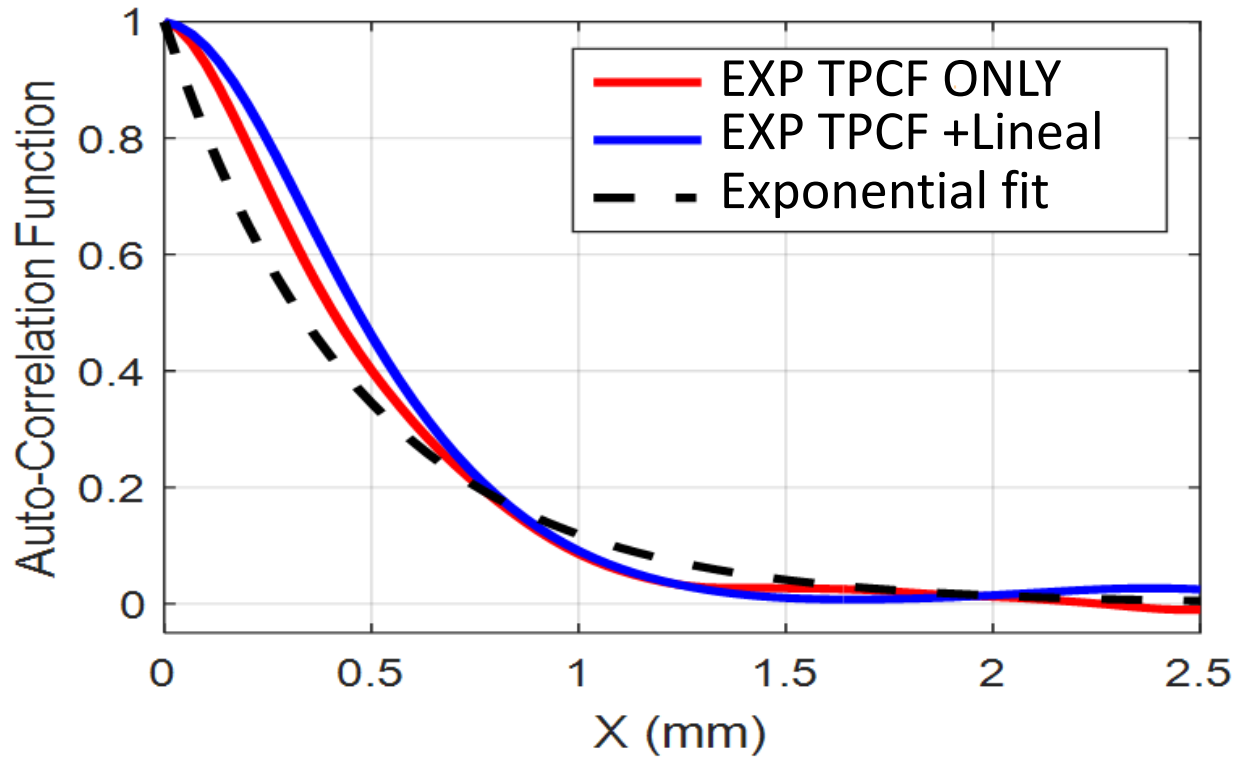
Figure 2.3 Spatial Auto-Correlation Function of the constructed snow medium versus distance.

slightly from the exact exponential fit, but it offers significant improvement on modeling the ice particles' macroscopic connectivity for a specified value of the snow volume fraction. An example of the resultant auto-correlation function is shown in Fig 2.3. An x-direction cut for the auto-correlation is shown using two realizations: (1) the exponential TPCF alone and (2) using the exponential TPCF in addition to the Lineal Path. As expected, the combined autocorrelation/lineal path function exhibits a small deviation from the exact exponential fit, as expected, but the connectivity of the particles is much better represented by the combined function, as demonstrated in Fig. 2.4 for a $16cm \times 16cm \times 3cm$ reconstructed snow sample with $\phi_v = 0.5$. The ice particles stick to each other forming clusters and these clusters are connected to each other to build the snow layers. In Fig. 2.4, even though the encircled particles appear to be floating and unconnected to others, they are actually connected to ice particles in other layers or in adjacent sections. The
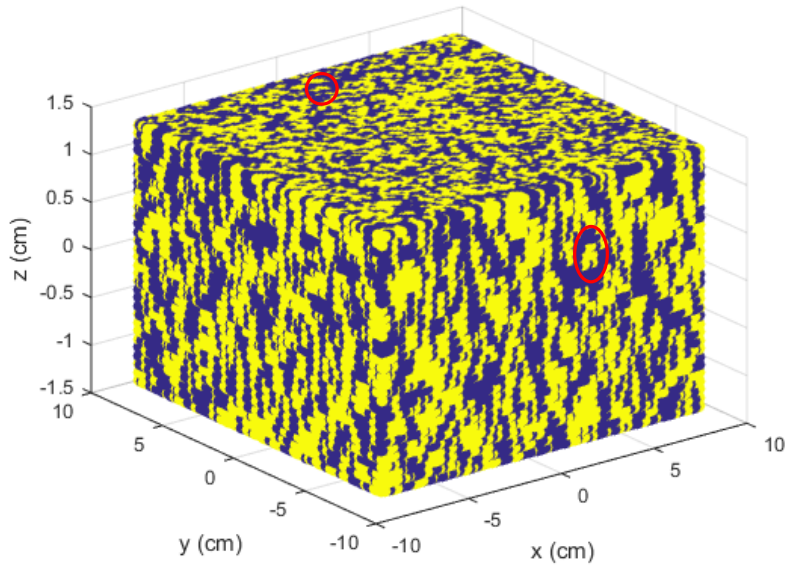
Figure 2.4 3D sample of reconstructed snow media with 50% volume fraction using both the exponential correlation and Lineal-path functions (Yellow denotes Ice and blue for Air).

aforementioned procedure was used to reconstruct many other realizations, the majority of which resulted in a similar behavior. The procedure did not provide adequate realizations for snow volumes with very low volume fractions. In such situations, invoking the Lineal-path has less impact on the connectivity [86], necessitating that we enforce higher-order clustering correlation functions to obtain better overall connectivity of the particles in snow with small volume fractions.

Another way to show how enforcing the Lineal-path function improves the overall connectivity is to show a 2-D cut of a reconstructed medium using the 3D exponential correlation function with and without the Lineal-path component. Such a comparison is shown in Fig. 2.5, significantly better macroscopic connectivity is realized by the combined correlation function approach (Fig. 2.5 (b)) compared to the sample reconstructed using the exponential correlation function without the Lineal-Path function (Fig. 2.5 (a)), where gray points are ice particles and black dots represent air-filled locations. It is worth noting here that the correlation length was set

TPCF ONLY   TPCF+Lineal Path

(a)   (b)
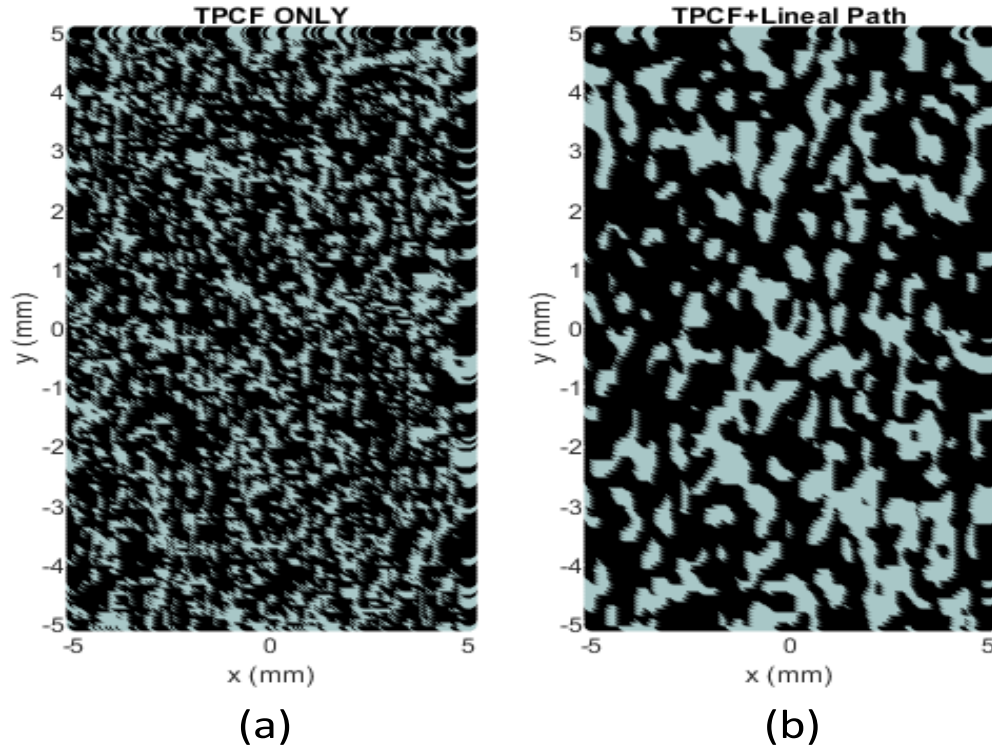
Figure 2.5 2D sample of reconstructed snow media with 40% volume fraction using (a) the exponential TPCF only, and (b) both the exponential TPCF and Lineal-path functions. Gray represents an ice particle and black is for air.

to be the same while generating the two realizations. However, the application of the Lineal Path function makes the sample shown by Fig. 2.5 (b) appear as if its average grain size is larger due to the clustering and spatial filtering effects of the Lineal-path function.

In addition, to examine the effect of the average chord length (l_g) on the overall PSD of the reconstructed sample, we varied l_g to be $0.1mm$ and $0.8\ mm$ while keeping the volume fraction and the correlation length the same. Then, the overall PSD of the reconstructed samples in both cases are shown in Fig. 2.6.
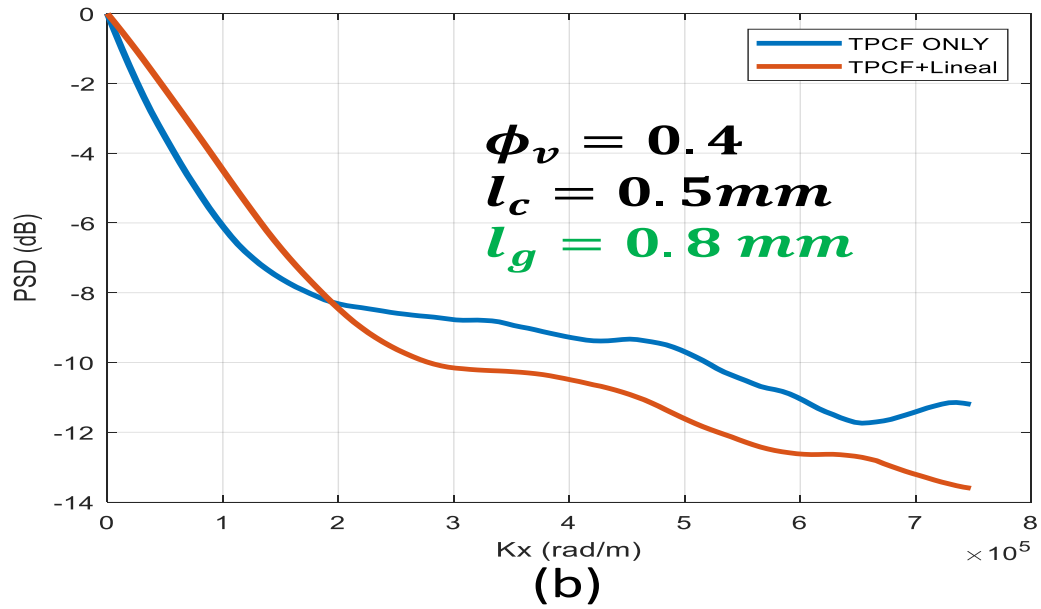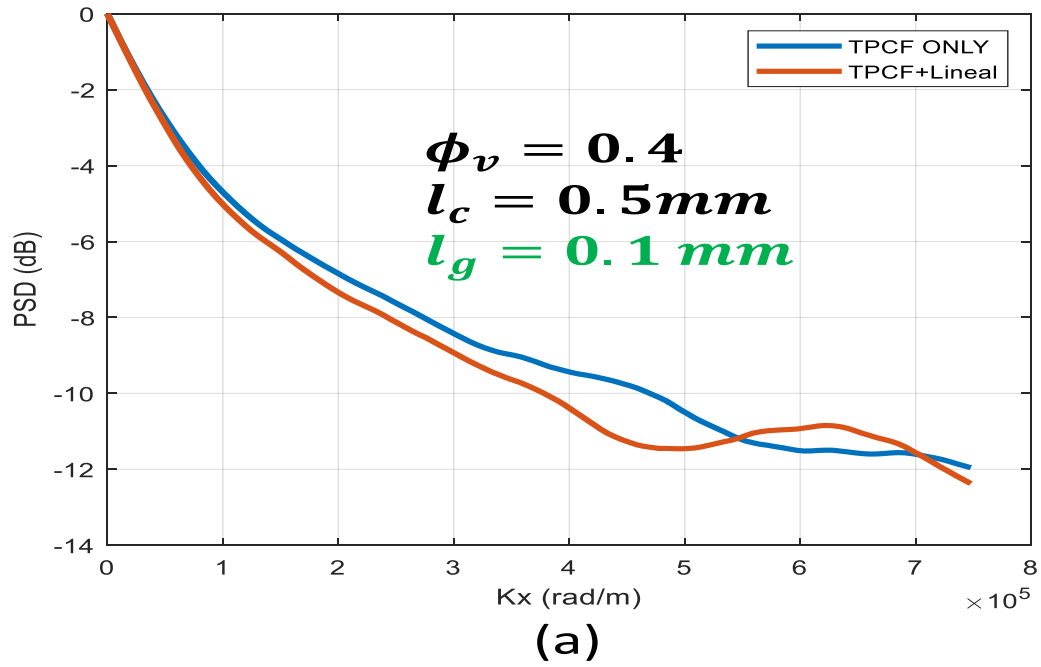
Figure 2.6 The Power Spectral Density (PSD) of a reconstructed snow sample with volume fraction of 40%, correlation length (l_c) of 0.5mm, and average chord length (l_g) of (a) $0.1\ mm$ and (b) $0.8\ mm$.

As anticipated, selecting l_g to be 0.1 mm which is five times smaller than the correlation length have minimal effect on the overall reconstructed PSD as depicted in Fig. 2.6 (a) and mainly the 3D exponential TPCF is dominating the reconstruction process. However, selecting l_g to be larger than the correlation length changes the PSD response of the overall reconstructed sample compared to the exponential case. As observed in Fig. 2.6 (b), the power contained in low frequency components are higher when both the Lineal-path and the exponential TPCF are used together compared to when the exponential TPCF is used alone. This is because that the Lineal-path function works as a spatial filter that smooths out the un-realistic discontinuities in the medium that occurs at higher spatial-frequency. Such reasoning could be even further emphasized by the observation of the power in higher spatial-frequency component which is again minimized by using the Lineal-path on top of the exponential TPCF compared to using the TPCF alone as shown in Fig. 2.6 (b).

To show the capability of our model to generate snow samples with different volume fractions, 2-D cuts with volume fractions of 30%, 40%, and 50% are depicted in Fig. 2.6 from left to right, respectively. In Fig. 2.7, the yellow points denote ice particles and the blue locations denote air.
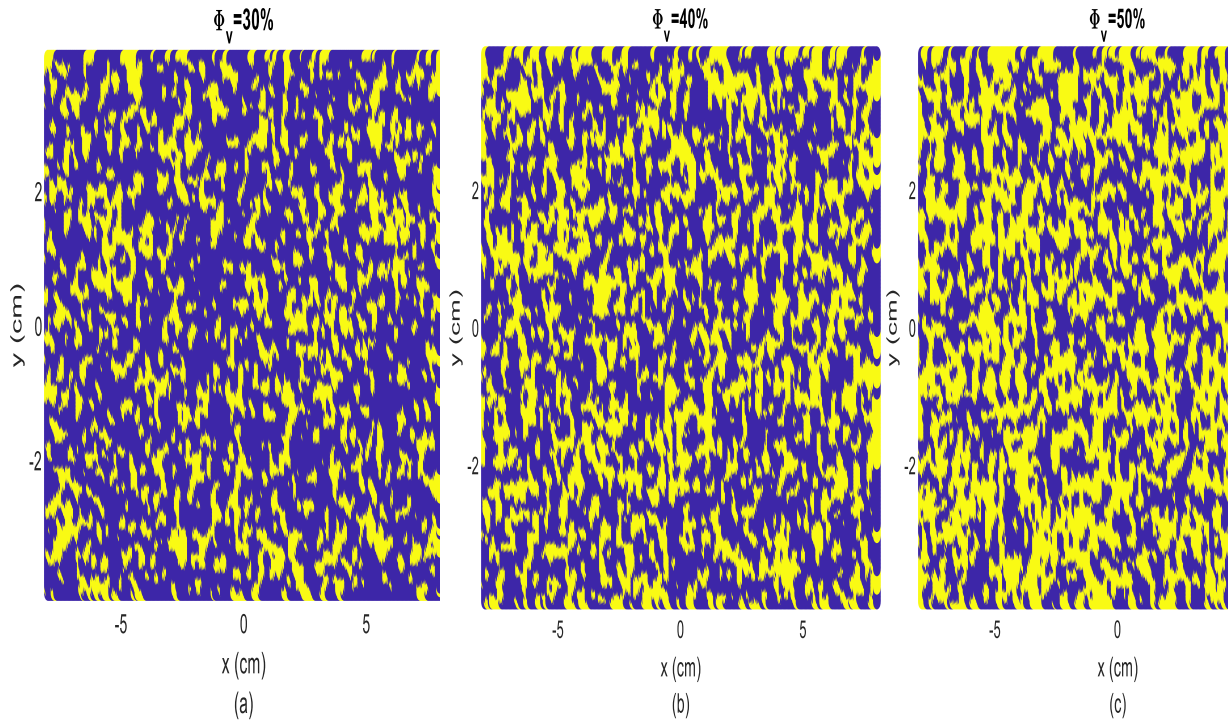
Figure 2.7 2D samples of reconstructed snow media with (a) 30%, (b) 40%, and (c) 50% volume fraction (Yellow denotes Ice and blue for Air).

2.3 Comparison with Measurement

To evaluate the validity of our proposed model, we compared a 2-D sample of our reconstructed medium with a real snow sample [87] with equivalent parameters (volume fraction of 30% and average grain size of 0.5mm). Figure 2.8 (a) compares our model- reconstructed medium to the real snow sample shown in Fig. 2.8 (b). The two images exhibit a great deal of similarity. Additionally, an example of the 3-D reconstructed medium is shown in Fig. 2.8(a) and is qualitatively compared to snow samples measured by X-ray computed tomography [88] in Fig. 2.8(b) and Fig. 2.8(d).
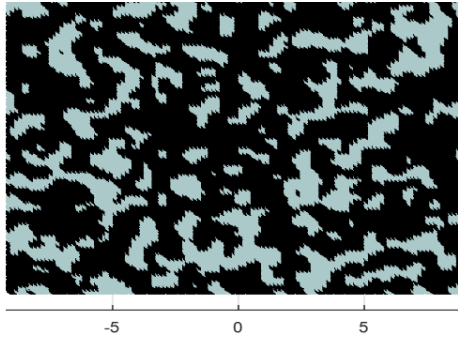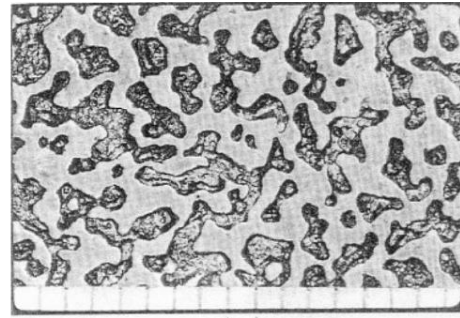
(a)   (b)

Figure 2.8 Microstructure image of 2D sample of (a) our reconstructed snow, and (b) real snow.
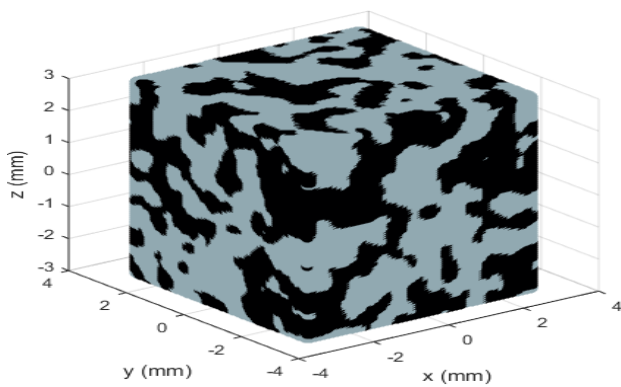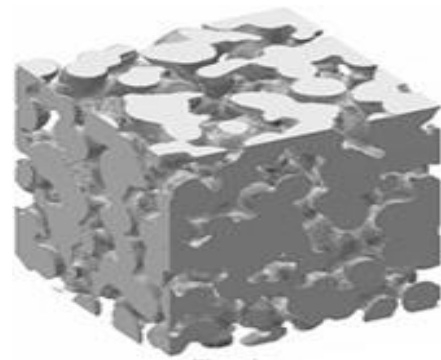
(a)   (b)
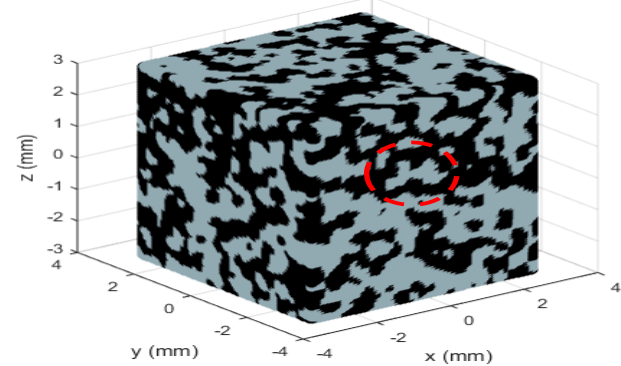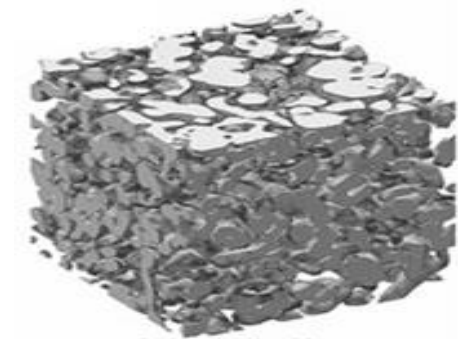
(c)   (d)

Figure 2.9 A qualitative comparison between 3D samples of reconstructed (left) and measured (right) snow media with 50% volume fraction for two different grain sizes; 0.26 mm (top) and 0.16 (bottom).

2.4 Conclusions

In this chapter, a new physics-based reconstruction method is used to generate 3-D computer samples of snow media. The proposed technique uses a Lineal-path function as a spatial filter of the spectral domain of the medium, and it is generated by enforcing the 3-D exponential auto-correlation function. After applying both the Lineal-path and the auto-correlation functions, a volume fraction-based threshold is applied to form the 3-D matrix representing the snow sample. The reconstructed samples assure the necessary macroscopic connectivity of the ice particles. At the end, our reconstruction method uses 3 parameters to generate the snow sample: (1) the volume fraction (ϕ_v), (2) the correlation length (l_c), and (3) the average chord length (l_g). Several realizations are reported and compared to both 2-D and 3-D images of real snow volumes, showing very good resemblance and reconstruction.

Chapter 3

Computationally-Tractable Full-Wave Electromagnetic Solver for Snow-packs

3.1. Introduction

Over the past four decades, an extensive effort has been devoted towards the development of solutions for full-wave electromagnetic propagation in a dense random medium. As discussed in the introductory chapter, several techniques have been implemented, either analytically, empirically, numerically, or a hybrid of the aforementioned list. While analytical solutions offer an easy and direct way to estimate the EM response, they usually incorporate simplifications that undermine their accuracy and applicability. In contrast, empirical models can be very accurate because they are based on measured data, but their applicability is limited to snow conditions similar to those of the snowpacks that had been measured and used to generate the empirical models. Thus, the validity of empirical models is not necessarily transferrable to snowpacks with different characteristics. Standard numerical methods are conceptually an attractive option because they rely on solving Maxwell's equations, but in practice, they are usually computationally-extensive and time-consuming. In this chapter, we present a time-efficient fully-coherent full-wave solver for a snowpack of arbitrarily thickness using a technique called the Statistical S-matrix Wave Propagation in Spectral Domain (SSWaP-SD) method.
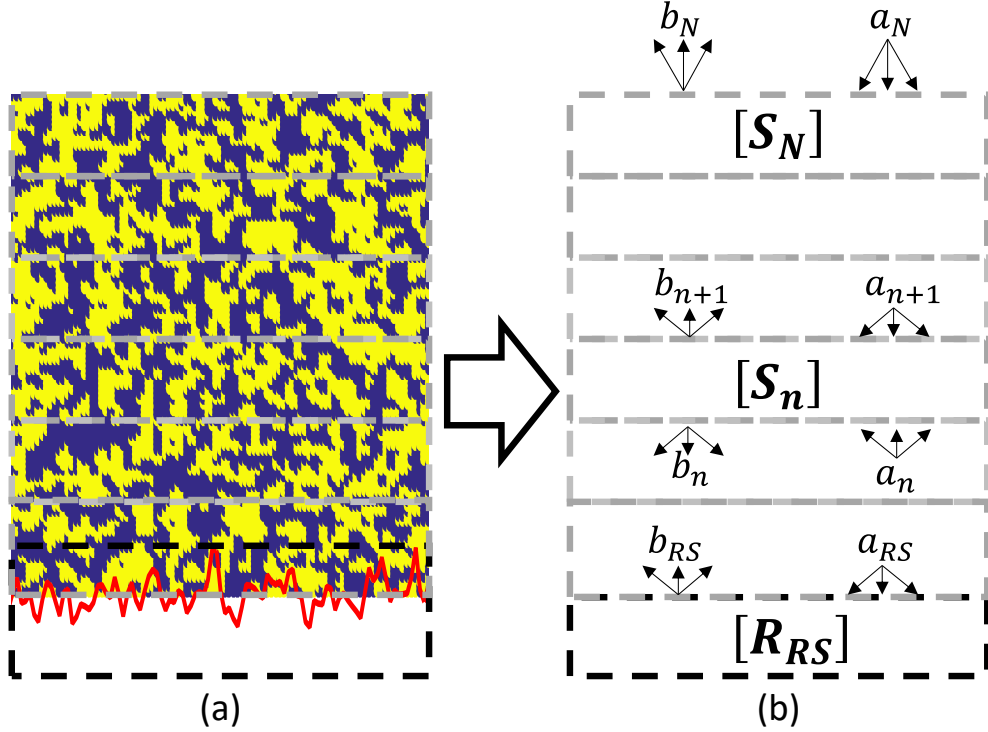
Figure 3.1 Basic Procedure in SSWaP-SD technique. (a) Discretization of the random medium into N slabs. (b) Representing each slab with an S-matrix.

3.2. Basic Structure of the SSWaP-SD Technique

The SSWaP-SD method is implemented in 3 basic steps: (1) discretizing the medium into slabs with a finite thickness and specified width, (2) representing each slab by an N-dimensional bi-static scattering matrix, and (3) cascading these matrices together to obtain the overall forward and backward scattered field. This process is summarized in Fig. 3.1. In our case, the medium inside the individual slabs can be either a layer of snow or the underlying rough surface.

In order to discretize the medium correctly, the slab size should be chosen to be large enough to contain enough statistical and structural characteristics of the random medium and small enough to render the simulation time feasible. For simplicity, we denote the slab dimensions $W_x \times W_y \times L$ as $W_x = W_y = W_s$ or W_{RS} for snow and the rough surface, respectively. Of course, the
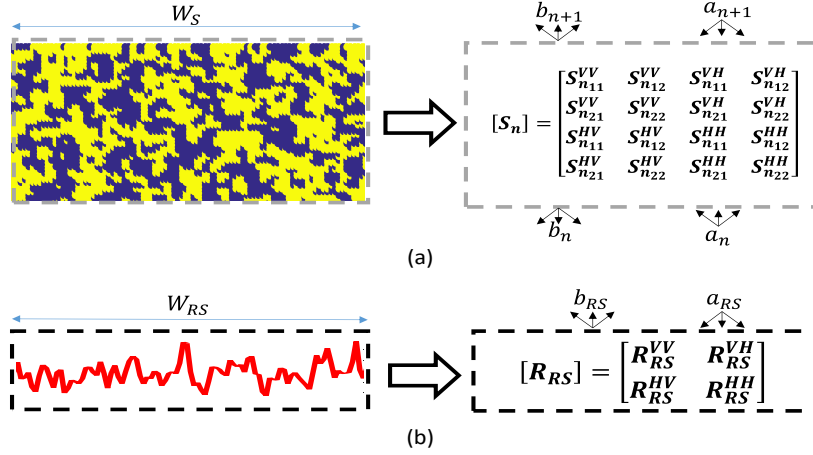
Figure 3.2 Representation of (a) snow slab with an N-dimensional polarimetric scattering matrix, (b) rough surface with a polarimetric reflectivity matrix.

dimensions L, W_s, and W_{RS} should all be much larger than the correlation length of the medium. Ideally, the width would be chosen to be infinite in extent so as to give a realistic view of the snow sample, but that would make the problem computationally intractable. To reduce the errors due to edge effects for a finite-width slab, W can be chosen to be on the order of multiple hundreds of wavelengths, as proposed in [68], for both lateral dimensions, along with proper tapering of the incident wave. However, even with these constraints, the application of numerical technique remains computationally-impractical. To circumvent this issue, periodic boundary conditions are applied along the lateral directions to eliminate the diffraction effects at the slab boundaries.

After the discretization, each snow slab is represented by a bistatic scattering matrix ($[S_n]$) that relates the forward and backward scattered waves at the input and output planes, and the rough surface slab is represented by a reflectivity matrix ($[R_{RS}]$), as depicted in Fig. 3.2. To better understand how to form the S-matrix of each individual slab, let us examine a general snow slab as in Fig. 3.2(a). Each slab is excited by a plane wave (acting as a port) entering the slab from one side and then the fields present in the slab are observed at the top and bottom layers of the slab.

These fields are then decomposed into plane-wave components by performing a 2-D FFT. Specifically, the ratio between the scattered field at a specific direction (i.e. port j) to the incident field at the prescribed direction (i.e. port i) represent an individual element (S_{ji}) in the complete S-matrix representing the slab. Then, we repeat the same process for all other directions. Generally, we can express the spatial transverse electric field at the nth plane as follow:

$$\bar{E}_t^n(x, y) = E_x^n(x, y)\,\hat{x} + E_y^n(x, y)\,\hat{y} \tag{3.1}$$

which can be transformed into the spectral domain by taking the Fourier transform:

$$\tilde{E}_t^n(k_x, k_y) = \tilde{E}_x^n(k_x, k_y)\,\hat{x} + \tilde{E}_y^n(k_x, k_y)\,\hat{y} \tag{3.2}$$

For a plane wave propagating in the direction $\bar{k} = k_x\hat{x} + k_y\hat{y} + k_z\hat{z}$, and in accordance with Gauss's law, the z-component of the field is represented by

$$\tilde{E}_z^n(k_x, k_y) = -\frac{1}{k_z}\left(k_x\tilde{E}_x^n(k_x, k_y) + k_y\tilde{E}_y^n(k_x, k_y)\right) \tag{3.3}$$

Hence, we need to determine only $E_x^n(x, y)$ and $E_y^n(x, y)$ to estimate the total field. To decompose the field into H and V polarizations [70], we start by writing down the horizontal and vertical unit vectors as follow

$$\hat{h} = \frac{\hat{z} \times \hat{k}}{|\hat{z} \times \hat{k}|} = -\frac{k_y}{k_t}\hat{x} + \frac{k_x}{k_t}\hat{y}$$

$$\hat{v} = \hat{h} \times \hat{k} = \frac{k_x k_z}{k_t k_o}\hat{x} + \frac{k_y k_z}{k_t k_o}\hat{y} - \frac{k_t}{k_o}\hat{z} \tag{3.4}$$

and the decomposed H/V-polarized components in the spectral domain can be expressed as $\tilde{E}_p^n(k_x, k_y) = \tilde{E}^n(k_x, k_y) \cdot \hat{p}$, and p is either h or v. Explicitly, we can write

$$\tilde{E}_H^n(k_x, k_y) = -\frac{1}{k_t}\left(k_y\tilde{E}_x^n(k_x, k_y) - k_x\tilde{E}_y^n(k_x, k_y)\right)$$

$$\tilde{E}_V^n(k_x, k_y) = \frac{k_o}{k_t k_z}\left(k_x\tilde{E}_x^n(k_x, k_y) - k_y\tilde{E}_y^n(k_x, k_y)\right)$$

(3.5)

where $\overline{k}_t = k_x\hat{x} + k_y\hat{y}, k_z^2 = k^2 - k_t^2$. The total field can be expressed as the sum of the two polarized components as

$$\tilde{E}^n(k_x, k_y) = \tilde{E}_H^n(k_x, k_y)\,\hat{h} + \tilde{E}_V^n(k_x, k_y)\,\hat{v}$$

(3.6)

Therefore, in general, by just taking the FFT for spatial fields, we can write the field as a combination between the two polarization and a summation (integration) over all the plane wave components

$$E_n^p(x, y) \approx \iint\limits_{k_t=-k_o}^{k_o} \left[a_n^p(k_x, k_y)\, e^{j(k_x x + k_y y)}\right] dk_x dk_y$$

$$+ \iint\limits_{k_t=-k_o}^{k_o} \left[b_n^p(k_x, k_y)\, e^{j(k_x x + k_y y)}\right] dk_x dk_y$$

(3.7)

where a_n^p and b_n^p denotes the spectral coefficients of a plane wave at the input of the nth slab with transverse wave number $\overline{k}_t$ propagating in the +z direction (inward) and –z (outward) direction. Since the FFT is taken for the fields on the top and bottom planes of the slab, the solution domain looks periodic in space which matches the assumption of periodic boundaries in the lateral dimensions. The spectral resolution is inversely proportional to the width, as $\Delta k_{x,y} = 2\pi/W_{x,y}$ and the maximum value of $k_{x,y}^{max} = \frac{2\pi}{\Delta x,y}$. Therefore, the wider the slab, the higher the spectral resolution. It is also worth mentioning that the integration limits in Eq. (3.7) theoretically extend from -∞ to ∞. However, in practice the limits are chosen such that $|k_t| \le k_o$, so as to assure a real value for k_z. In other words, the propagating modes are only included in this expansion. Also, to

avoid singularities in the Green's function, the slab dimensions $W_{x,y}$ are chosen such that they are not multiple integer of the wavelength. From Eq. (3.6), the total field is the vector sum of both the V and H polarizations, so Eq. (3.7) can be cast into four terms to represent the total field at the input plane of the nth slab

$$\bar{E}_n^{total}(r_{t_n}) \approx \int\int_{k_t=-k_o}^{k_o} \left\{ \begin{matrix} \left(a_n^V(\bar{k}_t)\hat{v} + a_n^H(\bar{k}_t)\hat{h}\right) \\ + \\ \left(b_n^V(\bar{k}_t)\hat{v} + b_n^H(\bar{k}_t)\hat{h}\right) \end{matrix} \right\} e^{j(\bar{k}_t \cdot \bar{r}_{tn})} dk_t \tag{3.8}$$

where $\bar{r}_{t_n} = x_n\hat{x} + y_n\hat{y}$ is the position vector at the input plane of the nth slab. Similarly, the same procedure is applied at the output plane of the nth slab so as to decompose the spatial field into the sum of a set of four spectral components, of which two are propagating inward the slab: $(a_{n+1}^V(\bar{k}_t), a_{n+1}^H(\bar{k}_t))$, and the other two propagating outward from the slab: $(b_{n+1}^V(\bar{k}_t), b_{n+1}^H(\bar{k}_t))$. In our simulation, Eq. (3.8) is discretized and the integration is replaced by a summation. Both W and L of the slab are chosen such that the difference between the total field in Eq. (3.8) and the numerically-acquired field distribution is within 1%.

Consequently, the scattering matrix is filled by relating the calculated spectral coefficients to those of the incident plane wave, and since both might have different polarizations, a general form of the S-matrix that relates the p polarized scattered fields to the q polarized incident field is expressed as

$$\begin{pmatrix} \bar{b}_n^p \\ \bar{b}_{n+1}^p \end{pmatrix} = \begin{pmatrix} \bar{\bar{S}}_{11}^{pq}(k_t^i, k_t^s) & \bar{\bar{S}}_{12}^{pq}(k_t^i, k_t^s) \\ \bar{\bar{S}}_{21}^{pq}(k_t^i, k_t^s) & \bar{\bar{S}}_{22}^{pq}(k_t^i, k_t^s) \end{pmatrix} \begin{pmatrix} \bar{a}_n^q \\ \bar{a}_{n+1}^q \end{pmatrix}$$

$$\begin{pmatrix} \bar{b}_n^p \\ \bar{b}_{n+1}^p \end{pmatrix} = \bar{\bar{S}}^{pq}(k_t^i, k_t^s) \begin{pmatrix} \bar{a}_n^q \\ \bar{a}_{n+1}^q \end{pmatrix} \tag{3.9}$$

Therefore, the total fully-polarized S-matrix representing each slab is explicitly calculated as in Eq. (3.10)

$$\bar{\bar{S}}_n = \begin{pmatrix} \bar{\bar{S}}_{11}^{VV}(k_t^i, k_t^s) & \bar{\bar{S}}_{12}^{VV}(k_t^i, k_t^s) & \bar{\bar{S}}_{11}^{VH}(k_t^i, k_t^s) & \bar{\bar{S}}_{12}^{VH}(k_t^i, k_t^s) \\ \bar{\bar{S}}_{21}^{VV}(k_t^i, k_t^s) & \bar{\bar{S}}_{22}^{VV}(k_t^i, k_t^s) & \bar{\bar{S}}_{21}^{VH}(k_t^i, k_t^s) & \bar{\bar{S}}_{22}^{VH}(k_t^i, k_t^s) \\ \bar{\bar{S}}_{11}^{HV}(k_t^i, k_t^s) & \bar{\bar{S}}_{12}^{HV}(k_t^i, k_t^s) & \bar{\bar{S}}_{11}^{HH}(k_t^i, k_t^s) & \bar{\bar{S}}_{12}^{HH}(k_t^i, k_t^s) \\ \bar{\bar{S}}_{21}^{HV}(k_t^i, k_t^s) & \bar{\bar{S}}_{22}^{HV}(k_t^i, k_t^s) & \bar{\bar{S}}_{21}^{HH}(k_t^i, k_t^s) & \bar{\bar{S}}_{22}^{HH}(k_t^i, k_t^s) \end{pmatrix} \tag{3.10}$$

Similarly, for the slab containing the rough surface shown in in Fig. 3.2 (b), a reflectivity matrix is formed following the same procedure. However, only the input plane is of interest since we are only interested in the amount of reflected power from the rough surface for radar remote sensing applications. Again, a single element in the reflectivity matrix for a specific polarization state for a wave scattered in k_t^s due an incident wave with k_t^i direction is given by

$$R_{RS}^{pq}(k_t^s, k_t^s) = b_{RS}^p(k_t^s)/a_{RS}^p(k_t^i) \tag{3.11}$$

where a_{RS}^p and b_{RS}^q denote the spectral coefficients of a plane wave in the -z (inward) and +z (outward) directions respectively. The full reflectivity matrix can be filled by repeating the previous process for different incident angles and polarization and the general form should look as in Eq. (3.12)

$$\bar{\bar{R}}_{RS} = \begin{pmatrix} \bar{\bar{R}}_{RS}^{VV} & \bar{\bar{R}}_{RS}^{VH} \\ \bar{\bar{R}}_{RS}^{HV} & \bar{\bar{R}}_{RS}^{HH} \end{pmatrix} \tag{3.12}$$

After representing each snow slab with the corresponding scattering matrix and representing the rough surface with the reflectivity matrix, we are just left with only one remaining step, namely to cascade these layers together to calculate the bistatic scattering from the entire snow layer. The cascading algorithm is performed to get the backward scattered fields from the snowpack over the rough surface. A simple case of having only two snow slabs A and B over the rough surface is shown in Fig. 3.3.
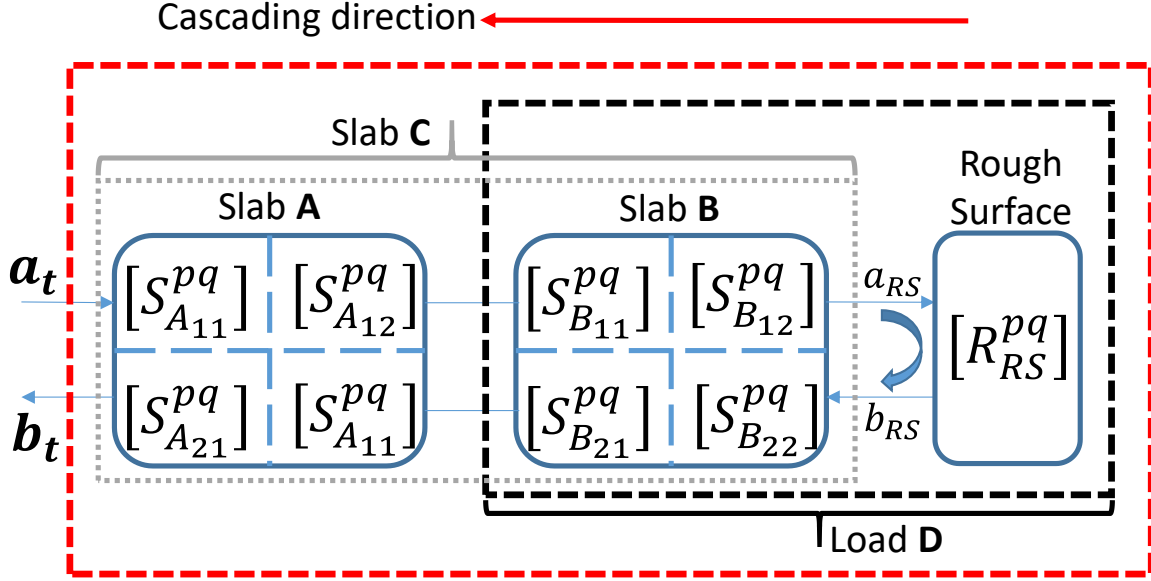
Figure 3.3 Cascading algorithm for multiple snow slabs over a rough surface.

In order to perform the cascading, we have two options: (1) to cascade Slabs A and B into Slab C and then cascade it with the reflectivity matrix, or (2) to cascade the reflectivity matrix of the rough surface with Slab B into a new load D, and then cascade load D with Slab A. To cascade the response of both slab A and B, each polarimetric component of the cascaded S-matrix S_c^{pq} is calculated in two steps as

$$S_c^{pq} = S_a^{pq} S_b^{qq} + S_a^{pp} S_b^{pq} \tag{3.13}$$

where $p, q = v \ or \ h$. For each of the previous two multiplications, the generalized n-port cascade connection is employed [71] through the following equations:

$$\bar{\bar{S}}_{11}^c = \bar{\bar{S}}_{11}^a + \bar{\bar{S}}_{12}^a \, \bar{\bar{S}}_{11}^b \big(\bar{\bar{I}} - \bar{\bar{S}}_{22}^a \bar{\bar{S}}_{11}^b\big)^{-1} \bar{\bar{S}}_{21}^a$$

$$\bar{\bar{S}}_{21}^c = \bar{\bar{S}}_{21}^b \big(\bar{\bar{I}} - \bar{\bar{S}}_{22}^a \bar{\bar{S}}_{11}^b\big)^{-1} \bar{\bar{S}}_{21}^a$$

$$\bar{\bar{S}}_{12}^c = \bar{\bar{S}}_{12}^a \bar{\bar{S}}_{12}^b + \bar{\bar{S}}_{12}^a \, \bar{\bar{S}}_{11}^b \big(\bar{\bar{I}} - \bar{\bar{S}}_{22}^a \bar{\bar{S}}_{11}^b\big)^{-1} \bar{\bar{S}}_{21}^a$$

$$\bar{\bar{S}}_{22}^c = \bar{\bar{S}}_{22}^b + \bar{\bar{S}}_{21}^b \, \big(\bar{\bar{I}} - \bar{\bar{S}}_{22}^a \bar{\bar{S}}_{11}^b\big)^{-1} \bar{\bar{S}}_{22}^a \bar{\bar{S}}_{21}^b$$

<div style="text-align:right">(3.14)</div>

where $\bar{\bar{I}}$ is the identity matrix. It is worth mentioning that the term between the brackets $\left(\bar{\bar{I}} - \bar{\bar{S}}_{22}^a \bar{\bar{S}}_{11}^b\right)^{-1}$ accounts basically for the multiple reflections between the two slabs. The cascading algorithm accounts for the multiple reflections between different slabs in a coherent manner. However, to cascade the reflectivity matrix with slab B to form a new load D (reflection), we can use a generalized form of the output from a signal flow graph as in [76]

$$\bar{\bar{R}}^D = \bar{\bar{S}}_{11}^b + \bar{\bar{S}}_{12}^b \, \bar{\bar{R}}_{RS} \left(\bar{\bar{I}} - \bar{\bar{S}}_{22}^b \bar{\bar{R}}_{RS}\right)^{-1} \bar{\bar{S}}_{21}^b \tag{3.15}$$

Again, the term $\left(\bar{\bar{I}} - \bar{\bar{S}}_{22}^b \bar{\bar{R}}_{RS}\right)^{-1}$ accounts for the multiple interactions between the snow layer and the rough surface. As shown from Eq. (3.13) and Eq. (3.14), it is more computationally demanding to cascade the snow slabs first and then include the rough surface response than to start by cascading the rough surface with the layer above it. Therefore, for an arbitrary number of snow slabs, it is preferable to start by loading the rough surface response into the slab above it and then loading the next slab above them, and so on.

Thus the SSWaP-SD acts as a domain discretization technique [90-92], wherein the complex medium is discretized into simpler domains that are linked together in a coherent way so as to precisely account for the interactions between them. The cascading algorithm accounts for all the multiple scattering effects between the different slabs, leaving us with only one more task to do, namely to obtain a fully coherent estimate of the single slab scattering matrix. This can be realized by solving Maxwell's equations numerically for the region inside the slab to obtain the single slab S- or the surface reflectivity matrix such that all multiple scattering contributions are included. The numerical solution for electromagnetic scattering from a single snow slab is discussed in chapter 4 and the rough surface reflectivity matrix computation is reported in chapter 5.

3.3. Conclusion

A fully-polarmetric fully-coherent time-efficient 3-D EM solver is presented through the SSWaP-SD technique. The method depends on decomposing the snowpack into thin slabs and representing each slab with an N-dimensional scattering matrix and representing the rough ground surface with a reflectivity matrix. Next, implementation of the cascading algorithm leads to the full response for the snowpack.

Chapter 4

Numerical Model for Electromagnetic Scattering from a Snow Layer of Arbitrary Thickness

4.1. Introduction

This chapter describes the full-wave solution developed in this investigation for characterizing the scattering within the volume of a snow layer of arbitrarily thickness, independently of the underlying ground surface. After dividing the snow layer into a finite number of horizontal slabs, we apply a numerical technique to solve for the scattering matrix of each slab. Then we cascade the scattering matrices together to obtain the full scattering response for the entire snow layer. By treating the snow as a statistically homogenous medium, Monte-Carlo simulations are performed for a single slab of snow to form the statistics of the building-block S-matrix, which then are used along with a Pseudo-random generator to simulate the statistics of the other snow slabs.

4.2. Single Slab Solution

Since the cascading algorithm accounts for the interactions between different slabs, the precise coherent estimation of the single slab S-matrix is of crucial importance to the overall accuracy of the SSWaP-SD method. To calculate the S-matrix, we needed to apply a numerical solution of Maxwell's equations, so we considered two possible methods. The first method uses a Finite-Element Method (FEM) commercial solver (namely, HFSS) and the other method relies

on writing a Method of Moment (MoM) code based on the DDA. For cross comparison, a snow slab with dimensions of $5\lambda \times 5\lambda \times \lambda/4$ ($\approx 100mm \times 100mm \times 5m$ at 14 GHz), was simulated using the two techniques. These dimensions correspond to the maximum dimensions that HFSS can handle in a reasonable amount of simulation time. Comparison of the two methods is presented in the following sections.

4.1.1 Finite Element Method Solution

In order to solve for the scattered fields using HFSS (FEM-based solver), we first have to draw the random medium into HFSS. Because HFSS can accommodate only a few standard shapes or objects such as a rectangular box, a sphere, a cylinder, and a few others, we generated a polyline-based importing algorithm to draw the random snow layer into HFSS through three steps. First, 2-
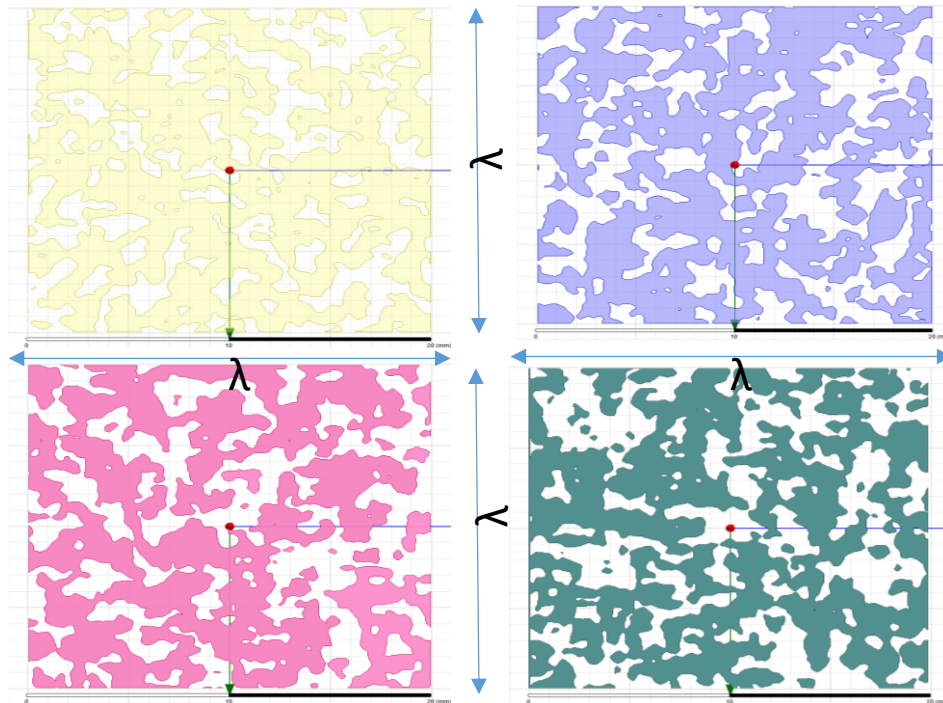
Figure 4.1 Samples of 2-D cuts of snow medium imported into HFSS using the polyline-based technique.

D horizontal cuts are selected from the 3-D sample, assuming that the medium remains statistically uniform between these cuts. The spacing between the adjacent cuts is selected to be the same as the vertical discretization of $\lambda/20$. Second, the border points of each snow grain inside this 2-D cut are sorted and a closed polyline that tracks these points is drawn using a visual basic script. Four samples of these 2-D cuts with dimensions of $\lambda \times \lambda$ (at 14 GHz) are imported into HFSS and are shown in Fig. 4.1. Each 2-D cut is plotted with different color in Fig. 4.1 for better visibility.

Finally, all the 2-D cuts are stacked vertically to form the 3D snow sample in HFSS. One realization of such a medium is shown in Fig. 4.2 with dimensions of $\lambda \times \lambda \times \frac{\lambda}{4}$. A detailed explanation on the polyline-based is discussed in Appendix 1. After drawing the medium into HFSS, an adaptive meshing algorithm is used to generate a finely-discretized version of the medium. It generates a tetrahedron-based version of the actual structure which gives a fairly
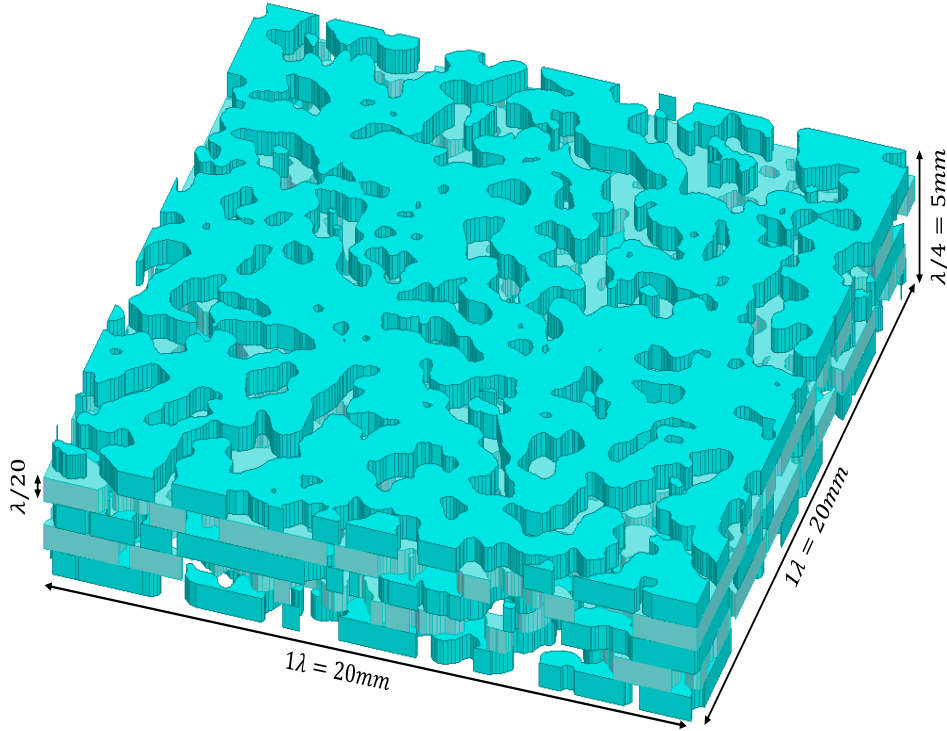
Figure 4.2 A sample of 3-D snow medium imported into HFSS with dimensions of $1\lambda \times 1\lambda \times \lambda/4$ at 14 GHz.
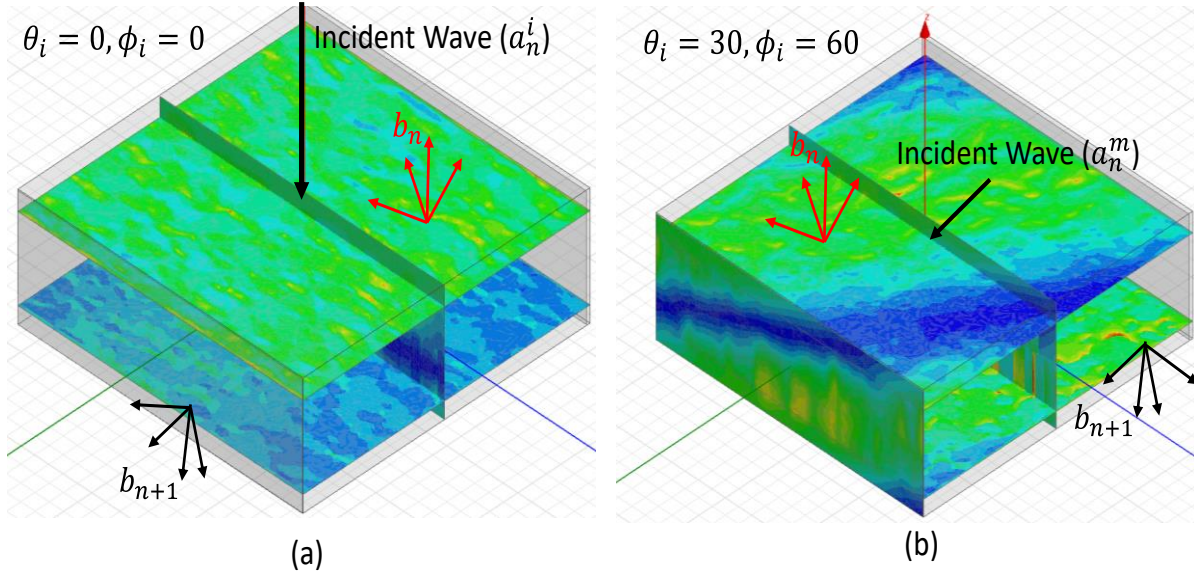
Figure 4.3 Example of calculated electric field at the input and output planes from HFSS for (a) $\theta_i = 0, \phi_i = 0$, and (b) $\theta_i = 30, \phi_i = 60$.

accurate discretization of the medium. Periodic boundary conditions are applied to imitate the infinite width of the snow layer and the structure is excited with plane waves by assigning Floquet ports at the top and bottom surfaces of the slab. Since Floquet ports are not allowed to touch a non-homogenous medium, we added a small air gab between the ports and the snow layer from both sides and we de-embedded the fields' calculations to the top and bottom layer of the snow slab at the end. An example of the fields calculated at the input and output plane of the snow slab is depicted in Fig. 4.3. Figure 4.3 (a) shows the electric field at the input (top) and output (bottom) layers for the normal-incidence case $(\theta_i = 0, \phi_i = 0)$. Figure 4.3 (b) shows an oblique incidence case with $\theta_i = 30, and\ \phi_i = 60$. After calculating the total field, we can compute the FFT and decompose the spatial fields into spectral components as discussed in Chapter 3. Therefore, we can easily find the power scattered in a certain direction k_s caused by an incident plane wave with propagation direction k_i.
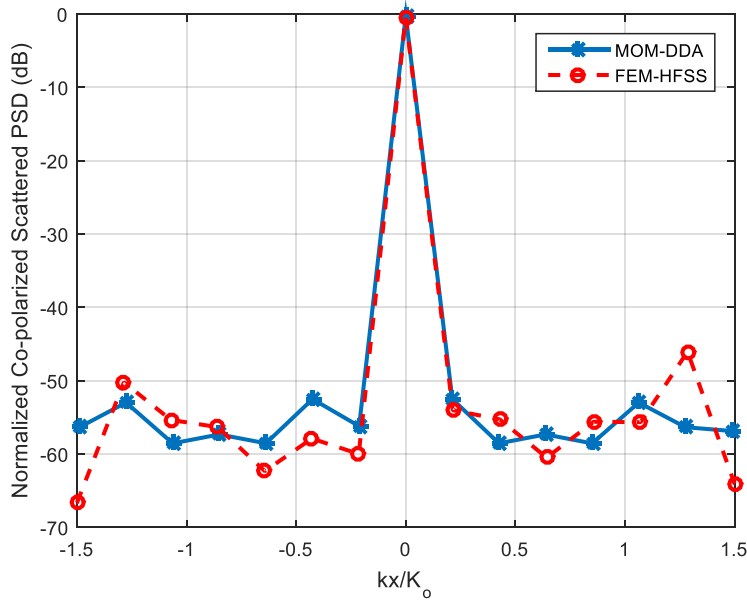
Figure 4.4 The average Co-polarized total power spectral density of the scattered field over 20 realizations using MOM-DDA and FEM-HFSS.

Monte-Carlo simulation is carried out to calculate the statistical characteristics of the scattered fields. It is common practice to represent the scattered field in a random medium as in Eq. (4.1)

$$E(r) = E_m(r) + E_f(r) \qquad (4.1)$$

where, $E_m = \langle E(r) \rangle$ is the main (coherent) field and $E_f(r)$ is the fluctuating (incoherent) component. For example, the average total (coherent + incoherent components) Power Spectral Density (PSD) of the backward propagating total field resulted is shown by the dashed red trace Fig. 4.4 for a normally- incident plane wave. In the K-space, the normal incidence direction is defined by $k_x = k_y = 0$. The PSD has a peak (-0.39 dB) at directions $k_x = k_y = 0$ which indicates that the maximum coherent scattered power is in the normal direction which happens to be the specular direction in this specific case. Such a result is as expected since the coherent contribution from a scatterer propagates mostly along the forward and specular directions. Another

important observation to note is that the power of the coherent component far exceeds the power levels of all the fluctuating (incoherent) components. One main factor responsible for why the power levels of the incoherent components are much lower than that of the coherent component is related to the fact that the slab is electromagnetically thin, which means that the slab does not contain enough scatterers to direct significant amount of the incident power to directions other than the coherent directions. Due to the huge difference between the coherent and incoherent components, we can expect that numerical noise can adversely affect the accuracy of our estimate of the S-matrix. In remote sensing, we usually are particularly interested in observing the statistics of the incoherent component, so we need to enlarge the dimensions of the individual slabs. The S-matrix of a single slab is formed by sweeping the excitation incidence angle and observing the scattered fields on the allowed points of the k-plane for each incidence angle. However, the simulation time for each angle in this case was around 7 hours and we need to repeat these calculations for many different angles, which renders the solution computationally expensive. Due to the long simulation time and the inevitable need to increase the slab dimensions, we aimed for another time-efficient numerical solution for the problem which is discussed in the coming section.

4.1.2 Method of Moments Solution

To address the shortcomings of the FEM-solver, we considered another numerical solver based on the solving the Volume Integral Equation (VIE) through the simplification of the Discrete Dipole Approximation (DDA). The DDA was initially introduced for computing the fields scattered from targets (media) with a complex nonhomogeneous dielectric constants [73], and was later applied to solve for scattering from thin snow layers [50]. The DDA depends on dividing the medium into electromagnetically small cubes. These cubes are then represented by dipoles whose

dipole moments are related through Green's function to form the matrix equation. Before, we dive into the implementation details of the DDA, we should mention that it suffers from the staircase approximation due to the cubic-based discretization which might result in lower solution accuracy when compared to the tetrahedron-based FEM solver. However, the matrix equation resulting from the DDA can be solved iteratively and the solution can be accelerated using the FFT, leading to much shorter simulation time. Following the same analysis outlined in [47] to derive the DDA equation, we can start from the wave equation for an inhomogeneous medium

$$\nabla \times \nabla \times \bar{E} - k^2 \bar{E} = k^2 (\epsilon_r(r) - 1)\bar{E} \tag{4.2}$$

Where k is the free space propagation constant and $\epsilon_r(r) = \epsilon_{ice} \approx 3.2$ if $r \in V_{ice}$ and $\epsilon_r(r) = 1$ elsewhere. The right hand side of the equation can be regarded as the polarization current that excites the wave equation. Hence, the scattered field is calculated using the application of the periodic dyadic Green's function over this polarization current, and since the total field is the sum of the incident and scattered fields, the scattered field can be determined by applying the Green's function to the polarization current in Eq. (4.2). Then, the total field at a point r is given by Eq. (4.3).

$$\bar{E}(r) = \bar{E}^i(r) + k^2 \int_V \bar{\bar{G}}_p(r,r')(\epsilon_r(r') - 1)\bar{E}(r')dr' \tag{4.3}$$

where $\bar{E}$ is the total field, $\bar{E}^i$ is the incident field, and $\bar{\bar{G}}_p(r,r')$ is the periodic Green's function. The second term in Eq. (4.3) represents the scattered field due to the polarization current of the ice inclusions inside the air background. This equation is the VIE that we need to solve. In order to numerically solve the VIE in Eq. (4.3), the domain is discretized into cubes with side length $d = \frac{\lambda}{32}$ and each cube is replaced by a dipole whose dipole moment is given by

$$\bar{p}_m = d^3 \epsilon_o (\epsilon_{r_m} - 1) \bar{E}_m \tag{4.4}$$

It is clear that only the ice occupied positions result in non-zero dipole moments. Therefore, we can rewrite a discretized form of the integral equation as

$$\bar{p}_m = \alpha_m \bar{E}_m^i + \alpha_m \frac{k^2}{\epsilon_o} \sum_{m=1, m \neq n}^{N_d} \bar{\bar{G}}_{p_{mn}} \cdot \bar{p}_n \tag{4.5}$$

Where p_m is the dipole moment of the mth dipole, $\bar{\bar{G}}_{p_{mn}} = \overline{\overline{G_p}}(r_m, r_n)$, N_d is the total number of dipoles, and α_m is the polarizability at the mth location which is given by [47] as

$$\alpha_m = d^3 \epsilon_o (\epsilon_{r_m} - 1) \left(\bar{\bar{I}} - k^2 (\epsilon_{r_m} - 1) \bar{\bar{S}} \right)^{-1} \tag{4.6}$$

in which $\bar{\bar{S}}$ is the singular integral of the Green's function and is given by $\bar{\bar{S}} = \int_{V_0} \bar{\bar{G}}_p(r, r') dr'$, where r, r' at point locations in V_0. The periodic Green's function is used to implement the assumption that the snow is periodic along the lateral directions. It is important to mention here that the width of the slab (W) dictates the number of propagating Floquet modes. By exploiting the translational invariant properties of the Green's function, we end up with a MoM matrix in a Toeplitz form. Therefore, the Conjugate-Gradient (CG) iterative method can be used to solve the system of equations much faster than the direct solver. An FFT-based algorithm can be used in the matrix-vector multiplication inside the CG to speed it up significantly [74]. After solving the matrix equation, dipole moments are calculated. An example of the calculated dipole moments are given in Fig. 4.5 in an XY cut.
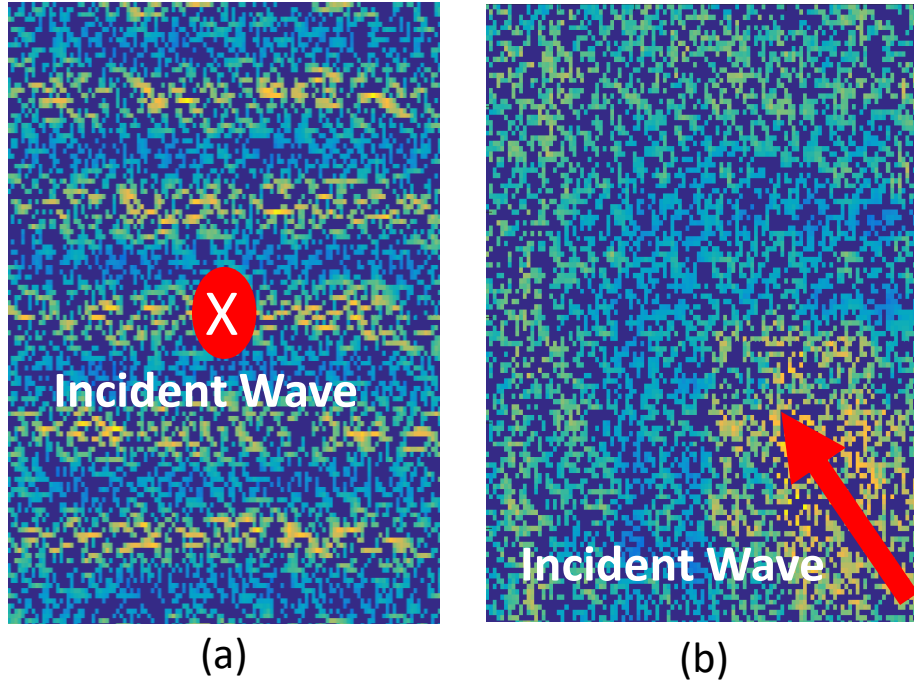
Figure 4.5 The calculated dipole moments for (a) $\theta_i = 0$, and (b) $\theta_i = 45$ degrees incidence angle at 9.5 GHz.

In Fig. 4.5(a), we show the magnitude of dipole moments for normal incidence case ($\theta_i = 0$), and in Fig 4.5(b) we show the dipole moments for $\theta_i = 45$ degrees. Then, the total field in the upper and lower planes are estimated and decomposed into plane waves. An example of the PSD of the total field is shown as the solid blue curve in Fig. 4.4 for a normally incident plane wave. As mentioned previously, the average PSD peaks ($\approx$-0.01 dB) along $k_x = 0$, so only a k_x cut is shown for simplicity.

   To further validate the implementation of our MoM code, we replaced the periodic Green's function with the 3-D free-space Green's function and used our code to calculate the scattering from a dielectric sphere with ka=4.5 and dielectric constant $\epsilon_c = 1.7866 - j0.266$ and compared the MoM-DDA code results with the analytical Mie series [93]. The comparison is shown in Fig.
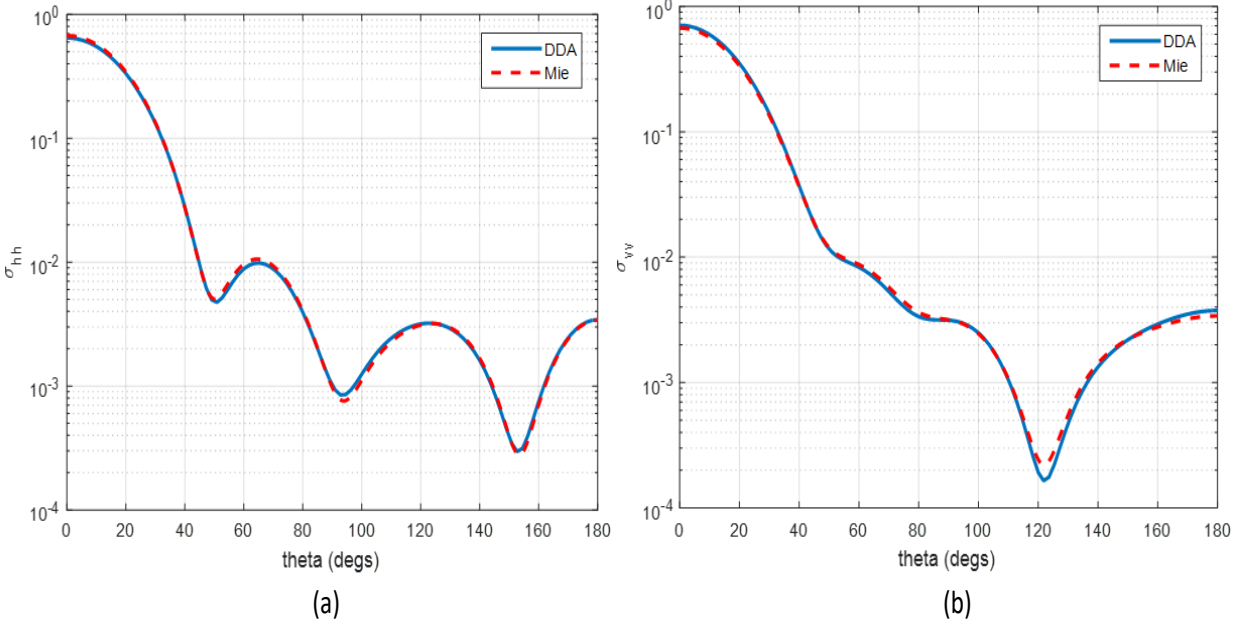
Figure 4.6 Validation of our MoM-DDA code against the Mie series solution for a sphere with ka=4.5.

4.6. Figure 4.6 (a) shows the MoM-DDA HH component (solid blue) compared with the Mie series solution (dashed red). Similarly, Fig. 4.6 (b) shows the comparison for VV components. Both plots show good agreement with the analytical solutions.

4.1.3 Comparison between MoM-DDA and FEM-HFSS Solutions

Figure 4.3 shows good agreement for the coherent power when computed using the FEM-HFSS and MoM-DDA techniques. Also, the results show almost a flat PSD in all directions except for the coherent direction. These results are as expected because the particle sizes are small relative to the wavelength. Along other directions (given by $k_x \neq 0$), however, large differences are observed between the power components of the total field. This is attributed to both the incident field contribution and the electromagnetically-small thickness of the simulated layer which does not include a sufficient concentration of random particles to generate a significant amount of

Table 4-1 Comparison between FEM-HFSS and MOM-DDA for the same slab dimensions

Method	Mesh Type	Number of unknowns	Simulation Time
FEM-HFSS	Tetrahedron-based	≈ 2,400,000	7 hours
MoM-DDA	Cubic-based	≈ 200,000	5 mins

incoherent scattered power. This leads to high vulnerability of the results to numerical noise, especially in directions where $k_x \neq 0$, and is the reason why there is a discrepancy between the MoM-DDA and the FEM-HFSS results.

Comparison between the two techniques in terms of the required number of unknowns and simulation time is summarized in Table I. The number of unknowns depends mainly on the discretization algorithm used in the solution domain. The MoM-DDA discretizes the medium into cubic cells, while the FEM-HFSS uses an adaptive tetrahedron-based meshing algorithm. To assure a fair comparison, the snow layer dimensions are chosen to be the same for both methods. Although the solution domain is the same, the two techniques have a different number of unknowns due to the different meshing algorithms. More specifically, one cube can be discretized into up to 12 tetrahedrons. Therefore, the simulation time for FEM-HFSS is much longer than for MoM-DDA, but the adaptive meshing algorithm provides a better structural representation for the real snow medium.

4.3. Arbitrarily-thick Snow Layer Response

With the confidence gained from our code results realized by comparing the MoM-DDA solution to the solution using the FEM-based commercial solver (HFSS) [72], we increased the snow layer dimensions to be ($16\lambda \times 16\lambda \times 1\lambda$ ($\approx 35cm \times 35cm \times 2cm$ at 14 GHz) and simulated several samples with snow parameters summarized in Table 4-2.
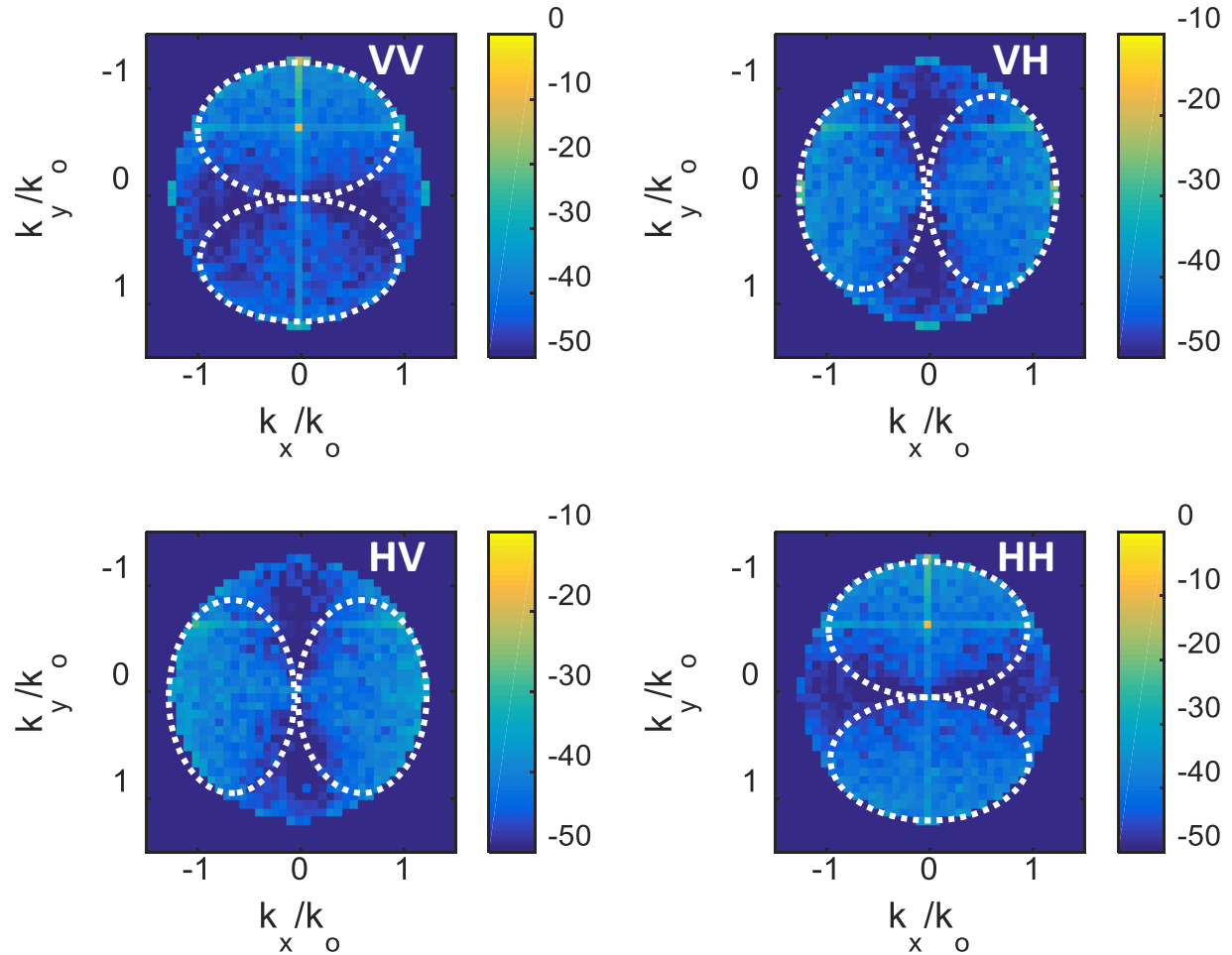
Figure 4.7 The average incoherent Co-polarized bistatic scattering coefficients over 50 realizations using MOM-DDA with an incidence angle of 40°.

Table 4-2 Snow medium parameters used in section 4.3

Parameter	Grain Size	Snow Density	Snow Depth
Value	$0.5\ mm$	$0.48\ g/cm^3$	$2\ cm$

As an example, the average (over 50 realizations) bistatic scattering in the backward direction in shown in Fig. 4.7 for an incidence angle of 40° ($k_{xi} = 0, k_{yi} = 0.6k_o$). As shown in the figure, there is a peak reflection along the specular direction which is indicated by the same

transverse direction and the flipped normal direction ($k_{xs} = k_{xi} = 0, k_{ys} = k_{yi} = 0.6k_o, k_{zs} = -k_{zi}$). The figure shows only the propagating modes, and all the evanescent modes were masked out. It is also important to mention that there is a peak reflection in the backscattered direction which is defined as ($k_{xs} = -k_{xi} = 0, \ k_{ys} = -k_{yi} = -0.6k_o, k_{zs} = -k_{zi}$). This peak reflection at the backscattering direction is due to the backscattering enhancement phenomenon. Interestingly, the bistatic scattered power distribution looks like a figure of 8 when observing the co-pol components (VV, and HH) as depicted by the dashed white shapes in Fig. 4.7. Most of the scattered power occurs along spectral directions that are inside the two white dashed ellipses. For the cross-pol components, the two ellipses are rotated by 90 degrees. These results are in agreement with the patterns reported in [47].

After repeating the same simulation for different incident angles at both polarizations, the full polarimetric S-matrix is formed. Then, different snow realizations are simulated to generate the statistics for each element in the S-matrix. Next, a pseudo random generator is used to create other samples for the corresponding S-matrices emulating the entire snowpack.

4.4. Validation against Measured Data

Using the previously described coherent cascading algorithm, we can calculate the statistics of the forward and backward scattered fields for any arbitrary thickness in a fully coherent way. After simulating 50 realizations of snow samples, we calculated the statistics of each element in the scattering matrix and then used them to generate the base information needed for a pseudo-random generator, so as to create other samples of the snow slabs without repeating the computationally-demanding simulations. The approach is justified because the snow medium is assumed to be statistically homogeneous. The accuracy of our computational model is validated
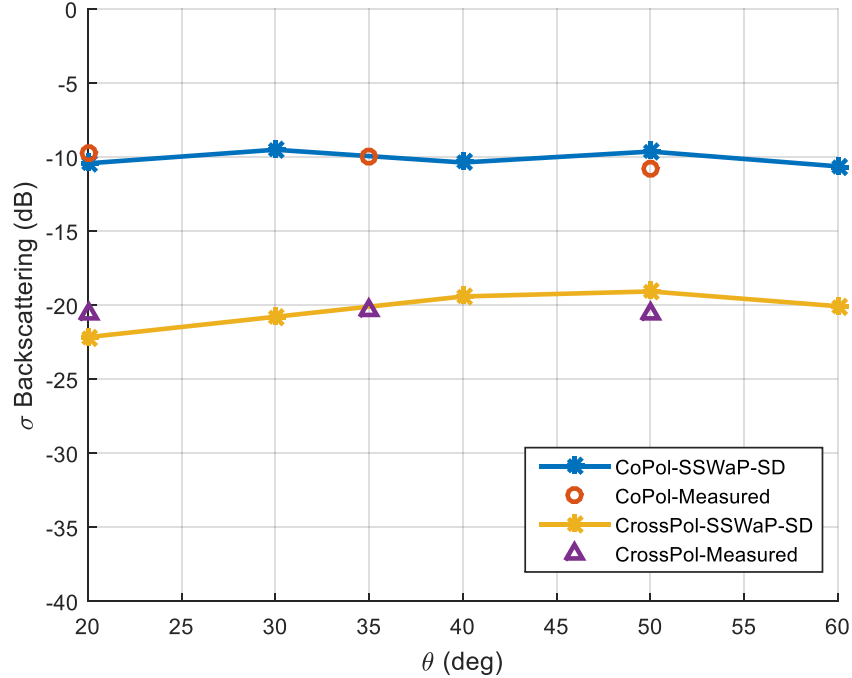
Figure 4.8 Backscattering coefficient versus angle at 15.5 GHz and the volume fraction (ϕ_v=50%) and snow depth of 90 cm.

using measured data [79, 80]. The measurement set in [79] was part of the NASA CLPX campaign. The campaign was held in Boulder, Colorado, USA, in February, 2003 over a period of several weeks. The measurements were performed using a Ku-band radar (15.5 GHz) at three different incidence angles, namely 20, 35, and 50 degrees. The reported ground truth data listed the snow depth as 90 cm over the entire measurement period. Figure 4.8 compares our model expectation (solid) to the measured data (dotted) for the Co- and Cross- Polarized backscattering coefficients for volume fraction $\phi_v = 50\%$ at 15.5 GHz and snow depth of 90 cm.

Even though Fig. 4.8 shows good agreement with the measured data, it is compared with only a single value of snow depth. Our model is then compared with measured data reported in [80], where an artificially generated snow medium was used. The use of artificial snow enables an easy change of the snow depth. Four different snow thicknesses were used as follow: 5, 20, 60,
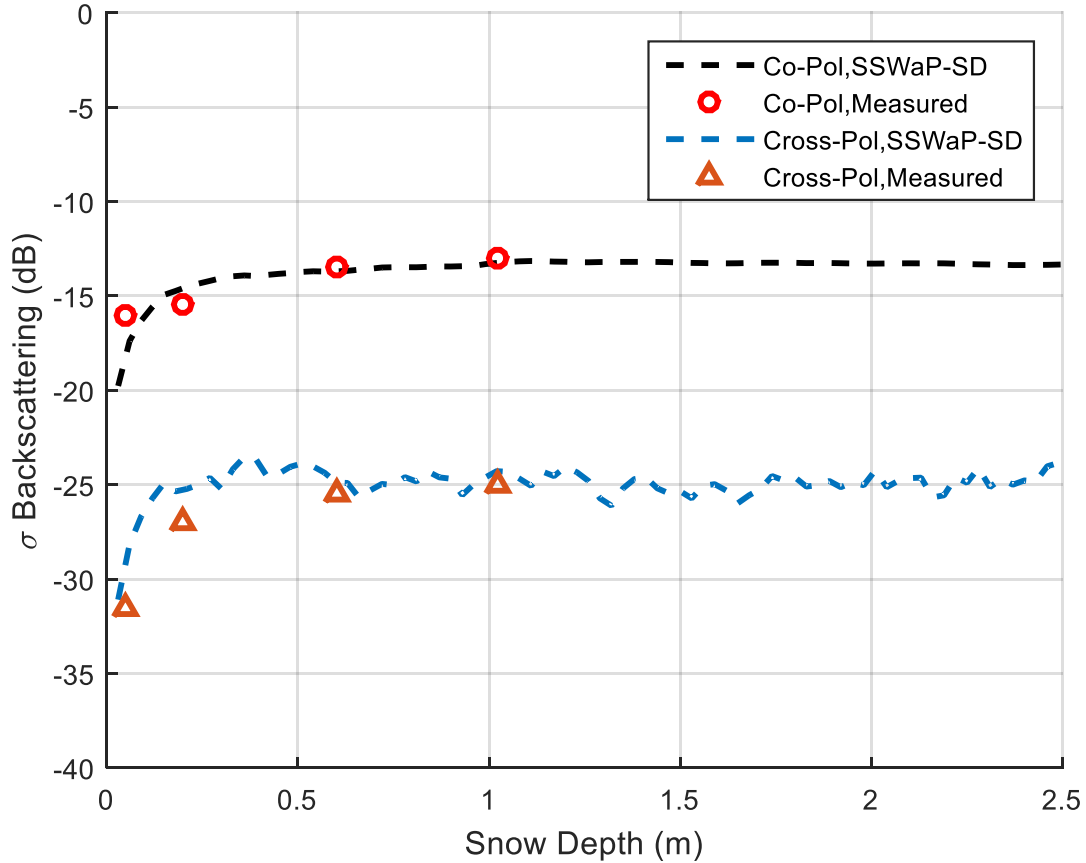
Figure 4.9 Backscattered cross-section versus snow depth, the incident angle was chosen to be 40° at 9.5 GHz.

and 102 cm. Figure 4.9 shows very good comparison between our computational model and the measured data. It is important to mention that the model response is in a better agreement for higher thicknesses of the snow layer. The rough surface underneath the snow layer contributes a non-negligible amount of scattered power for shallow snow layers. Moreover, the results show that the backscattering coefficient saturates after reaching a certain snow depth, which is found to be around 40 cm in the case of this example.

Building on the confidence gained from our computational model, we changed the volume fraction and observed the forward and backward scattering response at 14 GHz, and the results are displayed in Figs. 4.10 and 4.11. Figure 4.10 shows how the forward scattering power decreases
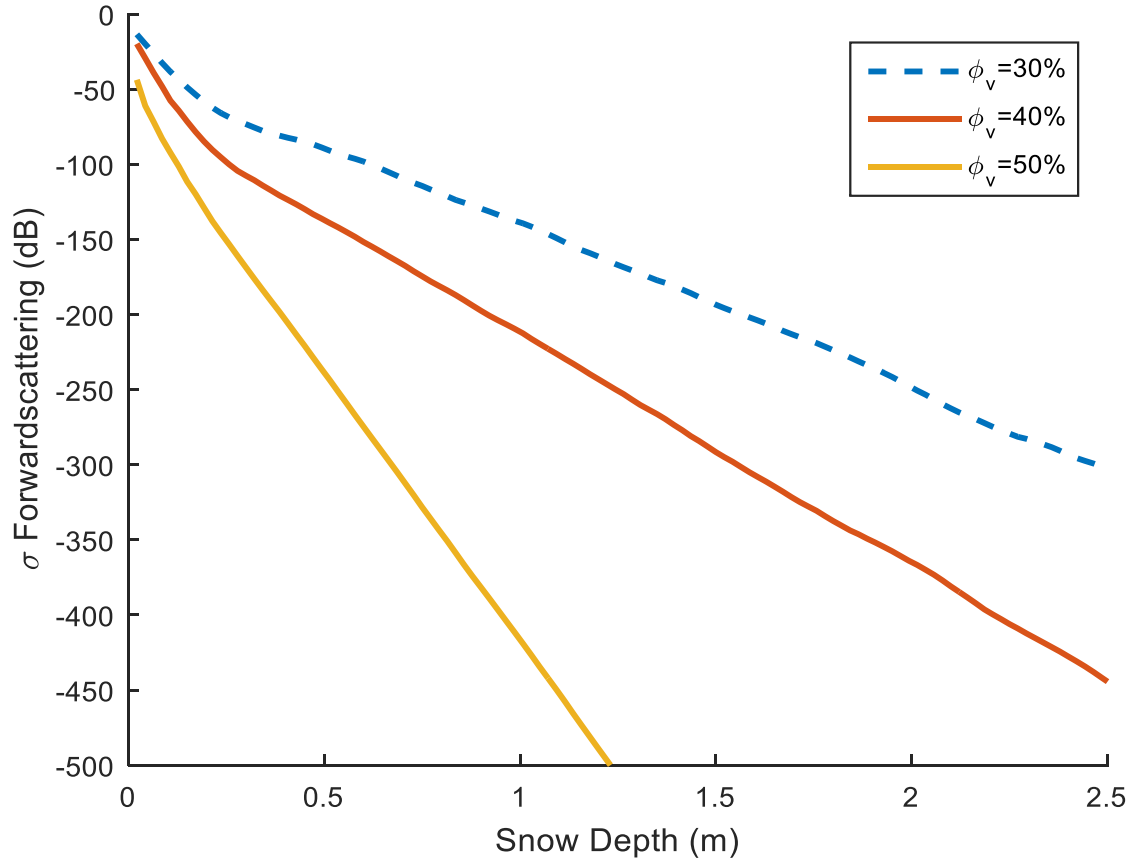
Figure 4.10 Co-Polarized Forward scattering cross-section versus snow depth for different volume fractions at 14 GHz, the incident angle was chosen to be 40°.

with increasing snow depth. Since the snow is a dense random medium, it scatters the incident power in all directions, including the forward direction. However, the forward scattering power attenuates rapidly inside the snow medium because it gets scattered along many different directions. The forward scattered power in Fig. 4.10 is directly proportional to the attenuation coefficient of the snow medium. We observe a dual-slope behavior in the forward scattering direction which indicates that the attenuation through the medium is dominated mainly by the incoherent component. This point is known as "Knee-point" and it appears to occur when the snow depth reaches approximately 40 cm. The dual-slope behavior is also observed for the backscattering response, which is expected due to the fact that most of the backscattered power is contributed by
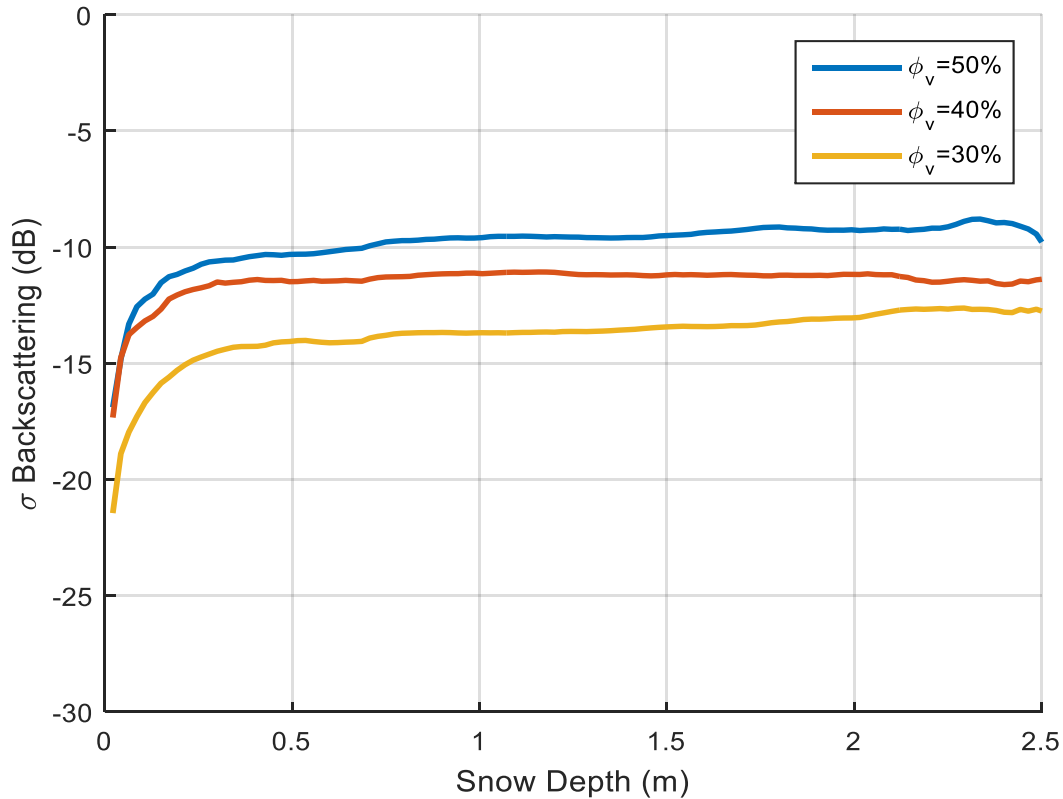
Figure 4.11 Co-Polarized Back-scattering cross-section versus snow depth for different volume fractions at 14 GHz, the incident angle was chosen to be 40°.

the top layers, and the contributions from the lower layers become insignificantly small after exceeding a certain thickness of the random medium. As expected, the higher the volume fraction, the greater is the attenuation in the forward direction and the knee-point occurs at shallower snow depths. Figure 4.11 shows that the higher is the volume fraction, the higher is the saturation level of the backscattering coefficient. Basically, greater volume fraction corresponds to a larger number of scatterers per unit volume, which results in a stronger backscatter response.

To observe the role of the operating frequency, we swept the frequency from 8 GHz to 17 GHz, which encompasses both X and Ku bands. The backscattering response versus frequency is shown in Fig. 4.12 for a 40-cm thick snow layer observed at an incidence angle of 40 degrees. As observed, increasing the frequency increases the magnitude of the backscattering coefficient for
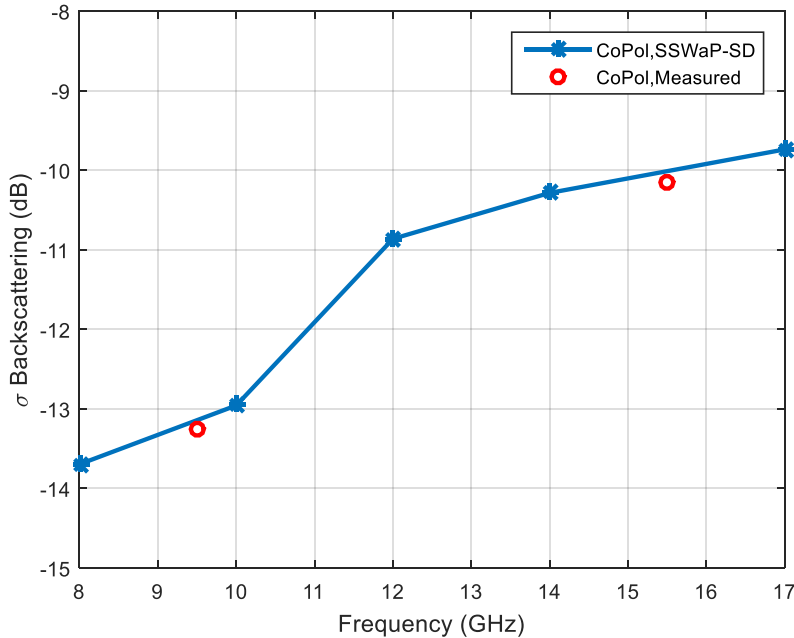
Figure 4.12 Backscattering coefficient versus frequency for 50% volume fraction, 40 degrees incidence angle and 50 cm snow depth.

the same snow depth. This is attributed to the increase in the snow particle size relative to the operating wavelength.

4.5. Conclusion

A Single slab of snow is solved numerically using the Method of Moments under the Discrete Dipole approximation and compared with a Finite Element Solver. After the MoM-DDA code is validated, it is used to build the statistics of the scattering matrix of a single snow slab that is then used as the building block to emulate the equivalent S-matrix of different slabs within the snow medium. The full response is calculated using the SSWaP-SD described earlier along with the results obtained from the single slab solution. This way, a fully-coherent time-efficient method is implemented to solve for the total forward and backward scattered fields from a snow layer of

arbitrary thickness. The model is validated against two different measurement campaigns and show very good agreement.

Chapter 5

Computation of Reflectivity Matrix for a Rough Ground Surface

5.1. Introduction

As was noted in the previous chapter, the scattering contribution of the ground surface to the total scattering is non-negligible for shallow snow layers. In order to obtain the complete scattering response of the snowpack, the EM scattering by the underlying surface has to be taken into account. Fundamentally, there are two approaches available to formulate the reflectivity matrix representing the rough ground surface, namely through an analytical solution or the implementation of a numerical technique. The analytical solution is based on Physical Optics (PO) and the numerical solution is based on MoM-software.

5.2. Analytical Solution

Traditionally, the scattered field from a rough surface is computed using the Physical Optics (PO) technique   under the tangent-plane approximation. The local surface fields are approximated from those of an infinite plane tangent to the surface at the local point. This is a good approximation when the radii of curvature at every point on the surface are large compared to the wavelength and the surface rms slope is small, wherein not much shadowing occurs and therefore multiple surface scattering is insignificant. In the PO approximation, both the coherent and incoherent powers can be calculated for a specified correlation profile. Generally speaking,

for a rough surface with a height profile $z = f(x, y)$, the local normal to the surface at point (x, y) is defined as follow:

$$\hat{n} = \frac{\nabla(z - f(x,y))}{|\nabla(z - f(x,y))|} = \frac{-f_x\hat{x} - f_y\hat{y} + \hat{z}}{\sqrt{1 + f_x^2 + f_y^2}} \tag{5.1}$$

where f_x, f_y are the partial derivatives with respect to x and y, respectively. It is also important to note that the tangent to the surface can be written as

$$\hat{t} = \frac{\hat{k}_i \times \hat{n}}{|\hat{k}_i \times \hat{n}|} \tag{5.2}$$

Following the derivation in [49] and using the Ewald-Oseen extinction theorem and some algebraic manipulation, we can reach the following expression for the field of the wave scattered along direction $\hat{k}_s$ when excited by a plane wave travelling along direction $\hat{k}_i$

$$\overline{E}_s(\bar{r}) = \frac{ik_0 e^{ik_0 r}}{4\pi r}(\bar{\bar{I}} - \hat{k}_s\hat{k}_s) \cdot \iint\limits_S \bar{C}(f_x, f_y)\, e^{ik_o(\hat{k}_i - \hat{k}_s)\cdot\bar{r}'} dr' \tag{5.3}$$

where $\overline{E}_s(\bar{r})$ is the scattered field at a general point $\bar{r}$, k_0 is the free space wave number, and $\bar{C}(f_x, f_y)$ is given by

$$\bar{C}(f_x, f_y) = \sqrt{1 + f_x^2 + f_y^2}(E_o \cdot \hat{t})\left\{ \begin{array}{l} -[(\hat{n}\cdot\widehat{k_i})(1 - R_e) + (\hat{n}\cdot\hat{k}_s)(1 - R_e)]\,\hat{t} \\ +(1 + R_h)\,(\hat{n}\times\hat{t}) + (\hat{n}\cdot\hat{k}_i)(1 - R_h)\,(\hat{k}_s\times\hat{t}) \end{array} \right\} \tag{5.4}$$

where E_o is the amplitude of the incident plane wave, and R_e, R_h are the perpendicular and parallel Fresnel reflection coefficients, respectively. It is important to mention that the integral in Eq. (5.4) is often difficult to evaluate due to the complicated argument $\bar{C}(f_x, f_y)$ and the random phase term associated with it. Under the approximation of a gentle surface roughness, the coefficient $\bar{C}(f_x, f_y)$ can be approximated by $\bar{C}(0,0)$, in which case we are left with the integration of the phase term I

$$I^0 = \iint_S e^{ik_o(\hat{k}_i - \hat{k}_s) \cdot \vec{r}'} \, dx' dy' \tag{5.5}$$

Since the integrand is random, the value of I^0 is random as well. Therefore, we can calculate the mean power $(|\langle I^0 \rangle|^2)$ and subtract it from the average total power $(\langle |I^0|^2 \rangle)$ to obtain the incoherent component. With appropriate change of variables and using the stationary phase approximation, we can express the incoherent component of I^0 as follows:

$$\langle |I^0|^2 \rangle - |\langle I^0 \rangle|^2 = 2\pi A \int_0^\infty \rho J_o(v_p \rho) \left[e^{-\sigma^2(1 - C_r(\rho))v_z^2} - e^{-\sigma^2 v_z^2} \right] d\rho \tag{5.6}$$

where A is the surface area, $\vec{v} = v_\rho \hat{\rho} + v_z \hat{z} = k_0(\hat{k}_i - \hat{k}_s)$, J_o is the zeroth order Bessel function, σ is the rms height of the surface, and $C_r(\rho)$ is the surface correction function. For a specific roughness profile, we can calculate the total incoherent bistatic scattering coefficient from Eq. (5.4) by plugging the results from Eq. (5.6). The general form is given be

$$\sigma_{pq}^0(\theta_s, \phi_s; \, \theta_i, \phi_i) = \frac{|k_o|^2}{4\pi A} |\hat{p}_s \cdot \bar{C}^q| \left[\langle |I^0|^2 \rangle - |\langle I^0 \rangle|^2 \right] \tag{5.7}$$

where $p, q = V \text{ or } H$ for the vertical and horizontal polarizations, respectively. We also should note that the solution given by Eq. (5.7) gives the average incoherent power only, not the fields, and additionally it is valid only in the far field region. An example of the computed co-pol bistatic scattering coefficient based on Eq. (5.7) is shown in Fig. 5.1 for a surface with rms height and correlation length of 0.35 cm and 2.09 cm, respectively, at incident angle $\theta_i = 40 \text{ and } \phi_i = 0$ and for a dielectric constant of 4.6 at 9.5GHz. It is observed that there are some directions along which no scattering occurs, which is due to terms in Eq. (5.7) which vanish when $\phi_s - \phi_i = \pm 90°$. The main drawback to use the formulation given by Eq. (5.7) is that it neglects phase information because deal with power instead of fields. However, this issue can be mitigated if we were to solve the integration in Eq. (5.4) without applying the stationary phase approximation.
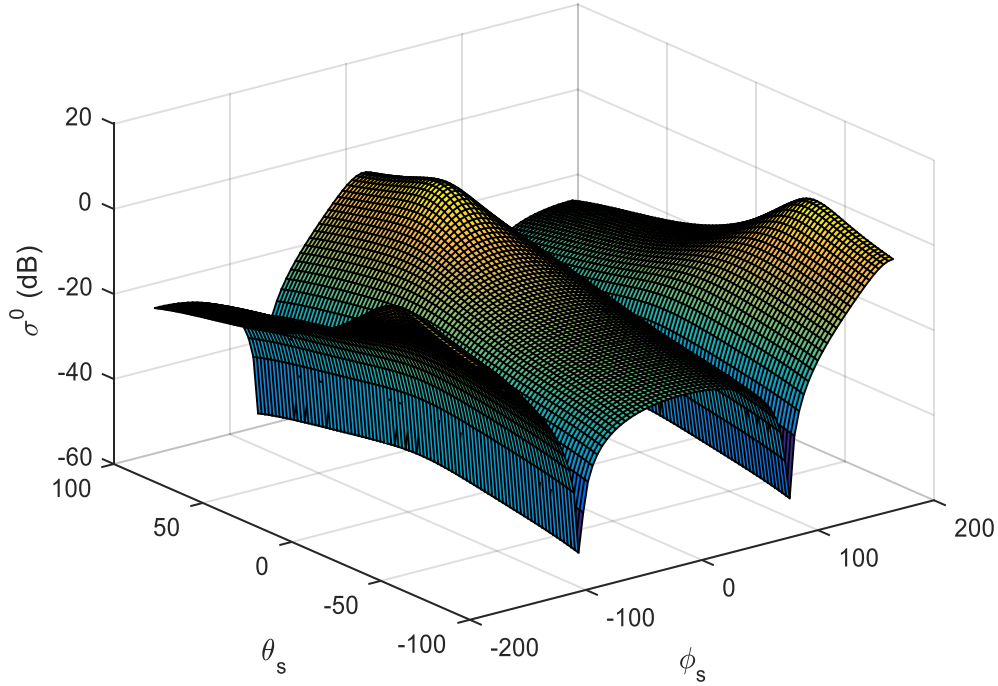
Figure 5.1 Bistatic scattering from a rough surface using the PO method. The surface has an rms height of 0.35 cm, correlation length of 2.09 cm, dielectric constant of 4.6, for an incidence angle of $(\theta_i = 40, \phi_i = 0)$ and operating frequency of 9.5GHz.

Solving the integral in Eq. (5.4) can provide the scattered field directly. We note that at each point r' on the rough surface, there is a random phase term associated with a complicated argument that changes accordingly. In order to evaluate the integral in Eq. (5.4), we first have to create a triangle-based mesh for the rough surface where we aim to evaluate the argument $\bar{C}(f_x, f_y)$ and consequently the whole integrand. Given a point $r'(x', y', z')$, we can easily find the local normal to the surface and the tangent by applying Eq. (5.1) and Eq. (5.2). The Fresnel reflection coefficient is then applied to these local points to calculate R_e and R_h. Therefore, for a specific

direction of observation k_s , we can calculate the polarimetric components of the argument $\bar{C}(f_x, f_y)$, which leads to the following form for the integral

$$I_{PO} = \iint\limits_{S} \left(C^V(r')\hat{v} + C^H(r')\hat{h} \right) e^{ik_o(\hat{k}_i - \hat{k}_s).\bar{r}'} \, dx' dy' \tag{5.8}$$

Each of the previous two components can then be solved numerically. To solve the integral numerically over the triangle, we have to perform the simplex to get the equivalent right-handed triangle in the transformed co-ordinates (α, β, γ). Next, we use the Gauss-quadrature method to evaluate the integral. The Gauss-quadrature method computes the integral by approximating it as a sum of weighted arguments calculated at the zeros of a Legendre-polynomial. For example, the polarimetric component of Eq. (5.8) can be expressed as

$$I_{PO}^p = \iint\limits_{S_\Delta} \left(C^V(r') \right) e^{ik_o(\hat{k}_i - \hat{k}_s).\bar{r}'} \, dr' = \iint\limits_{S_\Delta} f_1(r') dr' \approx A_{S_\Delta} \sum_{i=1}^{N} w(\alpha_i, \beta_i) f_1(\alpha_i, \beta_i) \tag{5.9}$$

We used a 7-point Gauss-quadrature for each triangle, together with the parameters listed in [77]. After evaluating the integral on a small triangle, we repeat the process for all the triangular elements in the mesh to estimate the integral over the entire rough surface area. Then we can calculate the scattered field from the rough surface in any desired direction (k_s), which forms the reflectivity matrix as described before. It is also important to note that we then normalized the scattered field by dividing it by the square of the area of the rough surface, so as to compare it later to the backscattered coefficients resulting from other techniques.

5.3. Numerical Solution

For surface roughness conditions for which the PO approximation is not applicable, a full-wave numerical solution must be used instead. To solve for the scattering by the rough surface

numerically, we utilize a MoM-based commercial software (CADFEKO) using the simulation setup depicted in Fig. 5.2.

(a)

(b)

(c)
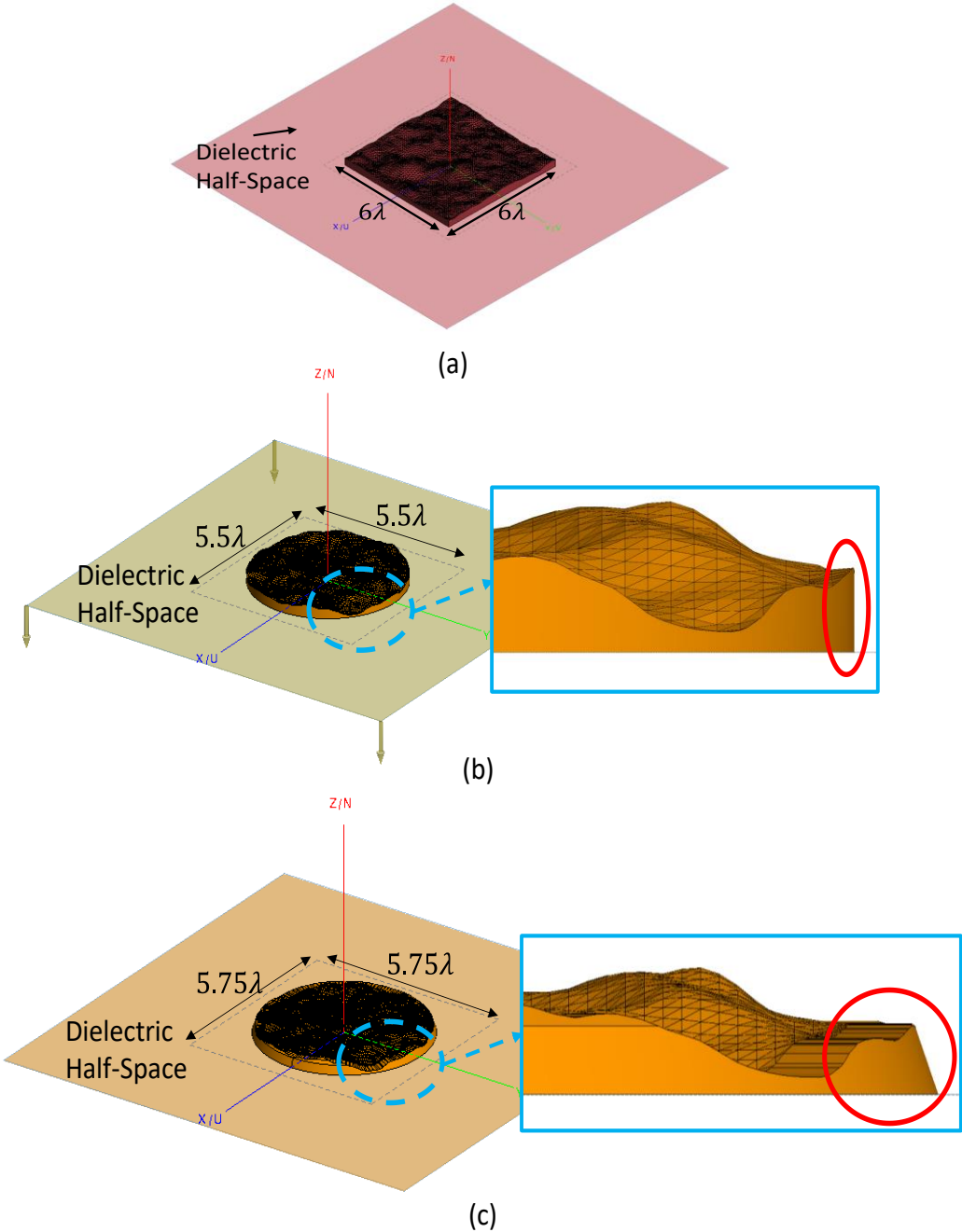
Figure 5.2 Simulation setup for rough surface scattering in CADFEKO using (a) square, (b) circular samples, and (c) circular sample with tapered edges.

CADFEKO is a MoM-based software that is widely used in antenna design. However, it offers the ability to choose between different types of Green's functions the free-space Green's function, a Green's function suited for a half-space dielectric medium, and the periodic Green's function. To perform the EM full-wave simulation using CADFEKO, we generate the rough surface profile using MATLAB, then we write an STL (Standard Triangle Language) file that includes the triangles representing the rough surface. The STL of the rough surface is then imported into the software and a half-space region is defined underneath it to emulate the infinite extent of the medium. The surface is then excited with set of plane waves and the far-field bistatic scattering is calculated accordingly for each of the plane waves to fill out a column in the S-matrix representing the rough surface response. This approach is reported by [94]. Monte Carlo simulations are performed to get the statistics of the S-matrix by repeating the calculations for 75-100 realizations of the rough surface with the same statistics. It is worth mentioning that when such a technique is used, the accuracy of its results may get degraded by edge diffraction effects. In order to minimize the edge effects, we change the sample size and cross-section geometry for each realization to reduce the coherent addition of the artificial scattering components resulting from the edge diffraction. Figure 5.2(a) shows a square sample with $6 \lambda \times 6 \lambda$, Fig. 5.2(b) shows a circular sample with 5.5λ diameter, and Fig. 5.2(c) shows a circular sample with 5.75λ diameter with tapered edges as well.

In order to show the effectiveness of tapering the edges on suppressing the edge effects, we changed the rough surface parameters and repeated the simulations for multiple realizations. This step is important as well in the retrieval algorithms for the underlying soil layer, especially for shallow snow layers. For an inversion algorithm, the forward model must be run many times by varying the snow parameters as well as the rough surface parameters such as the rms surface
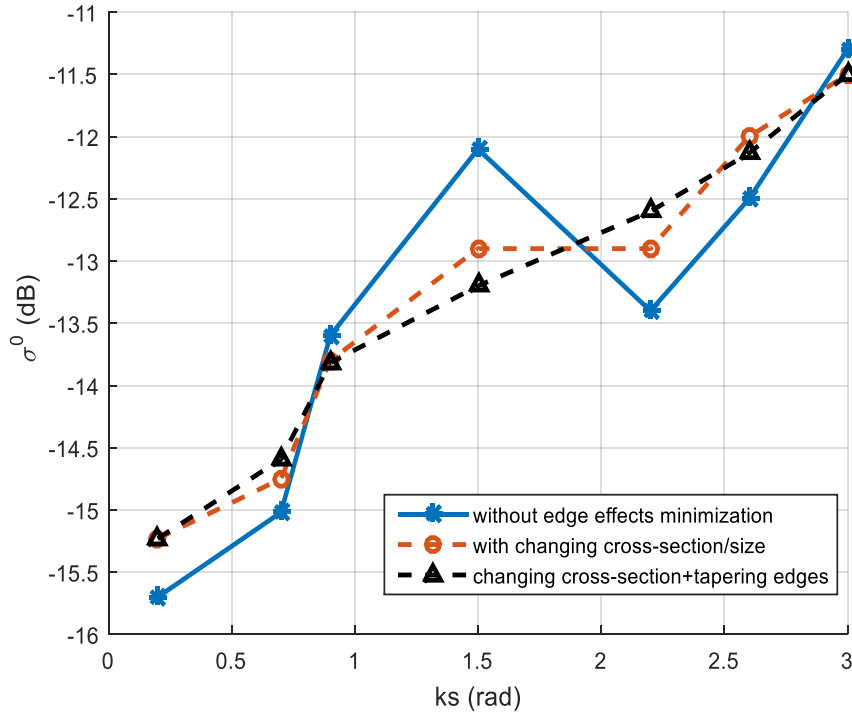
Figure 5.3 Normalized backscattering coefficient from rough surface for different rms heights with incidence angle of 40 degrees.

height and correlation length. The computed backscattering coefficient is shown in Fig. 5.3 as a function of ks where $k = \frac{2\pi}{\lambda}$ and the wavelength is around 3.16 cm at 9.5 GHz for a rough surface with correlation length of 2.09 cm and a dielectric constant of $\epsilon_{gnd} = 4.6 - j0.1$. The incidence angle is 40 degrees. In order to show the role of minimizing the edge effects on the computed scattering coefficient, we computed the scattering by treating all realizations of the rough surface as squares with dimensions of $6\lambda \times 6\lambda$. The results are shown by the blue trace in Fig. 5.3. As we can see, the response exhibits large nonphysical fluctuations. However, after employing the edge-effect minimization technique described earlier, we obtain the relatively smooth responses shown in red and black traces. In Fig. 5.3, the dashed black curve is the result of changing the cross-section from squares to circular in some of the realizations (Fig. 5.2(b)) and varying the size of

71

each sample a little bit (diameter of the sample varies between 5.5 λ to 6.25 λ). If, in addition, we incorporate tapered edges on top of that, we minimize the edge effect to the maximum extent, resulting in the dashed red curve.

5.4. Validation of Results

To validate the accuracy of our simulation techniques, the analytical and numerical techniques are compared in Fig. 5.4 against the Improved Integral equation Method (I2M) model and against measured data. The I2EM model is an integral equation-based model that takes shadowing effects into account through the application of a shadowing function. The measurement campaign reported in [79] was held in Brighton, Michigan, USA during March 1995. The results show good agreement between all four methods within a margin of few dBs. It is clear that applying the PO approximation by using (5.4) is more accurate than the analytical PO solution. It is also interesting to see that estimating the PO using (5.4) gives results that are more similar to those obtained using the integral equation based solvers (both I2EM and FEKO). Due to the complexity of the computational methods, we had to limit the extent of the surfaces for FEKO simulation to $6\,\lambda \times 6\,\lambda$. However, these dimensions can be increased significantly for numerical PO solutions.
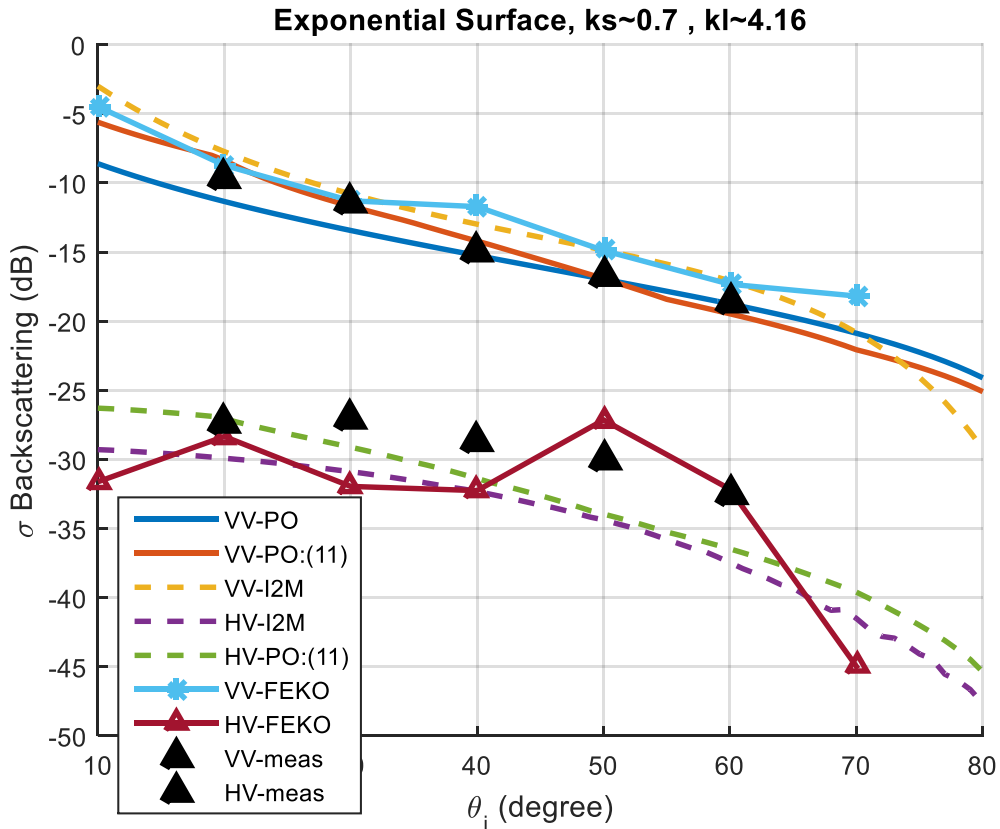
Figure 5.4 Cross-Comparison of backscattering coefficient of exponential rough surface between PO, I2M, FEKO, and measured data.

After obtaining the numerical solution for the field scattered by the rough surface, we then use it to form the reflectivity matrix in order to be able to cascade its response with the snow layer above it. However, it is important to note here that the slab width used for the snow, W_s, and for the rough surface, W_{RS}, may not necessarily be the same, which leads to different directions for the propagating plane waves. To help visualize what this means, we show in Fig. 5.5 the allowed propagation constants for $W_s = 16\lambda$ as empty circles and for $W_{RS} = 6\lambda$ as dotted circles. Consequently, the scattering matrix for the snow layer and the reflectivity matrix for the rough surface are computed for different angles. Therefore, cascading them directly does not result in
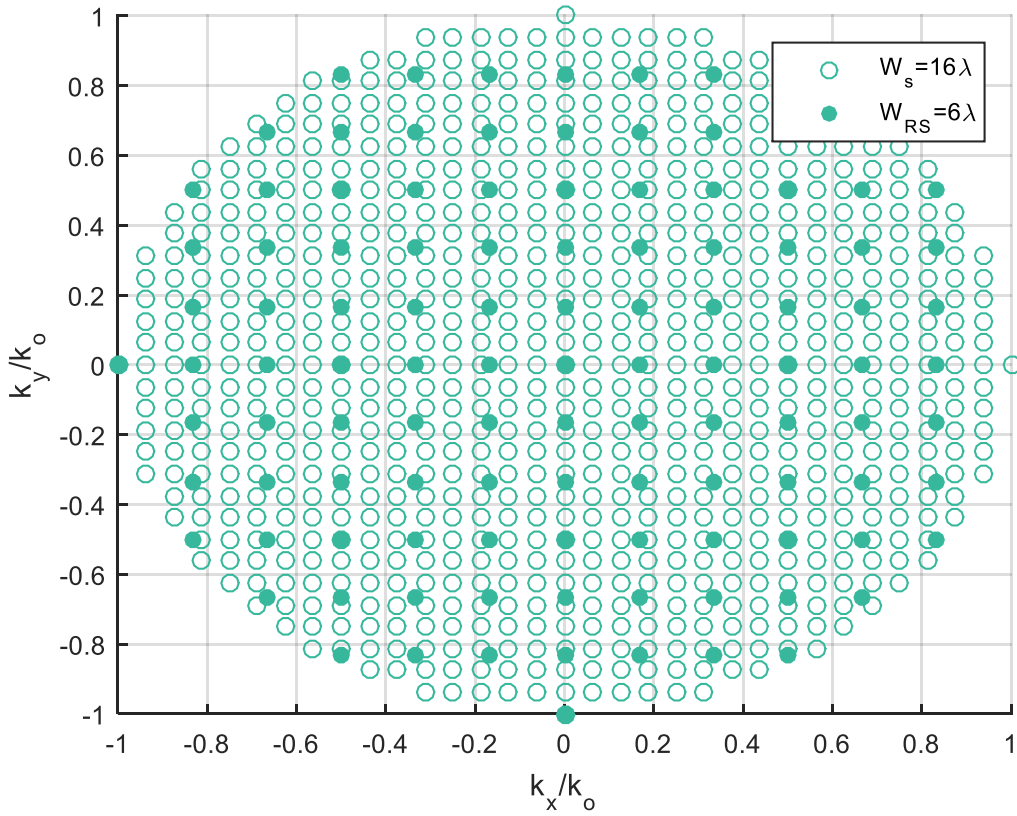
Figure 5.5 K-space and allowed k-values for a) snow slab with width of 16 λ, and b) rough surface with width of 6 λ.

accurate results. Consequently for full-wave solutions, like the FEKO used in here, the sparse directions have to be interpolated in order to match the grid to the snow slabs. One way to work around this is to use the $6\lambda \times 6\lambda$ FEKO samples to build a larger sample through the use of window functions. Specifically, we can build the spectral scattering behavior of a $16\lambda \times 16\lambda$ sample by multiplying a proper window function in space for each of the $6\lambda \times 6\lambda$ and then combine their responses to obtain the output for a larger sample. It is important to mention that the window function should be chosen in such a way that it allows intersections between adjacent samples and assures the continuity of the surface at these intersection points.
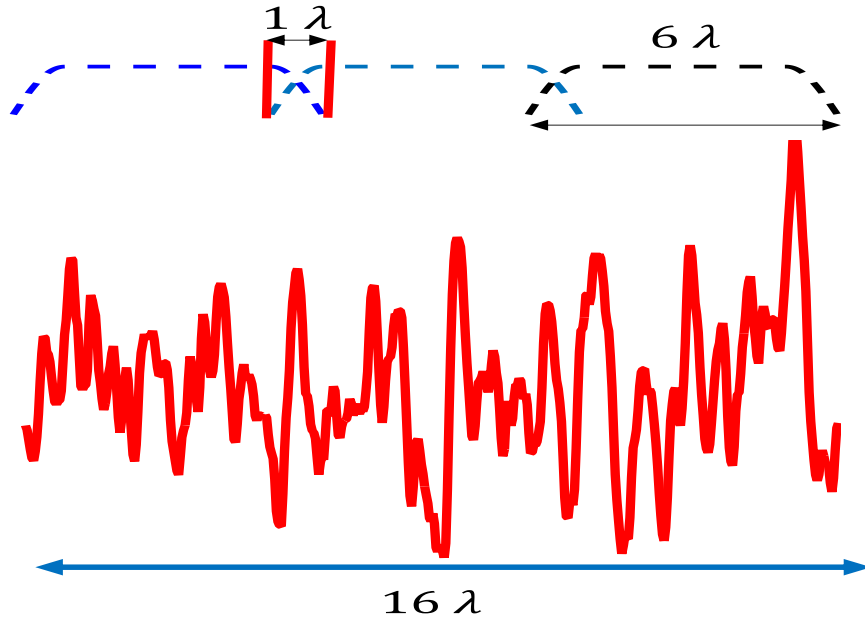
Figure 5.6 A 1-D illustration on how to use the window function to build a rough surface of $16\,\lambda$ length from $6\,\lambda$ samples.

An illustration on how to form a bigger sample ($16\,\lambda \times 16\,\lambda$) from the simulated samples ($\sim 6\,\lambda \times 6\,\lambda$) is shown in Fig. 5.6. A 1-D version of the used window function is given as follow

$$w(x) = \begin{cases} 1 & |x| < x_b \\ 1/2[1 + \cos^\gamma(\pi(x - x_a)/(x - xb))] & |x_b| < |x| < |x_a| \\ 0 & |x| > x_a \end{cases} \tag{5.2}$$

where, $\gamma, x_a, and\ x_b$ are chosen in a case by case basis since the width of our simulated samples ranges between $5.5\,\lambda\ to\ 6.25\,\lambda$. An example of such window function is depicted in Fig. 5.7.
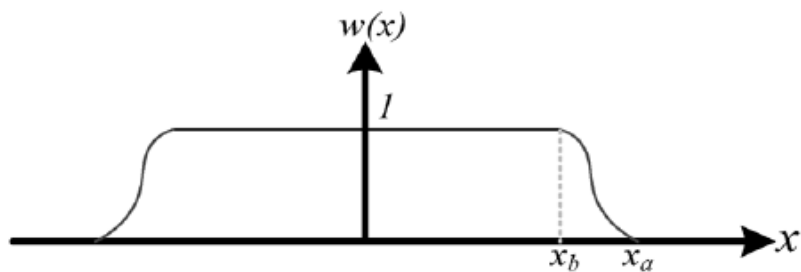
Figure 5.7 1-D example of the window function.

We should also mention that our window function is actually the 2-D version of the aforementioned case which could easily be expressed as in Eq. (5.3)

$$w(x, y) = w(x)w(y) \tag{5.3}$$

where $w(y)$ is written similar to $w(x)$ by replacing x by y. This way, we can form the reflectivity matrix of the aggregated rough surface on the same K-space as the snow response and then we just have to cascade them as discussed in Chapter 3.

5.5. Conclusions

The rough surface underneath the snowpack is represented with a reflectivity matrix that is computed through both analytical (PO) and numerical (CADFEKO) solutions. The solution is validated by comparing the results with existing empirical and numerical models as well as measured data.

Chapter 6

Snowpack Results and Discussions

6.1. Comparison with Measured Data

In this section, we present simulation results for a snow layer over a rough surface, which include the interaction of the scattering in the snow volume with the underlying surface. Traditionally, scattering by a snowpack is computed by incoherent addition of two separate components: (1) volume scattering by the snow layer as if it were over a smooth surface and (2) the scattering response of the underlying rough surface. In such an incoherent addition approach, the backscatter response of the rough surface is calculated as if the snow layer were a perfectly homogeneous dielectric medium, allowing for simply adding the volume and surface scattering components using superposition ($\sigma_t = \sigma_{RS} e^{-2\alpha d} + \sigma_v$). Incoherent addition of the powers assumes that the volume and surface scatterers do not interact with each other. In contrast, the cascading algorithm introduced in this study does take into account the interaction between the volume and surface scatterers. Even though each component is computed separately, our representation of scattering in the form of an S scattering matrix for the snow volume and a reflectivity matrix for the underlying surface serves to embed the coherency of the interactions between the two structures. Simulations for 3 snowpacks with thicknesses of 20, 60, and 102 cm, all over a rough surface, were performed at 9.5 GHz and the results are shown and compared to experimental measurements [79] in Fig. 6.1 (a), (b), and (c) respectively.
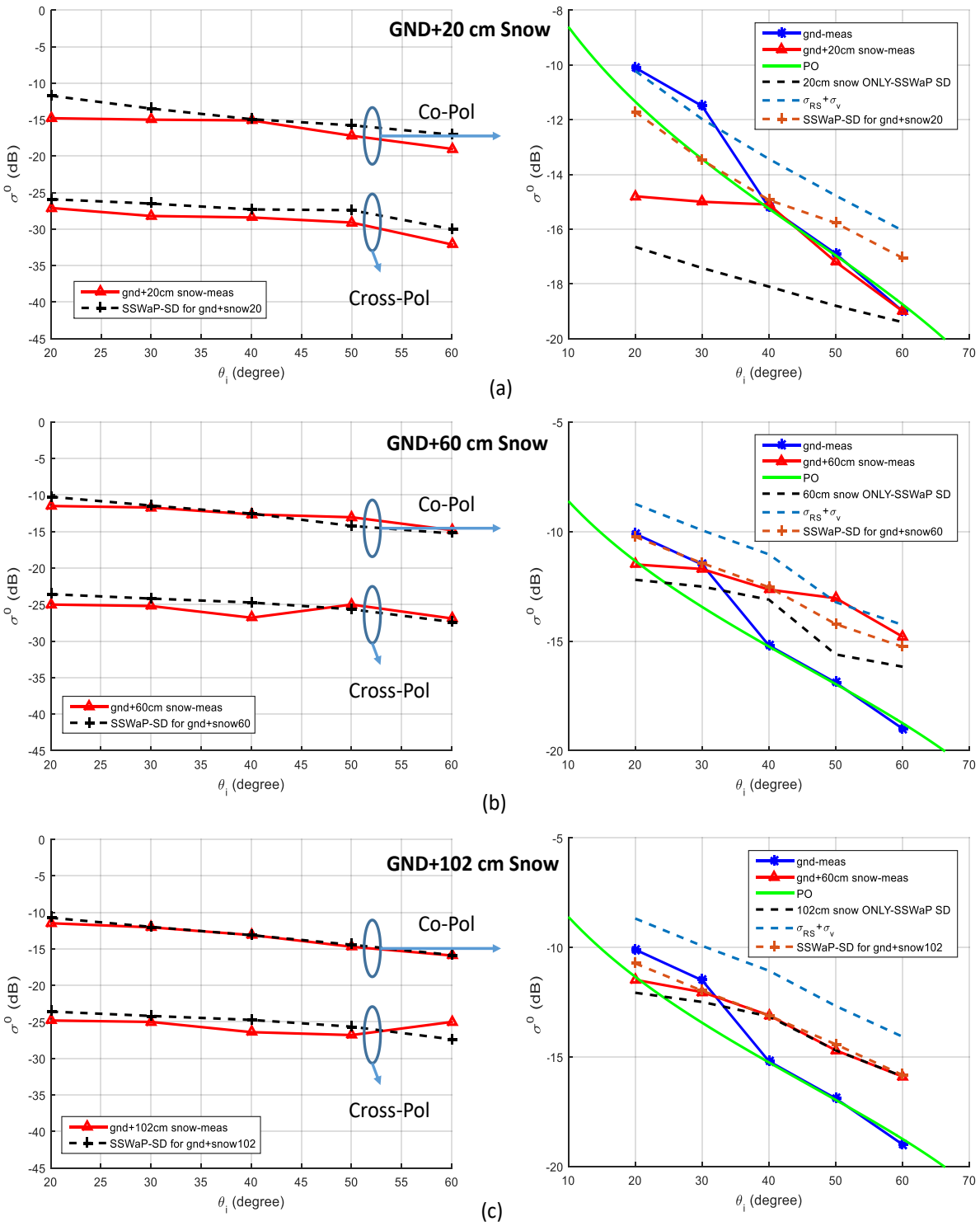
Figure 6.1 Backward scattering cross-section for snow-depth equals (a) 20 cm, (b) 60 cm, and (c) 102 cm.

The ground-truth data specifies an average snow density of $0.48 \ g/cm^3$ and an average particle diameter of 0.27 mm, which translates into a volume fraction of approximately 50%, a correlation length of 0.27 mm, and a chord size of 0.41 mm. The rough surface has a correlation length of 2.09 cm, rms height of 0.35 cm and a dielectric constant of $\epsilon_{gnd} = 4.6 - j0.1$. The three figures in the left-hand column of Fig. 6.1 contain values for the backscattering coefficient computed using all components and interactions comprising the model developed in the present study (shown in dashed black traces), along with the values measured experimentally (shown in solid red) as reported in [73]. The right hand column in Fig. 6.1 contains plots of the individual co-polarized contributions contained in the model. The contribution of the rough surface is referred to as "Gnd" and is calculated using the modified FEKO method described earlier in Chapter 5. The snow-only response is calculated for cascaded snow layers with no ground plane at all. For the 20-cm results, we observe that there is a noticeable difference between the SSWaP-SD for snow-only and the SSWaP-SD for snow over the rough surface, which is because the snow thickness is relatively small, allowing for a considerable amount of power to reach the rough surface and bounce back up to the surface. In contrast, for the thick-snow layer of 102cm, there is no significant difference between the results computed for the backscattering from the snow layer with or without the contribution of the underlying ground surface. It is also worth noting that for the 20-cm case, the coherent cascading of the rough surface and the snowpack responses gives results that differ from those based on the direct incoherent superposition of the individual response (compare solid red and dashed red traces in the top-left figure in Fig. 6.1). This is attributed to the interaction between the rough surface and the bottom snow layer.

The backscattering coefficient is plotted as a function of snow depth in Fig. 6.2. We observe a two-slope behavior in the backscattering response. This is attributed to the fact that the response of a thin snow layer is dominated by the contribution from the rough surface, but for a thicker layers there are enough random scatterers as to increase the attenuation through the layer down to the underlying surface and to simultaneously generate significant volume scattering to saturate the backscatter response and create a nonlinear slope with respect to the snow depth. In Fig. 6.2, we observe that for the shallow snow layer (20 cm), the difference between the model-computed backscattering coefficient and the measured value is about 0.75 dB. In contrast, for the thicker snow layers, the difference between computed and measured values of the backscattering coefficient is in the range of 0.15 dB.
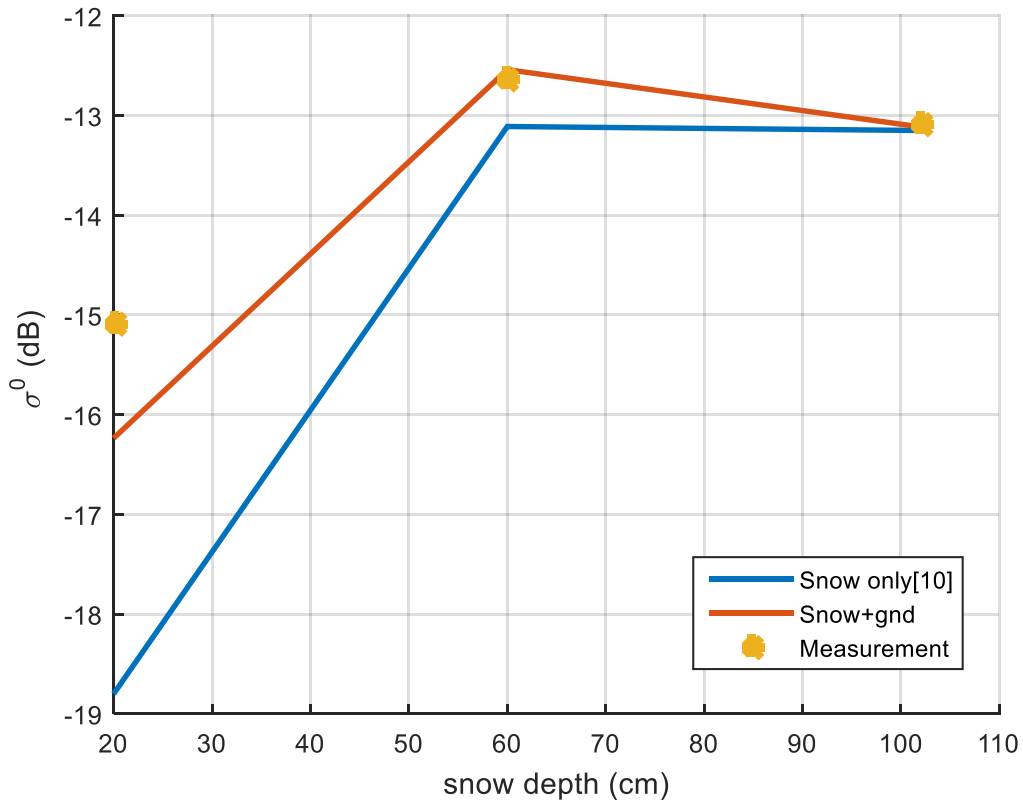
Figure 6.2 Backscattering cross-section versus snow-depth.

Additionally, our model is further validated against two other measured datasets reported in [95] at 9 and 16.6 GHz and the results are shown in Fig. 6.3 (a) and Fig. 6.3 (b), respectively. Both measured data were performed at 57 degrees of incidence angle but with slightly different ground truth snow parameters. In Fig. 6.3, we compare our model expectation (solid blue curve) to the measured data (dotted red circles) and the empirical model that has been reported [95] to best fit the measured data. The empirical model is given as follow

$$\sigma^0(dB) = 10 \log(C_1 - C_2 \, e^{-C_3 \rho_s d}) \tag{6.1}$$

where, ρ_s is the snow density, d is the snow depth, and $C_1, C_2, and \, C_3$ are the fitting parameters. Table 6-1 summarizes the values of these fitting parameters for each data set. As expected the fitting parameters are highly dependent on the frequency and the snow parameters as well. As shown in Fig. 6.3 (a), there is a very good agreement with our model expectation and the measured data set at 9 GHz. However, when comparing our model expectations to the measured data at 16.6 GHz as in Fig. 6.3 (b), there exist a good agreement about the saturation level of the backscattering coefficient at higher snow depths. On the other hand, at low snow depth, the level of accuracy is degraded due to the slight difference between our rough surface parameters to the ground truth surface roughness that has not been reported in [95].

Table 6-1 Summary of the fitting parameters in Eq. (6.1) for the two measured data sets

Data Set	C_1	C_2	C_3
$f = 9 \, GHz$	0.162	0.146	0.0199
$f = 16.6 \, GHz$	0.569	0.395	0.0487
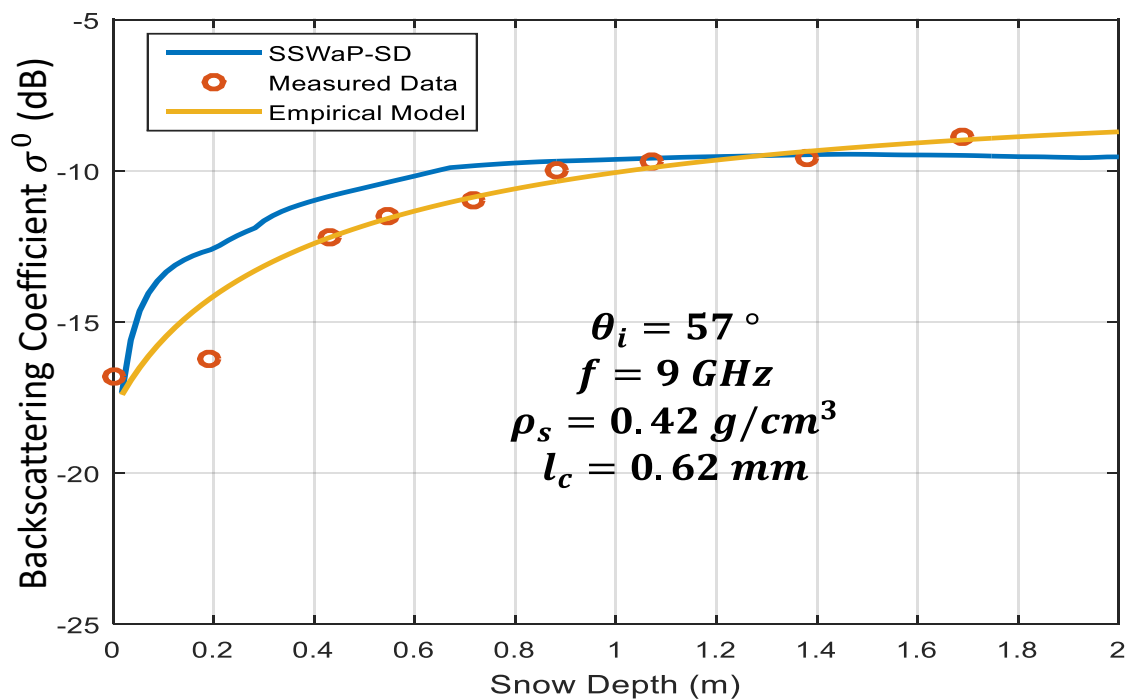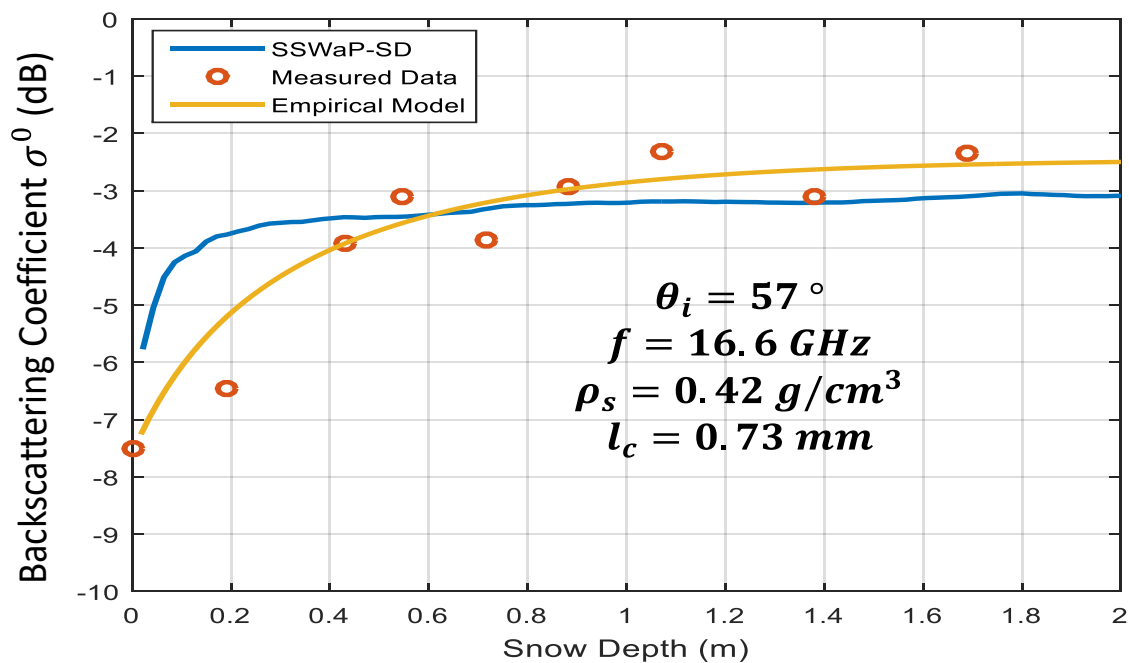
Figure 6.3 Validation of our model expectation of the normalized backscattering coefficient versus snow depth against measured data [95] at (a) 9 GHz, and (b) 16.6 GHz.

6.2. Phase Difference Statistics

After validating the model against measured data, we can use our technique to look at another important parameter which is the co-polarized phase difference statistics of the snowpack. The term co-polarized phase difference represents the phase difference between the HH and VV components of the backscattering coefficient and is denoted by $\phi = \phi_{hh} - \phi_{vv}$. The analytical formulation of how to calculate such a parameter is presented in the following sub-section. Afterwards, the statistics of our model data is presented and the co-polarized phase difference probability density function is calculated.

6.2.1. Co-Polarized Phase Difference Statistics: Analytical Solution

Fully polarimetric radar response of the snowpack is obtained by measuring both the magnitude and phase of each of the polarimetric component of the scattered field. However, most of the models and measurement campaigns report the backscattering coefficient only and neglect the measured phase information completely under the false impression that there are less information encapsulated in the phase. In fact, we can reach a closed form expression of the statistics, i.e. Probability Density Function (PDF), of the phase difference between the co-polarized components (HH, and VV) [96]. A fully polarimetric response of a target is characterized by its polarimetric scattering matrix that relates the scattered field to the incident field ($\bar{E}_s = \bar{\bar{S}}\bar{E}_i$). Such a scattering matrix is expressed in Eq. (6.2)

$$\bar{\bar{S}} = \begin{bmatrix} S_{vv} & S_{vh} \\ S_{hv} & S_{hh} \end{bmatrix} \tag{6.2}$$

where each element in the scattering matrix is a complex quantity. Hence, statistically speaking each of the polarimetric components of the scattering matrix should be expressed in two random

variables (representing the real and imaginary parts). Each of the polarimetric scattering component ($S_{pq}, p, q = v, h$) consists of the sum of the individual contributions of the random scatterers within the random medium and their multiple scattering interactions as well. Since the number of random scatterer inside the illuminated region of the random medium is usually very large, the central limit theorem can be applied. Hence, we can reach the conclusion that the real and imaginary parts of S_{pq} are identically distributed, zero-mean Gaussian random variables. Therefore, we can express the co-polarized components in terms of four joint random variables as in Eq. (6.3)

$$S_{vv} = X_1 + i\, X_2$$
$$S_{hh} = X_3 + i\, X_4$$

(6.3)

Observation of polarimetric data for various random media show that the cross-polarized components ($vh, or\ hv$) are statistically independent of the co-polarized components. Consequently, we can express the cross-polarized component in terms of another two independent, yet Gaussian, random variables as in Eq. (6.4)

$$S_{vh} = X_5 + i\, X_6$$

(6.4)

It is again reasonable to assume X_5 and X_6 to be jointly Gaussian. Therefore, the statistical behavior of S_{vh} can be obtained by getting the variance (σ_c^2) only in Eq. (6.5)

$$f_{X_5,X_6}(x_5, x_6) = \frac{1}{2\pi\sigma_c^2} e^{(-\frac{x_5^2+x_6^2}{2\sigma_c^2})}$$

(6.5)

However, the co-polarized random variables are statistically-dependent on each other. Hence, the covariance matrix (C) describes the joint probability density function between the four random variables of the co-polarized components in Eq. (6.3). Since X_1, X_2, X_3, and X_4 are Gaussian. Then C is expected to be a 4×4 symmetric matrix whose entries are expressed as [97]

$$\lambda_{ij} = \lambda_{ji} = \langle X_i X_j \rangle \qquad\qquad i,j \in \{1, \cdots, 4\} \tag{6.6}$$

Following the derivation in [98], we can relate the ensemble average Mueller matrix to the λ_{ij} as in Eq. (6.7)

$$\langle M \rangle = \begin{bmatrix} 2\lambda_{11} & 2\sigma_c^2 & 0 & 0 \\ 2\sigma_c^2 & 2\lambda_{33} & 0 & 0 \\ 0 & 0 & 2\lambda_{13} + 2\sigma_c^2 & 2\lambda_{14} \\ 0 & 0 & -2\lambda_{14} & 2\lambda_{13} - 2\sigma_c^2 \end{bmatrix} \tag{6.7}$$

where $\langle M \rangle$ is the ensemble average of the Mueller matrix. The Mueller matrix M can be easily written in terms of the polarimetric scattering matrix components as follows

$$M = \begin{bmatrix} |S_{vv}|^2 & |S_{vh}|^2 & R_e[S_{vv}S_{vh}^*] & -I_m[S_{vv}S_{vh}^*] \\ |S_{hv}|^2 & |S_{hh}|^2 & R_e[S_{hv}S_{hh}^*] & -I_m[S_{vv}S_{vh}^*] \\ 2R_e[S_{vv}S_{hv}^*] & 2R_e[S_{vh}S_{hh}^*] & R_e[S_{vv}S_{hh}^* + S_{vh}S_{hv}^*] & -I_m[S_{vv}S_{hh}^* - S_{vh}S_{hv}^*] \\ 2I_m[S_{vv}S_{hv}^*] & 2I_m[S_{vv}S_{vh}^*] & I_m[S_{vv}S_{hh}^* + S_{vh}S_{hv}^*] & R_e[S_{vv}S_{hh}^* - S_{vh}S_{hv}^*] \end{bmatrix} \tag{6.8}$$

Therefore, measuring the complex polarimetric components S_{pq} enables us to estimate the Mueller matrix where its ensemble average lead to the full knowledge of the covariance matrix elements λ_{ij} as summarized in Eq. (6.9)

$$\begin{aligned} \lambda_{11} &= \frac{\langle M_{11} \rangle}{2} \quad , \quad & \lambda_{11} &= \frac{\langle M_{22} \rangle}{2} \\ \lambda_{13} &= \frac{\langle M_{33} \rangle + \langle M_{44} \rangle}{4} \quad , \quad & \lambda_{14} &= \frac{\langle M_{34} \rangle - \langle M_{43} \rangle}{4} \end{aligned} \tag{6.9}$$

Hence, estimating the covariance matrix result in a full knowledge of the joint probability density function of the co-polarized random variables ($f_{X_1, \cdots, X_4}(x_1, \cdots, x_4)$). Using the following change of variables

$$\begin{aligned} x_1 &= \rho_1 \cos \phi_{vv} \quad , \quad & x_2 &= \rho_1 \sin \phi_{vv} \\ x_3 &= \rho_2 \cos \phi_{hh} \quad , \quad & x_4 &= \rho_2 \sin \phi_{hh} \end{aligned} \tag{6.10}$$

We can reach an easier form of such a density function as given in Eq. (6.11)

$$f_{\rho_1,\rho_2,\phi_{vv},\phi_{hh}}(\rho_1,\rho_2,\phi_{vv},\phi_{hh}) = \frac{\rho_1\rho_2}{4\pi\sqrt{\Delta}} e^{\left(-\frac{1}{2}[a_1\rho_1^2+a_2\rho_2^2-2a_3\rho_1\rho_2]\right)} \tag{6.11}$$

where $\Delta = (\lambda_{11}\lambda_{33} - \lambda_{13}^2 - \lambda_{14}^2)^2$, $a_1 = \lambda_{33}/\sqrt{\Delta}$, $a_2 = \lambda_{11}/\sqrt{\Delta}$, and $a_3 = [\lambda_{13}\cos(\phi_{hh} - \phi_{vv}) + \lambda_{14}\sin(\phi_{hh} - \phi_{vv})]/\sqrt{\Delta}$. In order to obtain the co-polarized phase difference statistics, we can integrate the density function in Eq. (6.11) over all the possible values of ρ_1 and ρ_2 as follow

$$f_{\phi_{vv},\phi_{hh}}(\phi_{vv},\phi_{hh}) = \int_{\rho_2=0}^{\infty}\int_{\rho_1=0}^{\infty} f_{\rho_1,\rho_2,\phi_{vv},\phi_{hh}}(\rho_1,\rho_2,\phi_{vv},\phi_{hh})\,d\rho_1 d\rho_2 \tag{6.12}$$

After some rigorous mathematical steps as reported in details in [98], we can end up with the following expression for the probability density function of the co-polarized phase difference ($\phi = \phi_{hh} - \phi_{vv}$)

$$f_\phi(\phi) = \frac{\lambda_{11}\lambda_{33} - \lambda_{13}^2 - \lambda_{14}^2}{2\pi(\lambda_{11}\lambda_{33} - D^2)}\left\{1 + \frac{D}{\sqrt{\lambda_{11}\lambda_{33} - D^2}}\left[\frac{\pi}{2} + \tan^{-1}\frac{D}{\sqrt{\lambda_{11}\lambda_{33} - D^2}}\right]\right\} \tag{6.13}$$

where $D = \lambda_{13}\cos\phi + \lambda_{14}\sin\phi$ and $\lambda_{11}, \lambda_{33}, \lambda_{13}$, and λ_{14} are all given in Eq. (6.9). Hence, using Eq. (6.13) leads to expectation of the probability density function of the co-polarized phase difference. It is worth noting that the phase difference is of more interest compared to the absolute phase since the measurement of the absolute phase of the scattering matrix elements S_{pq} is very challenging.

6.2.2. Statistics of the Polarimetric Backscattering from Snowpack

After examining the theoretical behavior of the polarimetric components of the scattering matrix S_{pq}, we can compare our model results to the analytical expressions we formulated in Section 6.2.1. First, we can look at the speckle statistics of the co-polarized scattering components expressed in Eq. (6.3) and examine their behavior. Figures 6.4 and 6.5 summarize the histograms

of the co-polarized components of the backscattering from a 2cm-thick snowpack with incident angle of 20 degrees, volume fraction of 50%, snow density of $0.48\ gm/cm^3$ and at frequency of 14.4 GHz using 60 realizations for the vv and hh components, respectively.
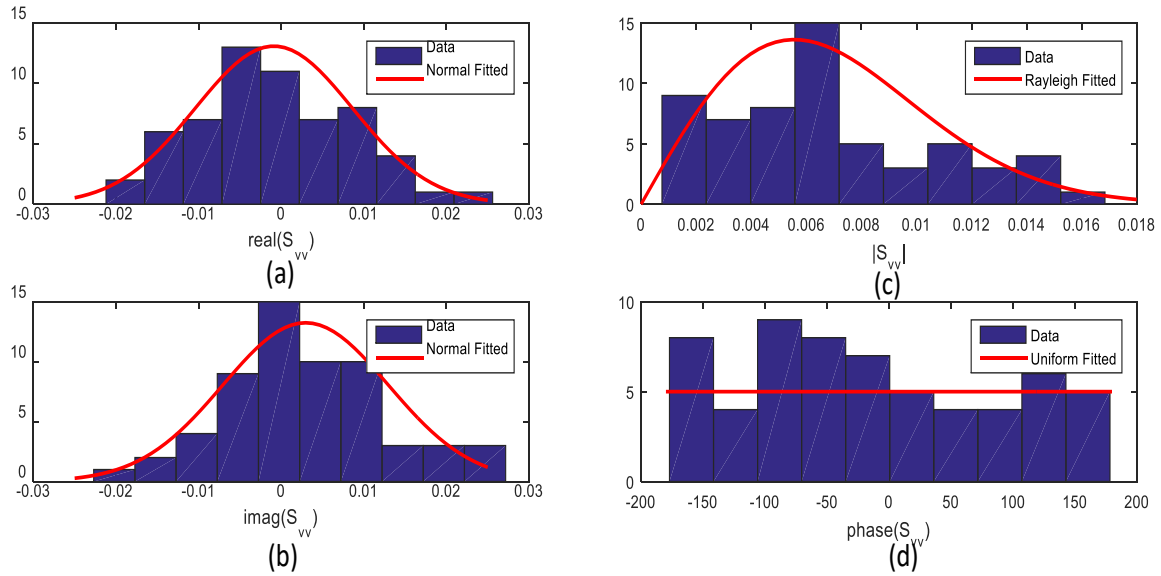
Figure 6.4 Speckle statistics of the vv component of the scattering matrix.
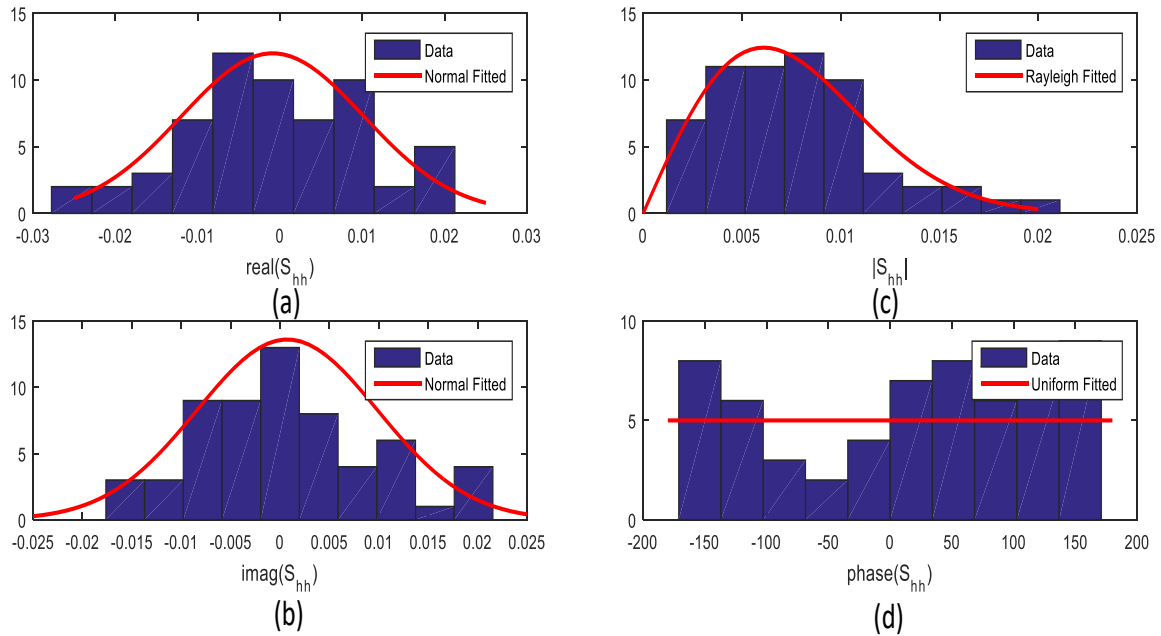
Figure 6.5 Speckle statistics of the hh component of the scattering matrix.

The histograms of our model vv component is shown in Fig. 6.4. The real and imaginary components fits a Gaussian (normal) distribution perfectly as depicted in Fig. 6.4 (a) and Fig. 6.4 (b), respectively. This matches the theoretical assumption we highlighted in expression the polarimetric scattering components statistically with zero-mean Gaussian random variables as in Eq. (6.3) and Eq. (6.4). Additionally, the statistics of S_{vv} magnitude matches a Rayleigh distribution so as expected and the phase statistics of S_{vv} matches a uniform distribution. Similar observation can be concluded for the S_{hh} statistics as depicted in Fig. 6.5. We could also examine the statistics of the cross-polarized component S_{vh} to assess the validity of Eq. (6.4) that again both the real and imaginary components should be zero-mean Gaussian variables. The results for the S_{vh} statistics are reported in Fig. 6.6. Again, the same observations can be concluded that the histograms of real and imaginary parts match zero-mean normal (Gaussian) distribution and the magnitude and phase are fitting a Rayleigh and uniform distributions, respectively.
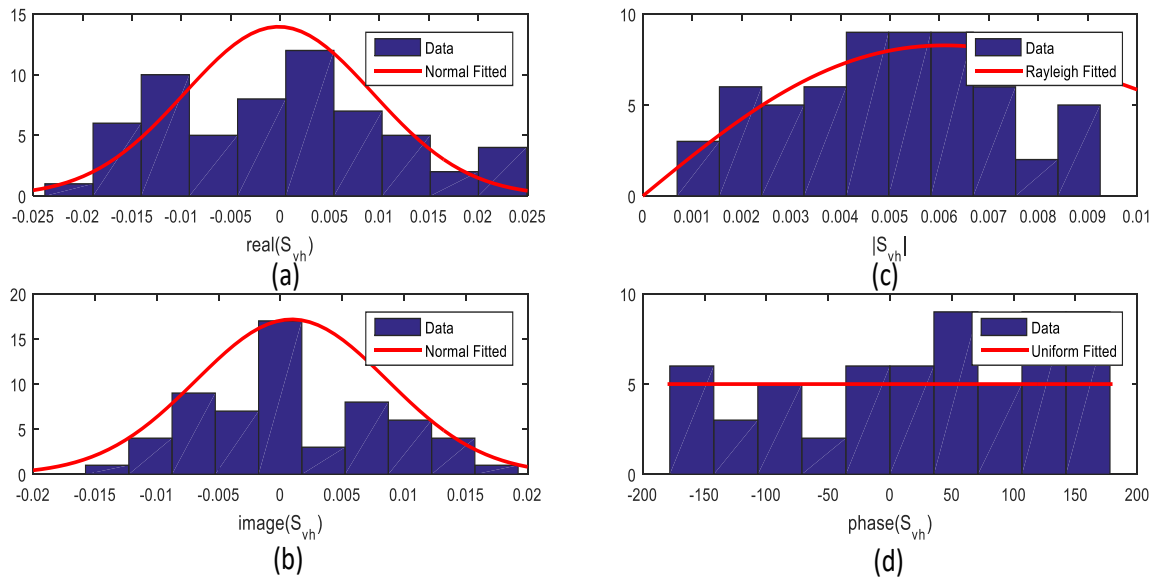
Figure 6.6 Speckle statistics of the vh component of the scattering matrix.

The major point of interest afterwards is the co-polarized phase difference statistics. We simulated 60 different realizations of 60cm-thick snowpacks with the same medium parameters as mentioned earlier in this section and estimated the polarimetric backscattering matrix using the SSWaP-SD technique. Then using Eq. (6.8), we calculated the Mueller matrix for each realization and then the ensemble average of the Mueller matrix is obtained. Afterwards, the covariance matrix elements λ_{ij}'s are calculated using Eq. (6.9) and the resulting ensemble average of the Mueller matrix. Finally, the $\lambda_{ij}'s$ are substituted in Eq. (6.13) to obtain the co-polarized phase difference density function. A comparison of the histogram of our model data with the analytical expression is depicted in Fig. 6.7 as show a very good agreement.
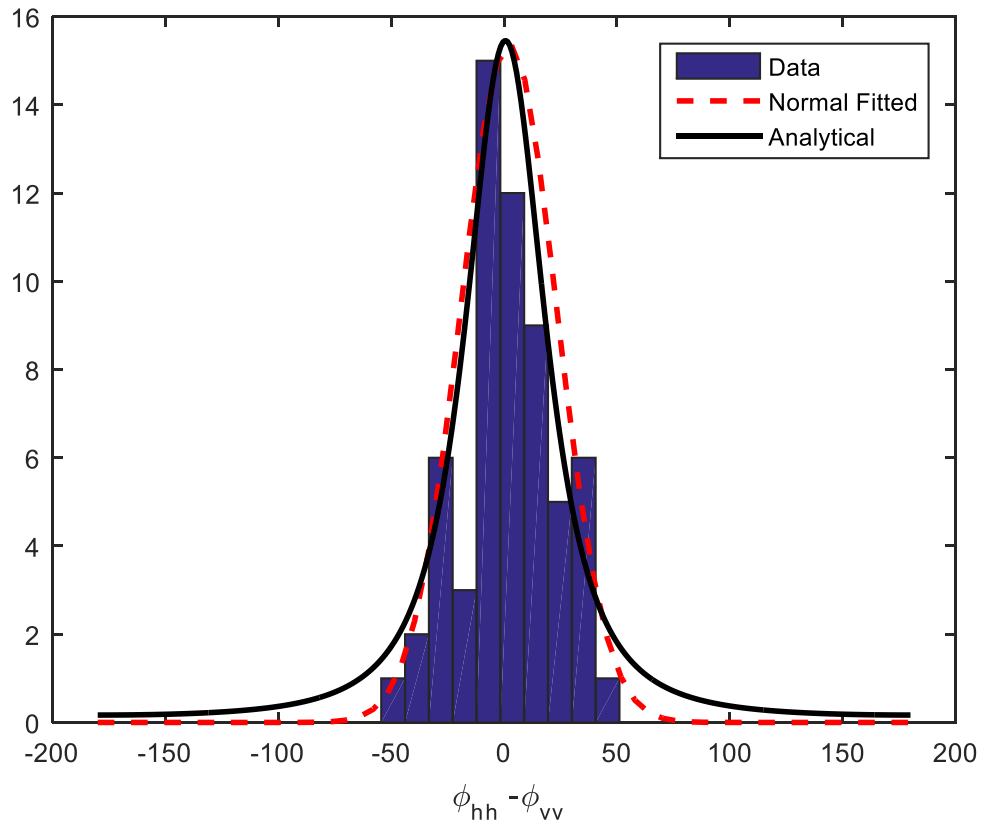
Figure 6.7 Co-polarized phase difference statistics of 60cm-thick snowpack.

6.3. Discussions

Another interesting point that we can observe is the response of a shallow snowpack over a rough surface with variable complex dielectric constant. The real part of the dielectric constant (ϵ_p) of the rough surface is swept from 4.5 to 10 with a fixed imaginary part of the dielectric constant $\epsilon_{pp} = 0.016$. The results of the backscattering coefficient are shown in Fig. 6.8. As we can see the higher is the dielectric constant, the higher is the backscattering coefficient as expected. We also swept the imaginary part of the ground dielectric constant (ϵ_{pp}) from 0 to 20 and the results are reported in Fig. 6.9 while the real part ϵ_p is kept fixed at 4.6. The same observation could be made, since the difference between the surface and air is getting higher which lead to
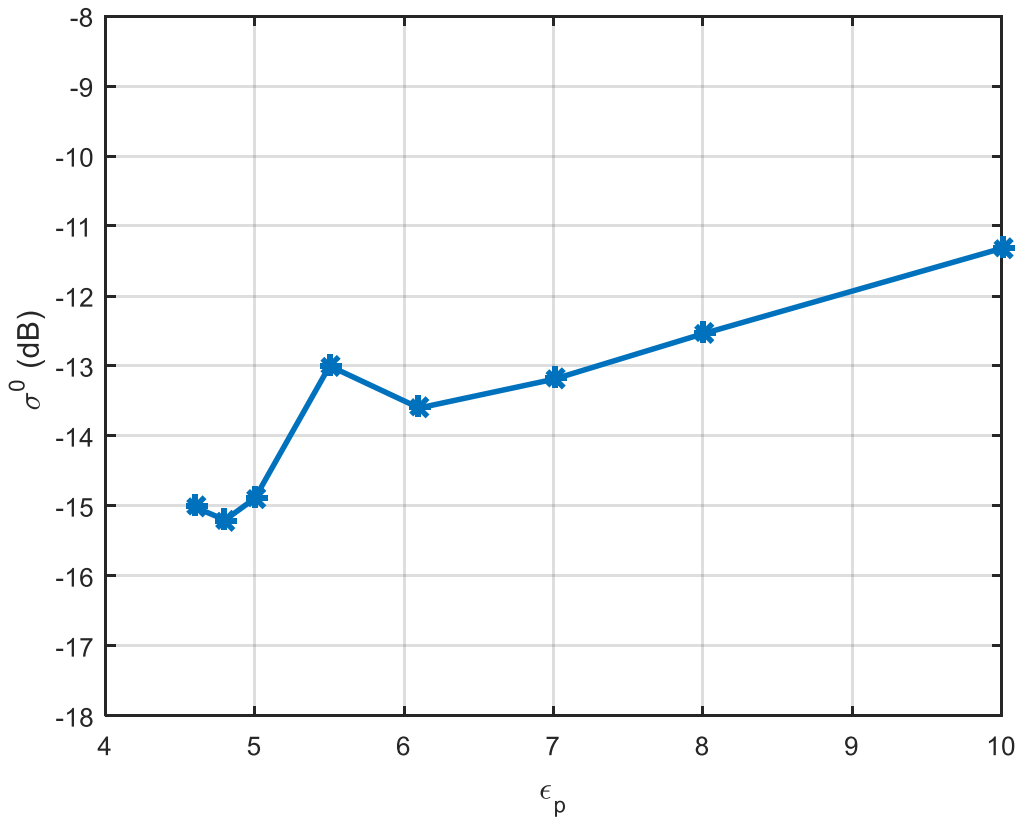
Figure 6.8 Backscattering cross-section versus the real part of ground dielectric constant (ϵ_p) for fixed imaginary part of the dielectric constant ($\epsilon_{pp} = 0.016$).
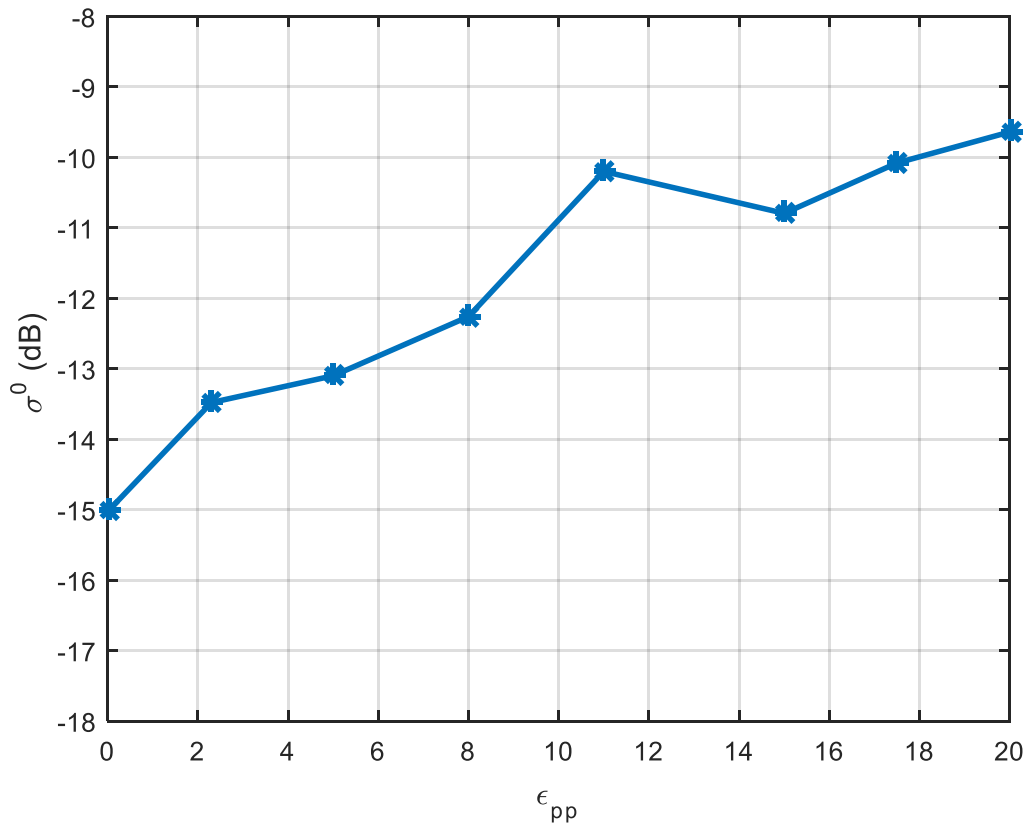
Figure 6.9 Backscattering cross-section versus the imaginary part of ground dielectric constant (ϵ_{pp}) for fixed real part of the dielectric constant ($\epsilon_p = 4.6$).

higher reflection from the surface. It is important to highlight that the SSWaP-SD method allows us to get the full response for a snow layer over any rough surface without the need of re-simulating the snow layer over and over.

Chapter 7

Conclusions and Future Work

7.1. Summary and Conclusions

The work in this thesis is focused on electromagnetic modeling for radar remote sensing from snow. A physics-based model is proposed to reconstruct the computer-generated samples of the snow through the implementation of both the Lineal-path function on top of the 3D exponential correlation function to ensure the macroscopic connectivity of the ice particles. The proposed reconstruction method is compared to both 2D and 3D sample images of real snow and show good resemblance. A fully-coherent time-efficient method is implemented to solve for the bistatic scattered fields from a snow layer with arbitrary thickness over rough surface. The technique exploits the SSWaP-SD approach as a time-efficient method to deal with the problem of the long-distance propagation in a complex media based on discretizing the composite medium into slabs and represent each slab with an N-dimension fully-polarimetric scattering matrix in the spectral domain. The individual snow slab problem is addressed using MoM code based on the discrete dipole approximation. The rough surface is represented with a scattering matrix as well using both analytical (PO) and numerical (CADFEKO) solutions. The full response is acquired by cascading both S-matrices together and validated using two measurement campaigns at X and Ku band respectively.

7.2. Future Work

The proposed simulation setup has been carried over multiple times for different snow parameters (volume fraction, correlation length, chord length, snow depth), roughness profiles (correlation length, rms height), operating frequencies, and incidence/scatter angles in order to form a complete library that could be used to build an inversion algorithm. Trials to get to a simple inversion algorithm were performed as an initial step but led to the conclusion that a rigorous neural network model needs to be built in order to guess the medium parameters from the backscattering coefficients.

On the other hand, higher order clustering functions could be used instead of the Lineal-path function to handle cases when volume fraction is very low. Additionally, we can apply the SSWaP-SD to different complex media like vegetation or we can use the SSWaP-SD a 3D domain decomposition method to solve for electromagnetic interference in high speed integrated circuits.

Appendix 1

Importing a Random Snow Sample into HFSS

8.1. Purpose

With all the recent advances of the EM computational methods, few commercial full-wave solvers are proven trust-worthy by the EM community. HFSS (or AnsysEM) is considered the most commonly-used 3-D EM solver by EM engineers. HFSS has been used extensively in many EM applications ranging from radiation to the scattering problems. However, using a commercial software to solve for scattering from a random medium is still very challenging. First issue relates to importing a sample of the random medium into HFSS which can be very challenging. This is due to the fact that HFSS offers the ability to draw/import only a few canonical objects such as sphere, box, cylinder, and some other objects. Additionally, most random media, such as snow, are infinite in extent. Hence, even if we were able to import/draw the medium into HFSS, a proper EM setup has to be performed in order to get accurate results in a feasible amount of time. The main objective of this appendix is to describe the process of importing a 3-D random medium structure from MATLAB into HFSS.

8.2. Importing a Snow Sample into HFSS

After using the proposed reconstruction method described in Chapter 4, we end up with a 3-D connectivity matrix representation the locations of the ice particles in the air-filled
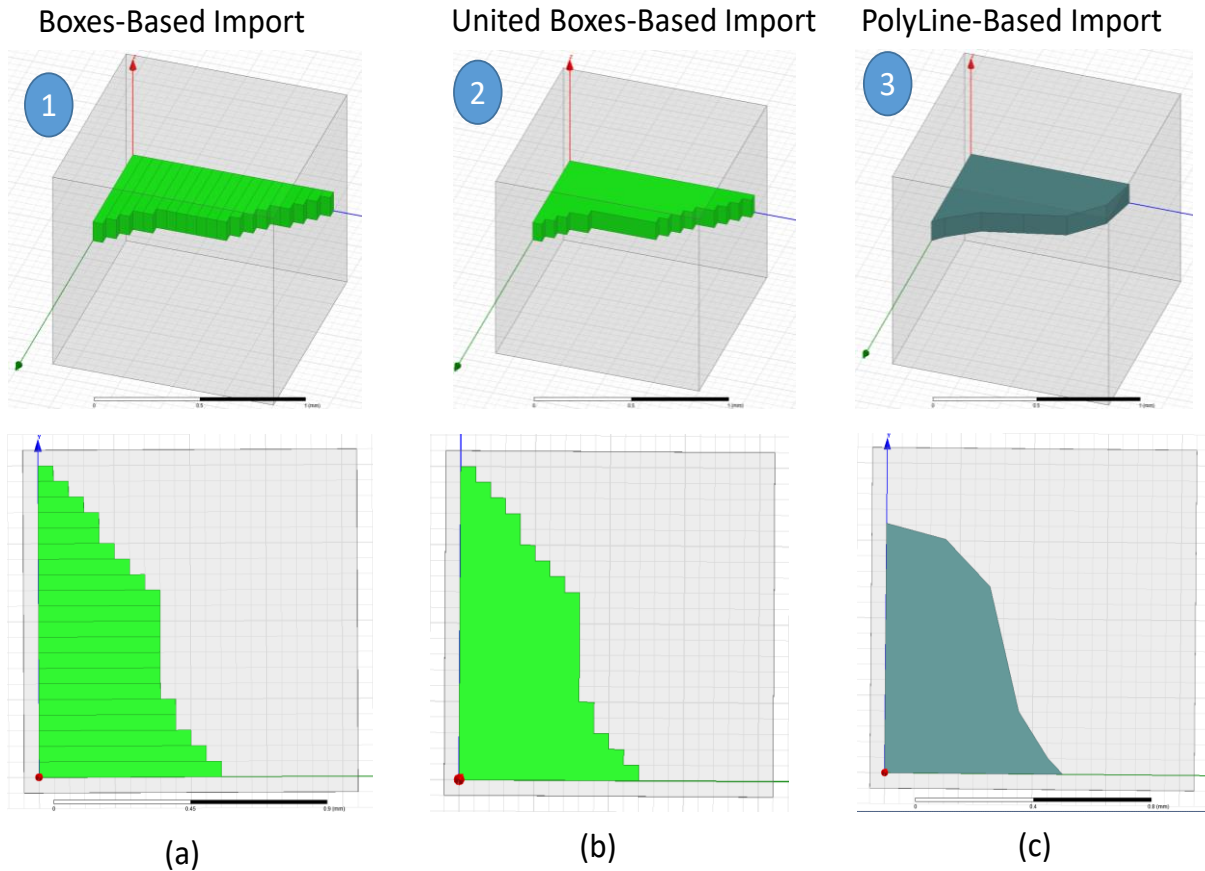
Figure 8.1 Different scenarios to draw a single snow grain into HFSS.

background. Therefore, we need to draw/import these ice particles into HFSS. First, let us concern

ourselves by just one snow grain and try to draw its equivalent shape into HFSS, then Fig. 8.1

depicts few scenarios of the imported snow grain. The brute-force scenario, not shown in Fig. 8.1,

is to represent each ice particle by a dielectric box and then draw those boxes into HFSS. However,

there are tremendous amount of ice-filled locations and importing such a huge number of boxes in

HFSS takes quite a lot of time. Alternatively, we can still use a box-based import scheme where

we just try to find the set of rectangular boxes that could be stacked horizontally to form the snow

grain as depicted in Fig. 8.1 (a). To examine the total number of unknowns resulting in HFSS after

its adaptive meshing algorithm is performed, we imported the snow grain in HFSS and surrounded

Table 7-1 Comparison of the three importing scenarios

Importing scheme	Number of unknowns	Importing time
Box-based	3352	~ 5 sec
United boxes-based	1667	~ 5.5 sec
Polyline-based	1066	< 0.1 sec

it with a small air-filled box as depicted in Fig 8.1 (a). The resulting number of unknowns is reported in Table 8-1 to be 3352 which is considered to be a big number given that the actual snow sample consists of millions of these snow grains. Therefore, we can unite the boxes drawn in the first scenario together to remove the mesh elements in between as performed in scenario 2 in Fig. 8.1 (b). The number of unknowns is reduced by half in this scenario compared to the first scenario. However, the snow grain geometry still suffers from the staircase approximation and the smallest step in the staircase dictates the smallest mesh element. It is also worth noting that, the importing time for the united boxes-based algorithm is a slightly higher than the first scenario importing algorithm. This is due to the fact that, HFSS takes additional time applying the Boolean operation to unite all the boxes. Hence, a polyline-based importing scheme is used as depicted in Fig. 8.1 (c). The snow grain is represented by a polyline that tracks the border points of it and draw a closed surface that is then swept along the vertical direction to get the 3-D snow grain. As reported in Table 8.1, the polyline-based importing scheme is more efficient in terms of both the total number of unknowns and the importing time. Then, we just have to repeat this scheme for the rest of the snow grains.

Another point is that the reconstructed snow sample as in Chapter 4 has been discretized with what we denote as the statistical discretization (must be much smaller than the correction length) which is quite smaller than the typical wavelength of EM waves used in radar remote
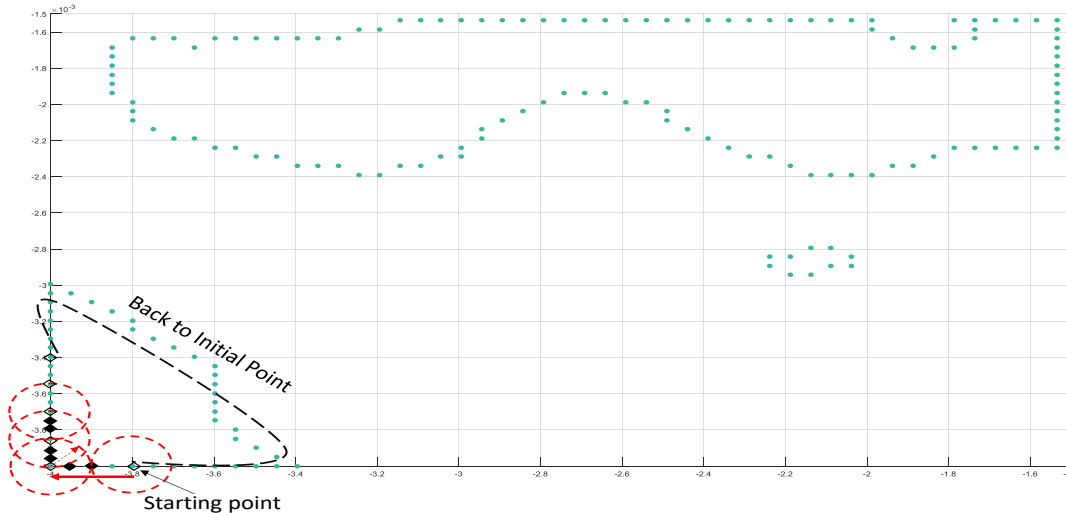
Figure 8.2 Polyline-based importing algorithm with discretization step.

sensing of snow. Therefore, we have to under-sample the medium which importing it into HFSS

to end up with a computationally-tractable problem. Such under-sampling is depicted in Fig. 8.2.

The polyline-based importing algorithm of a single snow grain starts by getting the list of

the border points. This step is implemented by modifying the built-in MATLAB function

"visboundaries". Then, we pick a point from the list as the starting point and draw a circle around

it with a prescribed radius that is related to the EM discretization steps ($\lambda/20$). Afterwards, we

pick our next point as the furthest point away from the center on the snow grain and drops the

points in between as illustrated in Fig. 8.2. In order to better visualize the effect of the

aforementioned under-sampling process, we plotted the same snow grain with and without the

under-sampling in Fig. 8.3 (a) and Fig. 8.3 (b), respectively. After optimizing our polyline-based

importing algorithm, we turn the closed polyline shaped snow grain into a visual basic script that

can be run into HFSS to do the importing step automatically. Hence, we repeat the same procedure

for each of the snow grains to get our 2-D snow cut imported into HFSS. As described in Chapter

5, we then assume there is no change in the vertical direction for $\lambda/20$ and stack different layers

to form the 3-D snow sample. An example of two-stacked layers is shown in Fig. 8.4.

(a)   (b)

Figure 8.3 Illustration of the same snow grain imported (a) with, and (b) without the under-

sampling technique.

Figure 8.4 A sample of 3-D snow imported into HFSS by stacking two 2-D cuts.

BIBLIOGRAPHY

[1]   B. Arheimer, G. Lindström, J. Olsson, "A systematic review of sensitivities in the Swedish flood-forecasting system," Atmospheric Research, vol. 100, issues 2-3, pp. 275-284, 2011.
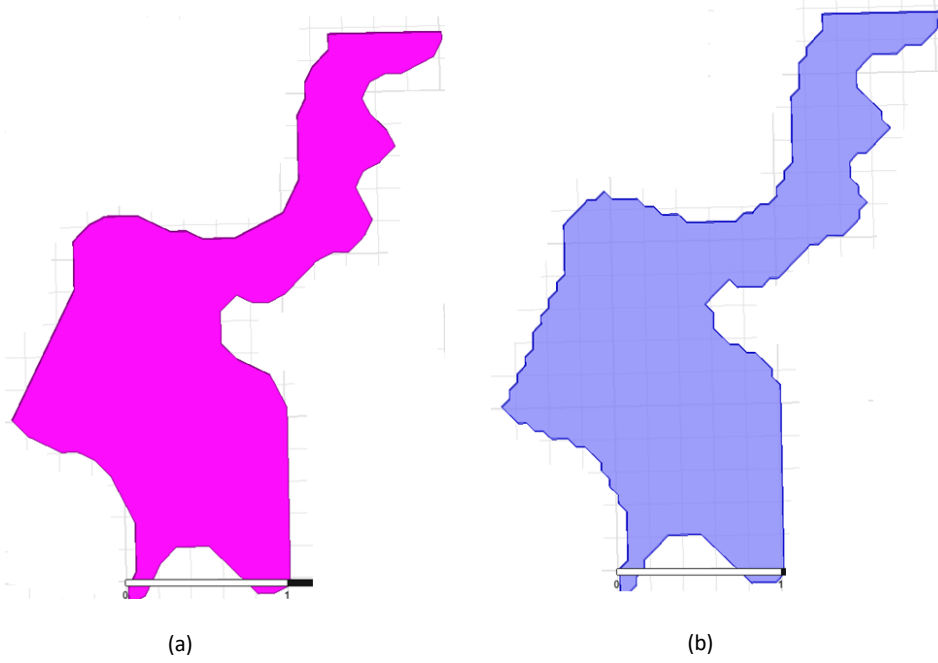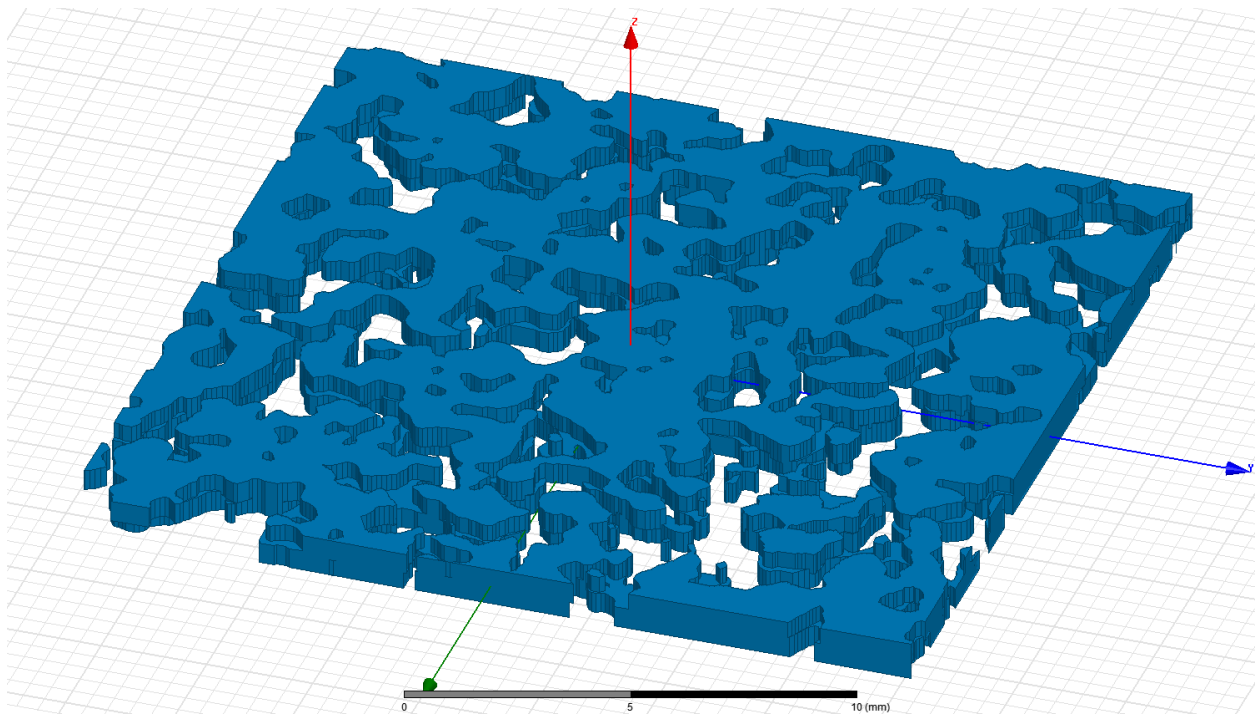
[2]   H. Biemans, C. Siderius, A. F. Lutz, S. Nepal, B. Ahmad, T. Hassan, W. von Bloh, R. R. Wijngaard, P. Wester, A. B. Shrestha and W. W. Immerzeel "Importance of snow and glacier meltwater for agriculture on the Indo-Gangetic Plain," Nature Sustainability, vol. 2, pp. 594–601, July 2019.

[3]   S. R. Fassnacht, K. A. Dressler, and R. C. Bales, "Snow water equivalent interpolation for the Colorado River Basin from snow telemetry (SNOTEL) data," Water Resources Research, vol. 39, no. 8, pp. 1208-1218, 2003.

[4]   https://www.weather.gov/marfc/Snow

[5]   https://www.nrcs.usda.gov/wps/portal/nrcs/detail/null/?cid=nrcseprd1314833

[6]   K. Libbrecht, "Field Guide to Snowflakes," 1st ed., Voyager Press, 2006.

[7]   "All About Snow." National Snow and Ice Data Center. https://nsidc.org/cryosphere/snow.

[8]   R. S. Williams, and J. G. Ferrigno, "State of the Earth's cryosphere at the beginning of the 21st century -- Glaciers, global snow cover, floating ice, and permafrost and periglacial environments: Chapter A" Satellite image atlas of glaciers of the world, pp. 1386-A, 2012.

[9]   J. Shi, C. Xiong, and L. Jiang, "Review of snow water equivalent microwave remote sensing," Science China Earth Science, vol.59, pp.731–745, April 2016.

[10]   X. Zheng, Q. Wang, L. Zhou, Q. Sun, and Q, Li, "Predictive Contributions of Snowmelt and Rainfall to Streamflow Variations in the Western United States", Advances in Meteorology, vol. 2018, Article ID 3765098, 14 pages, 2018.

[11]   P. H. Gleick, "Water resources. In Encyclopedia of Climate and Weather", ed. by S. H. Schneider, Oxford University Press, New York, vol. 2, pp. 817-823, 1996.

[12]   I. Shiklomonov, and P. H. Gleick, "Water in crisis: A guide to the world's fresh water resources," Oxford University Press, New York, 1993.

[13]   D. Archer and D. Stewart, "The Installation and Use of a Snow Pillow to Monitor Snow Water Equivalent," Water and Environment Journal, vol. 9, pp 221-230, June 1995.

[14] K. A. Dressler, S. R. Fassnacht, and R. C. Bales "A Comparison of Snow Telemetry and Snow Course Measurements in the Colorado River Basin," Journal of Hydrometeorology, vol. 7, no. 4, pp. 705-7012, 2006.

[15] R. Rice, and R. C.Bales, "Embedded-sensor network design for snow cover measurements around snow pillow and snow course sites in the Sierra Nevada of California," Water Recourses Research, vol. 46, no. 3, 2010.

[16] https://www.wcc.nrcs.usda.gov/about/mon_automate.html

[17] J. R. Kendra, F. T. Ulaby and K. Sarabandi, "Snow probe for in situ determination of wetness and density," in IEEE Transactions on Geoscience and Remote Sensing, vol. 32, no. 6, pp. 1152-1159, Nov. 1994.

[18] N. Kinar and J. Pomeroy, "Automated determination of snow water equivalent by acoustic reflectometry," IEEE Transactions on Geoscience and Remote Sensing, vol. 47, no. 9, pp. 3161–3167, Sep. 2009.

[19] J. Deems, T. Painter, and D. Finnegan, "Lidar measurement of snow depth: A review." Journal of Glaciology, vol. 59, no. 215, pp. 467-479, 2013.

[20] J. S. Deems, and T. Painter. "Lidar Measurement of Snow Depth: Accuracy and Error Sources." Proceedings of the International Snow Science Workshop, Telluride, Colorado, 2006.

[21] M. Tedesco, C. Derksen, J. S. Deems, and J. L. Foster, "Remote sensing of snow depth and snow water equivalent," Remote Sensing of the Cryosphere, ed. 1, pp. 78-93, 2015.

[22] S. Leinss, A. Wiesmann, J. Lemmetyinen and I. Hajnsek, "Snow Water Equivalent of Dry Snow Measured by Differential Interferometry," IEEE Journal of Selected Topics in Applied Earth Observations and Remote Sensing, vol. 8, no. 8, pp. 3773-3790, Aug. 2015, doi: 10.1109/JSTARS.2015.2432031.

[23] F. Ulaby and D. Long, "Microwave radar and radiometric remote sensing," Artech House 2015.

[24] T. Guneriussen, K. A. Høgda, H. Johnsen, and I. Lauknes, "InSAR for estimation of changes in snow water equivalent of dry snow," IEEE Transactions on Geoscience and Remote Sensing, vol. 39, no. 10, pp. 2101–2108, Oct. 2001.

[25] N. Saberi, R. Kelly, M. Flemming, and Q. Li, "Review of snow water equivalent retrieval methods using spaceborne passive microwave radiometry", International Journal of Remote Sensing, vol. 41, no. 3, pp. 996-1018, 2020.

[26] F. Koch, P. Henkel, F. Appel, L. Schmid, H. Bach, M. Lamm, et al, "Retrieval of snow water equivalent, liquid water content, and snow height of dry and wet snow by combining GPS signal attenuation and time delay," Water Resources Research, vol. 55, pp. 4465– 4487, 2019.

[27] A. Patil, G. Singh, and C. Rüdiger, "Retrieval of Snow Depth and Snow Water Equivalent Using Dual Polarization SAR Data," Remote Sensing, vol. 1, no. 7, pp. 1183-1194, 2020.

[28] L. Tsang, T. Liao, S. Tan, H. Huang, T. Qiao, and K. Ding, "Rough Surface and Volume Scattering of Soil Surfaces, Ocean Surfaces, Snow, and Vegetation Based on Numerical Maxwell Model of 3-D Simulations.", IEEE Journal of Selected Topics in Applied Earth Observations and Remote Sensing. pp. 1-18. July 2017.

[29] Y. Yang, W. Luo, B. Yin, and Y. Ren, "Electromagnetic Scattering of Rough Ground Surface Covered by Multilayers Vegetation," International Journal of Antennas and Propagation, Hindawi, vol. 19, pp. 1687-5869, April 2019.

[30] H. Yuan, J. H. Lee, and J. E. Guilkey, "Stochastic reconstruction of the microstructure of equilibrium form snow and computation of effective elastic properties," Journal of Glaciology, vol. 56, issue 197, pp. 405-414, Aug. 2010.

[31] K. K. Tse, L. Tsang, C. H. Chan, K. H. Ding and K. W. Leung, "Multiple scattering of waves by dense random distributions of sticky particles for applications in microwave scattering by terrestrial snow," Radio Science, vol. 42, no. 05, pp. 1-14, Oct. 2007.

[32] L. Tsang, K. H. Ding, S. Huang and X. Xu, "Electromagnetic Computation in Scattering of Electromagnetic Waves by Random Rough Surface and Dense Media in Microwave Remote Sensing of Land Surfaces," Proceedings of the IEEE, vol. 101, no. 2, pp. 255-279, Feb. 2013.

[33] K. H. Ding, X. Xu and L. Tsang, "Electromagnetic Scattering by Bicontinuous Random Microstructures with Discrete Permittivities," IEEE Transactions on Geoscience and Remote Sensing, vol. 48, no. 8, pp. 3139-3151, Aug. 2010.

[34] W. Chang, K. H. Ding, L. Tsang and X. Xu, "Microwave Scattering and Medium Characterization for Terrestrial Snow With QCA–Mie and Bicontinuous Models: Comparison Studies," IEEE Transactions on Geoscience and Remote Sensing, vol. 54, no. 6, pp. 3637-3648, June 2016.

[35] A. J. Dietz, C. Kuenzer, U. Gessner and S. Dech, "Remote sensing of snow – a review of available methods," International Journal of Remote Sensing, vol. 33, no. 13, pp. 4094-4134, 2012.

[36] M. Tedesco and E. J. Kim, "Intercomparison of Electromagnetic Models for Passive Microwave Remote Sensing of Snow," IEEE Transactions on Geoscience and Remote Sensing, vol. 44, no. 10, pp. 2654-2666, Oct. 2006.

[37] Y. Q. Jin, "Electromagnetic Scattering Modeling for Quantitative Remote Sensing," Newyork:Wiley, 1993.

[38] J. T. Pulliainen, J. Grandell and M. T. Hallikainen, "HUT snow emission model and its applicability to snow water equivalent retrieval," IEEE Transactions on Geoscience and Remote Sensing, vol. 37, no. 3, pp. 1378-1390, May 1999.

[39] A. Wiesmann and C. Mätzler, "Microwave Emission Model of Layered Snowpacks," Remote Sens. Environ., vol. 70, no. 3, pp. 307–316, 1999.

[40] L. Tsang, J. A. Kong, and R. T. Shin, "Theory of Microwave Remote Sensing," NewYork: Wiley, 1985.

[41] A. Stogryn, "A Study of the Microwave Brightness Temperature of Snow from the Point of View of Strong Fluctuation Theory," IEEE Transactions on Geoscience and Remote Sensing, vol. GE-24, no. 2, pp. 220-231, March 1986,

[42] Y. Q. Jin and J. A. Kong, "Strong fluctuation theory for electromagnetic wave scattering by a layer of random discrete scatterers," Journal of Applied Physics, vol. 55, no. 5, pp. 1364-1369, 1984.

[43] A. Wiesmann, C. Matzler, and T. Weise "Radiometric and structural measurements of snow samples," Journal of Radio Science, vol.3, no.2, pp. 273 -29, 1998.

[44] C. Mätzler, "Relation between grain-size and correlation length of snow," Journal of Glaciology, vol. 48, no. 162, pp.461-466, 2002.

[45] Y-L. S. Tsai, A. Dietz, N. Oppelt, and C. Kuenzer, "Remote Sensing of Snow Cover Using Spaceborne SAR: A Review," Remote Sensing, vol. 11, pp. 1456-1465, 2019.

[46] L. M. Pant, S. K. Mitra, and M. Secanell, "Stochastic reconstruction using multiple correlation functions with different-phase-neighbor-based pixel selection, "Physics Review E vol. 90, 2014.

[47] S. Tan, J. Zhu, L. Tsang and S. V. Nghiem, "Microwave Signatures of Snow Cover Using Numerical Maxwell Equations Based on Discrete Dipole Approximation in Bicontinuous Media and Half-Space Dyadic Green's Function," IEEE Journal of Selected Topics in Applied Earth Observations and Remote Sensing, vol. 10, no. 11, pp. 4686-4702, Nov. 2017.

[48] P. Hermansson, G. Forsell, and J. Fagerstom, "A review of models for scattering from rough surfaces," Scientific Report, Swedish Defense Research Agency, ISSN 1650-1942, Nov. 2002.

[49] K. Sarabandi, "Electromagnetic Scattering from Vegetation Canopies," Ph.D. Thesis, The University of Michigan, 1989.

[50] L. Tsang, J. A. Kong, K.-H. Ding, and C. O. Ao, Scattering of Electromagnetic Waves,vol. 2, Numerical Simulations." New York: Wiley-Interscience, 2001.

[51] S. O. Rice, "Reflection of electromagnetic waves from slightly rough surfaces," Communication Pure Applied Mathematics, vol 4, pp. 351, 1951.

[52] M. Sanamzadeh, L. Tsang, J. T. Johnson, R. J. Burkholder, and S. Tan, "Scattering of electromagnetic waves from 3D multilayer random rough surfaces based on the second-order small perturbation method: energy conservation, reflectivity, and emissivity," Journal of Optical Society of America A, vol. 34, pp. 395-409, 2017.

[53] P. Beckmann, and A. Spizzichino, "The scattering of electromagnetic waves from rough surfaces," Norwood, MA, Artech House, Inc1987.

[54] C. Macaskill, "Geometric optics and enhanced backscatter from very rough surfaces," Journal of Optical Society of America A, vol. 8, pp. 88-96, 1991.

[55] J. S. Asvestas, "The physical optics method in electromagnetic scattering," Journal of Mathematical Physics, vol. 21, no. 2, pp. 290-299, Feb. 1980.

[56] Lemaire, D., Sobieski, P., Craeye, C., and Guissard, A., "Two-scale models for rough surface scattering: Comparison between the boundary perturbation method and the integral equation method," Radio Science., vol. 37, no. 1, pp. 1-16, 2002.

[57] Y. Oh, K. Sarabandi, and F. T. Ulaby, "An empirical model and an inversion technique for radar scattering from bare soil surfaces," IEEE Transactions on Geoscience and Remote Sensing, vol. 30, no. 2, March 1992.

[58] P. C. Dubois, J. vanZyl and T. Engman, "Measuring Soil Moisture with Imaging Radars", IEEE Transactions on Geoscience and Remote Sensing, vol. 33, no. 6, pp. 1340-, Nov. 1995,

[59] A.K. Fung, W.Y. Liu, K.S. Chen & M.K. Tsay "An Improved IEM Model for Bistatic Scattering From Rough Surfaces," Journal of Electromagnetic Waves and Applications, vol. 16, no. 5, pp. 689-702, 2002.

[60] M. Y. Xia, C. H. Chan, S. Q. Li, B. Zhang and L. Tsang, "An efficient algorithm for electromagnetic scattering from rough surfaces using a single integral equation and multilevel sparse-matrix canonical-grid method," in IEEE Transactions on Antennas and Propagation, vol. 51, no. 6, pp. 1142-1149, June 2003,

[61] Z. Zhao and H. X. Ye, "Sparse Matrix Canonical Grid Method for Three-Dimension Rough Surface" 2018 International Conference on Microwave and Millimeter Wave Technology (ICMMT), May 2018.

[62] S. Huang, L. Tsang, E. G. Njoku and K. S. Chan, "Backscattering Coefficients, Coherent Reflectivities, and Emissivities of Randomly Rough Soil Surfaces at L-Band for SMAP Applications Based on Numerical Solutions of Maxwell Equations in Three-Dimensional Simulations," in IEEE Transactions on Geoscience and Remote Sensing, vol. 48, no. 6, pp. 2557-2568, June 2010

[63] J. Zhu and L. Tsang, "Electromagnetic Scattering from Random Rough Surfaces with Multiple Elevations for GNSS-R Land Applications," 2019 IEEE International Symposium on Antennas and Propagation and USNC-URSI Radio Science Meeting, Atlanta, GA, USA, pp. 169-170, 2019.

[64] L. Tsang et al., "Active and Passive Vegetated Surface Models With Rough Surface Boundary Conditions From NMM3D," in IEEE Journal of Selected Topics in Applied Earth Observations and Remote Sensing, vol. 6, no. 3, pp. 1698-1709, June 2013.

[65] M. A. Davis, S. D. C. Walsh, and M. O. Saar, "Statistically reconstructing continuous isotropic and anisotropic two-phase media while preserving macroscopic material properties," Physics. Review E, vol. 83, 2010.

[66] L. M. Pant, S. K. Mitra, and M. Secanell, "Stochastic reconstruction using multiple correlation functions with different-phase-neighbor-based pixel selection," Physics Review E, vol. 90, 2014.

[67] M. Zaky and K. Sarabandi, "Electromagnetic scattering from a 3D random volume using SSWaP-SD method for radar remote sensing of snow," 2016 IEEE International Geoscience and Remote Sensing Symposium (IGARSS), Beijing, 2016, pp. 1892-1894

[68] A.A. Ibrahim, and K. Sarabandi, "Simulation of Long Distance Wave Propagation in 2-D Sparse Random Media: A Statistical S-Matrix Approach in Spectral Domain," IEEE Transactions Antennas and Propagation, vol.62, no.5, pp.2708-2720, May 2014.

[69] F. Wang and K. Sarabandi, "A Physics-Based Statistical Model for Wave Propagation through Foliage," IEEE Transactions on Antennas and Propagation, vol. 55, no. 3, pp. 958-968, March 2007.

[70] T. Melamed, "TE and TM beam decomposition of time-harmonic electromagnetic waves," Journal of Optical Society of America A, vol. 28, pp. 401-409, 2011.

[71] G. R. Simpson, "A Generalized n-Port Cascade Connection," 1981 IEEE MTT-S International Microwave Symposium Digest, Los Angeles, CA, USA, pp. 507-509, 1981,.

[72] M. Zaky and K. Sarabandi, "Physics-Based Modeling and Electromagnetic Scattering Computation for Snow-Packs," 2019 IEEE MTT-S International Conference on Numerical Electromagnetic and Multiphysics Modeling and Optimization (NEMO), Boston, MA, USA, pp. 1-4, 2019.

[73] B. Draine and P. Flatau, "Discrete-Dipole Approximation For Scattering Calculations," Journal of Optical Society of America, A, vol. 11, pp. 1491-1499 (1994).

[74] B. E. Barrowes, F. L. Teixeira, and J. A. Kong "Fast algorithm for matrix–vector multiply of asymmetric multilevel block-Toeplitz matrices in 3-D scattering," Microwave and Optical Technology Letters, vol. 31, no.1, Oct. 2001.

[75] M. M. Zaky and K. Sarabandi, "Fully Coherent Electromagnetic Scattering Computation for Snowpacks Based on Statistical S-Matrix Approach," in IEEE Transactions on Geoscience and Remote Sensing, doi: 10.1109/TGRS.2020.3026206.

[76] D. M. Pozar, "Microwave Engineering," 6th edition, Hoboken, NJ: J. Wiley, 2005.

[77] W. C. Gibson, "The method of moments in electromagnetics", Taylor & Francis Group LLC, 2010.

[78] M. M. Zaky and K. Sarabandi, " Full-Wave Electromagnetic Scattering Computation for Snow-packs over Rough Surface," in IEEE Transactions on Geoscience and Remote Sensing, under review.

[79] J. R. Kendra, "Microwave Remote Sensing of Snow: An Empirical/Theoretical Scattering Model for Dense Random Media." Ph. D. thesis, University of Michigan, Sept.1995.

[80] H. Marshall, G. Koh, and R. Forster, "CLPX-Ground: Ground-Based Frequency Modulated Continuous Wave (FMCW) Radar, Version 1 [Subset: IOP3 data]", Boulder, Colorado USA, 2004. NASA National Snow and Ice Data Center Distributed Active Archive Center. doi: https://doi.org/10.5067/R3WIYZO7YU82.

[81] C. L. Yeong, and S. Torquato, "Reconstructing random media," Phys. Rev. E, American Physical Society, vol. 57, pp. 495-506, Jan1998.

[82] A. Wiesmann, C. Matzler, and T. Weise "Radiometric and structural measurements of snow samples," Journal of Radio Science, vol.3, no.2, pp. 273 -29, 1998.

[83] C. Mätzler, "Relation between grain-size and correlation length of snow," Journal of Glaciology, vol. 48, no. 162, pp.461-466, 2002.

[84] M. A. Davis, S. D. C. Walsh, and M. O. Saar, "Statistically reconstructing continuous isotropic and anisotropic two-phase media while preserving macroscopic material properties," Phys. Rev. E vol. 83, 2010.

[85] L. M. Pant, S. K. Mitra, and M. Secanell, "Stochastic reconstruction using multiple correlation functions with different-phase-neighbor-based pixel selection," Phys. Rev. E vol. 90, 2014.

[86] H. Malmir, M. Sahimi, and J. Yang, "Higher-order correlation functions in disordered media: Computational algorithms and application to two-phase heterogeneous materials." Physical Review E. 98, 2018. DOI: 10.1103/PhysRevE.98.063317.

[87] Q. Krol, "Upscaling the evolution of snow microstructure: From 4D image analysis to rigorous models." 2017, DOI: 10.5075/epfl-thesis-7996.

[88] C. Coléou, B. Lesaffre, J. Brzoska, W. Ludwig, and E. Boller, "Three-dimensional snow images by X-ray microtomography." Annals of Glaciology, vol. 32, pp. 75-81, 200.

[89] K. Sarabandi, A. Tavakoli, and F.T. Ulaby, "Propagation in a Two-Dimensional Periodic Random Medium with Inhomogeneous Particle Distribution," IEEE Transactions on Antennas and Propagation, vol. 40, no. 10, pp. 1175-1186, October 1992.

[90] J. Vay, I. Haber, and B. B. Godfrey, "A domain decomposition method for pseudo-spectral electromagnetic simulations of plasmas," Journal of Computational Physics, vol. 243, pp. 260-268, ISSN 0021-9991, 2013, https://doi.org/10.1016/j.jcp.2013.03.010.

[91] I. Voznyuk, "Domain decomposition method for electromagnetic modelling and quantitative microwave imaging in large-scale three-dimensional configurations," Electromagnetism. Aix-Marseille Université, 2014.

[92] J. F. Lee, and Z. Peng, "Computational Electromagnetics: Domain Decomposition Methods and Practical Applications," CRC Press, SN. 9781315117379, 2017.

[93] J. R. Mautz, "Mie Series Solution for a Sphere (Computer Program Descriptions)," in IEEE Transactions on Microwave Theory and Techniques, vol. 26, no. 5, pp. 375-375, May 1978, doi: 10.1109/TMTT.1978.1129393.

[94] K. Sarabandi, Y. Oh, and F.T. Ulaby, "A Numerical Simulation of Scattering from One-Dimensional Inhomogeneous Dielectric Random Surfaces," IEEE Transactions on Geoscience and Remote Sensing, vol. 34, no.2, pp. 425-432, March 1996.

[95] F. T. Ulaby, and W. H. Stiles,"Microwave response of snow," Advances in Space Research, Vol. 1, Issue 10, pp. 131-149, 1981.

[96] K. Sarabandi, Y. Oh and F. T. Ulaby, "Measurement and calibration of differential Mueller matrix of distributed targets," in IEEE Transactions on Antennas and Propagation, vol. 40, no. 12, pp. 1524-1532, Dec. 1992, doi: 10.1109/8.204743.

[97] Ioannidis, G.A. and D.E. Hammers, "Optimum antenna polarization for target discrimination in clutter," IEEE Transactions on Antennas and Propagation, vol. 27, no. 5, 1979.

[98] K. Sarabandi, "Derivation of phase statistics from the Mueller matrix," Radio Sci., vol. 27, Sept. 1992.